2007

Satellite Microwave Remote Sensing of Boreal-Arctic Land Surface State and Meteorology from AMSR-E

Lucas Alan Jones
The University of Montana

SATELLITE MICROWAVE REMOTE SENSING OF BOREAL-ARCTIC LAND SURFACE STATE AND METEOROLOGY FROM AMSR-E

By

Lucas Alan Jones
B.S. Resource Conservation (Terrestrial Sciences)
University of Montana, Missoula, MT, 2005

Thesis

presented in partial fulfillment of the requirements for the degree of

Master of Science
Forestry

The University of Montana
Missoula, MT

Autumn 2007

Approved by:

Dr. David A. Strobel (Dean)
Graduate School

Dr. John S. Kimball (Chair)
Division of Biological Sciences
College of Forestry and Conservation

Dr. Steven W. Running (Committee Member)
College of Forestry and Conservation

Dr. Anna E. Klene (Committee Member)
Department of Geography

Jones, Lucas, M.S., December 2007 Forestry

Chairperson: Dr. John S. Kimball

Abstract

High latitude regions are undergoing significant climate-related change and represent an integral component of the Earth's climate system. Near-surface vapor pressure deficit, soil temperature, and soil moisture are essential state variables for monitoring high latitude climate and estimating the response of terrestrial ecosystems to climate change. Methods are developed and evaluated to retrieve surface soil temperature, daily maximum/minimum air temperature, and land surface wetness information from the EOS Advanced Microwave Scanning Radiometer (AMSR-E) on the Aqua satellite for eight Boreal forest and Arctic tundra biophysical monitoring sites across Alaska and northern Canada. Daily vapor pressure deficit is determined by employing AMSR-E daily maximum/minimum air temperature retrievals. The seasonal pattern of microwave emission and relative accuracy of the estimated land surface state are influenced strongly by landscape properties including the presence of open water, vegetation type and seasonal phenology, snow cover and freeze-thaw transitions. Daily maximum/minimum air temperature is retrieved with RMSEs of 2.88 K and 2.31 K, respectively. Soil temperature is retrieved with RMSE of 3.1 K. Vapor pressure deficit (VPD) is retrieved to within 427.9 Pa using thermal information from AMSR-E. AMSR-E thermal information imparted 27% of the overall error in VPD estimation with the remaining error attributable to underlying algorithm assumptions. Land surface wetness information derived from AMSR-E corresponded with soil moisture observations and simple soil moisture models at locations with tundra, grassland, and mixed - forest/cropland *land cover*s (r = 0.49 to r = 0.76). AMSR-E 6.9 GHz land surface wetness showed little correspondence to soil moisture observation or model estimates at locations with > 20% open water and > 5 m^2 m^{-2} Leaf Area Index, despite efforts to remove the impact of open water and vegetation biomass. Additional information on open water fraction and vegetation phenology derived from AMSR-E 6.9 GHz corresponds well with independent satellite observations from MODIS, Sea-Winds, and JERS-1. The techniques and interpretations of high-latitude terrestrial brightness temperature signatures presented in this investigation will likely prove useful for future passive microwave missions and ecosystem modeling.

ACKNOWLEDGMENT

This study was carried out at the University of Montana and at the Jet Propulsion Laboratory, California Institute of Technology, under contract to the National Aeronautics and Space Administration. The author would like to thank Dr. John S. Kimball, Dr. Steven W. Running, and Dr. Anna E. Klene for intellectual guidance. Thanks to the Flathead Lake Biological Station and Numerical Terradynamic Simulation Group labs for administrative support. The work of Faith Ann Heinsch and Maosheng Zhao of the Numerical Terradynamic Simulation Group (NTSG) for obtaining and processing tower station data and MODIS data is appreciated. Erica Podest and Kyle McDonald of the Jet Propulsion Laboratory kindly provided the JERS-1open water product. The author is grateful to the Ameriflux, FLUXNET Canada, and CALM site principal investigators and their teams for the diligent collection of field data and generously allowing us to use it for this study. These investigators include: Walter C. Oechel and the Global Change Research Group of San Diego State University (Barrow, Atqasuk, and Ivotuk); R. F. Paetzold of the National Resource Conservation Service (NRCS), F.E. Nelson of University of Delaware and K. M. Hinkel of University of Cincinnati for Barrow soil moisture data; Larry Hinzman and Doug Kane (University of Alaska Fairbanks) (Happy Valley/Sagwon Hill sites); Allison Dunn and Steven Wofsy of Harvard University (BOREAS NSA Old Black Spruce); T. Andy Black of the University of British Columbia (BOREAS SSA Old Aspen), and Lawrence Flanagan of The University of Lethbridge (Lethbridge). The author thanks his family and friends for patience and support, but most of all inspiration.

Table of Contents

List of Tables:

Table 9
Validation statistics for thawed-season AMSR-E 2004 air temperature (T in **°C**; ~2 m height) retrievals by study location. T_{am} stands for air temperature at time of descending (am) overpass; T_{min} is minimum daily air temperature; T_{max} is maximum daily air temperature. Statistical abbreviations as in Table 7.

Table 10
Validation statistics for thawed-season AMSR-E 2004 Vapor Pressure Deficit (VPD) in pascals (Pa) by algorithm input meteorology and by study site. The VPD algorithm run with T_{min} and T_{max} from AMSR-E is denoted 'VPD AMSRE' and the VPD algorithm run with T_{min} and T_{max} from site observations is denoted 'VPD site met.' Statistical abbreviations as in Table 7.

Table 11
Results for comparison of retrieved AMSR-E 6.9 GHz optical depth to MODIS 8-day LAI by study site. The statistics presented here correspond to regression lines presented in Fig 27.

Table 12a
Pairwise soil moisture validation statistics for the period June 2002- December 2004 for BRW and UPAD sites. The data compared include *in situ* soil moisture (< 8 cm) observations (SM Obs), Antecedent Precipitation Index (API) model, BIOME-BGC soil moisture model, the AMSR-E NASA L3 algorithm soil moisture (L3), and AMSR-E Land Surface Wetness Index (LSW). All data are scaled between 10 % and 95 % and assigned units of % Saturation. Comparisons with corresponding slope statistic significantly ($p < 0.001$) greater than zero are in bold. *Na* indicates that soil moisture observations for the location were not available. Statistical abbreviations as in Table 7.

Table 12b
Same as Table 12a, but for ATQ and IVO sites.

Table 12c
Same as Table 12a, but for HPV and NOBS sites.

Table 12d
Same as Table 12a, but for OAS and LTH sites.

List of Figures:

same in (a) and also in Fig. 10 with the addition of F. Increasing vegetation biomass increases the slope of the line between (e_h^*, e_v^*) and point OW (curved arrow). Broadly dashed lines represent 1:1 in both plots.

Figure 7
Histograms of 6.9 GHz T_{bh} and T_{bv} for June 1-Sept. 31, 2003 across the Northern Hemisphere used for determining the emissivity of open water (OW). Plot represents the distribution of points from Fig. 5 for the T_{bh} - and T_{bv} - axes.

Figure 8
Uncertainty in estimated slope (δa) between land fraction emissivity and open water with increasing open water fraction. Small error in emissivity estimation from errors in land surface temperature estimates (δT), greatly increases uncertainty in land fraction emissivity as open water fraction approaches 1. The effect of 0.5 K radiometer noise is very small and within the thickness of the displayed lines. Mean maximum annual estimated AMSR-E 6.9 GHz for the observation period (June 19, 2002-Dec. 31, 2004) shown as dashed vertical lines.

Figure 9
Percent of MODIS International Geosphere-Biosphere Programme (IGBP) 1-km pixels falling into each land cover class for 60 km x 60 km window extracted over the study sites. Land cover classes are open water, barren areas, crops, grass, open shrubland (Oshrub), mixed forest (MXForest), evergreen needle-leaf forest (ENForest), and other for any IGBP land cover class within the window outside of those listed.

Figure 10
Linear correlation between AMSR-E uncorrected T_{bv} values for various frequencies and *in situ* minimum daily air temperature (T_{min}) and soil temperature (T_{soil}) measurements for selected study sites. Note that the soil and air temperature measurement levels are different for each plot as measurement depth differed between each site.

Figure 11
Linear correlation of AMSR-E multi-frequency T_{bv} to *in situ* air temperature (~2 m) plotted by study site corresponding to the time of the descending (am) satellite overpass.

Figure 12
AMSR-E 6.9 GHz V and H polarized brightness temperatures over selected study sites from 2002 to 2004.

Figure 13
Linear correlation coefficient (r) between AMSR-E 6.9 GHz T_{bh} and site observed soil moisture (< 8 cm) and AMSR-E 6.9 GHz T_{bh} and MODIS 8-day LAI plotted against maximum annual MODIS LAI and percent open water derived from MODIS IGBP land cover 60 km x 60 km window extractions. Closed symbols indicate that correlation is significant ($p < 0.05$) of expected sign (see Table 6).

Figure 14
Scatter plot of 2004 thawed-season retrievals for the regression and process-based AMSR-E T_s methods and associated statistics.

Figure 15
Both methods of AMSR-E T_s retrievals ($^{\circ}$C) plotted against $T_{soil,}$ $T_{min,}$ and MODIS LST at the study sites for 2004. MODIS LST error bars represent the standard deviation of the 1 km x 1 km resolution based MODIS LST results within a 60 km x 60 km window centered at each site.

Figure 16
MODIS 8-day LAI (m^2/m^2) time series and AMSR-E g (kg/m^2) vegetation/roughness parameter plotted results for 2003. The points represent daily values of g, while the solid black lines represent an 8-day running average (g_{sm8}).

Figure 17
Snow depth plotted time series at BRW and OAS (dashed gray lines) and AMSR-E W_s (cm)**.** The points represent daily values of W, while the solid black lines represent an 8-day running average.

Figure 18
Root mean square error (RMSE) in Kelvin (K) for all AMSR-E temperature algorithms considered in this investigation. Values are tabulated in Table 7 and Table 9.

Figure 19
Mean residual (MR) in Kelvin (K) for all AMSR-E temperature algorithms considered in this investigation. Values are tabulated in Table 7 and Table 9.

Figure 20
Error introduced in VPD estimate from error in air temperature estimates. a) Error introduced in saturation water vapor pressure for given levels of error in air temperature. b) Error introduced in VPD estimates from independent errors (δT) in T_{min} and T_{max} inputs for fixed levels of T_{min}. c) Relative error (%; $\delta VPD / VPD * 100$) introduced in VPD estimates from independent errors (δT) in T_{min} and T_{max} inputs for fixed levels of T_{min}.

Figure 21
Overall results from validation of AMSR-E T_{max} and T_{min} plotted against site observations and associated statistics (upper plots). Overall results from prediction of VPD from the VPD algorithm run on site observed meteorology and from prediction of VPD using AMSR-E T_{max} and T_{min} vs. site observations of VPD and associated statistics (lower plots). Dashed line represents 1:1.

Figure 22
Root mean square error (RMSE) in pascals (Pa) for the VPD algorithm run on site meteorology and the VPD algorithm with AMSR-E meteorology. Values are tabulated in Table 10.

Figure 23
Mean residual (MR) in pascals (Pa) for the VPD algorithm run on site meteorology and the VPD algorithm with AMSR-E meteorology. Values are tabulated in Table 10.

Figure 24
Relative amount of error introduced by employing the AMSR-E meteorology in the VPD algorithm plotted as a percentage of overall AMSR-E VPD retrieval RMSE.

Figure 25
Maximum annual open water fraction estimated from AMSR-E 6.9 GHz (2002-2004) compared to JERS-1 EASE-grid open water map and MODIS land cover with relevant statistics. Symbol shapes same as fig. 13, except that closed symbols stand for JERS-1 and open symbols stand for MODIS. JERS-1 data were only available for Alaska North Slope locations.

Figure 26
Time series of thawed season open water fraction by study location derived from AMSR-E 6.9 GHz observations. Gaps in the AMSR-E lines represent missing daily values.

Figure 27
Relation between AMSR-E 6.9 GHz canopy optical depth (τ_c) and MODIS 8-day Leaf Area Index (LAI) means derived from 60 km x 60 km windows. The lines represent linear-least squares fits for each location. Statistics for the lines are in Table 11.

Figure 28
Time series of thawed season AMSR-E 6.9 GHz canopy optical depth (τ_c) and MODIS 8-day LAI by study location. Error bars represent one standard deviation from the mean 8-day LAI within 60 km x 60 km windows. Gaps in the AMSR-E lines represent missing daily values.

Figure 29
Time series of thawed season NASA L3 soil moisture algorithm $\overline{w}$ parameter by study location. The $\overline{w}$ parameter contains information on both vegetation biomass and open water fraction combined.

Figure 30
Scatterplots of model (API, BGC) and AMSR-E soil moisture algorithm (L3, LSW) results vs. site observed soil moisture and API (all in % saturation) by study location. Composites of 8-day means are displayed to improve visualization. The associated statistics for the daily values are shown in Tables 12a-d. Dashed lines represent 1:1 for each panel.

Figure 31
Time series of thawed season model (API, BGC), AMSR-E soil moisture algorithm (L3, LSW) results, and site observed soil moisture by location and year for the observation period (June 19, 2002 to Dec. 31, 2004). Plots depict growing season differences and time series correspondence between locations down each column and across time within a site across each row.

Figure 32
Histograms of soil moisture across locations where the AMSR-E algorithms showed correspondence to both site observed soil moisture (< 8 cm) and API (LTH, OAS, and HPV).

I. Introduction

High latitude regions are undergoing significant climate-related change and represent an integral component of the Earth's climate system. Observational evidence indicates that mean annual air temperatures (~ 2 m height) in Arctic and Boreal regions have warmed 2-4 ˚C in the last several decades (Oechel 1993; Serreze 2000; Hinzman 2004). Global model projections indicate that warming under future climate change will be most pronounced in high latitude regions (Gates 1992; IPCC 2001). Warming is expected to alter the terrestrial carbon cycle (Oechel 1993; Oechel 1995; Euskirchen 2006), surface energy balance (Eugster 2000), and hydrologic systems with resulting feedbacks to climate (Hinzman & Kane 1992).

Ecosystem responses to warming include advances in growing season timing and duration, increases in vegetation growth and extent of woody shrubs (Sturm 2001), increases in the depth of annual soil thaw, and decreasing permafrost extent (Osterkamp & Romanovsky 1999). Increasing soil thaw depths and thawing permafrost coupled with low annual precipitation characteristic of Arctic regions will potentially cause deepening of local water tables (Hinzman 2004). Drying of surface soil layers coupled with warming may potentially cause increases in efflux of CO_2 from soil organic matter decomposition and acceleration of soil nutrient cycles (Oechel 1998). Drying may change the partitioning of latent and sensible heat energy, further increasing surface temperature and terrestrial ecosystem stress. Recent satellite evidence corroborated with field data suggests that widespread drought has caused marked decreases the net-primary productivity of North American Boreal regions (Bunn 2007). Near-surface vapor pressure deficit, soil temperature, and soil moisture therefore are essential state variables

for monitoring high latitude climate and estimating the response of terrestrial ecosystems to climate change.

High-latitude regions have a sparse network of meteorological stations which strongly limit regional climate monitoring. Additionally these stations usually provide air temperature, relative humidity and precipitation information; soil moisture and soil temperatures are seldom directly measured at standard meteorological stations. Accurate surface meteorological information is needed to provide critical inputs for regional scale biophysical and hydrological models (Crow & Wood 2002; Zhang 2007). The largest error in the MODIS MOD17 terrestrial productivity products was introduced by uncertainties in daily surface meteorology inputs (Hiensch 2006). Uncertainties in the surface energy and water budgets of global re-analysis models are also contingent upon land surface parameterization and high latitude feedbacks (Stieglitz 1999).

The latest generation of NASA's Earth Observing System (EOS) satellite-remote-sensing-based observations provides an unprecedented array of global daily monitoring capabilities at moderate spatial resolution, including multi-band optical-infrared and passive-microwave-based measurements from MODIS and AMSR-E, respectively. These measurements are sensitive to thermal and moisture characteristics of the land surface and provide a potential alternative to spatially gridded meteorological data from sparse surface station networks and model re-analyses for driving terrestrial ecosystem models.

Land surface temperature information has commonly been obtained from satellite infrared remote sensing observations from the NOAA Advanced Very High Resolution Radiometer (AVHRR), Advanced Space-borne Thermal Emission and Reflection Radiometer (ASTER), METEOSAT, and NASA's Moderate Resolution Imaging

Spectroradiometer (MODIS; Goita 1997; Gillespie 1998; Verstraeten 2006; Wan 2002; Comiso 2002). Thermal infrared land surface temperature algorithms are distinguished by methods of atmospheric aerosol and cloud-cover screening, and estimation of the surface emissivity (Gillespie 1998). Infrared land surface temperatures have also been used to derive soil wetness information using thermal inertia approaches (Verstraeten 2006; Anderson 2007). Soil wetness information has also been derived from optical data by analyzing the slope of the relationship between land surface temperatures and the Normalized Difference Vegetation Index (NDVI; Nemani 1993; Gillies 1997; Sandholt 2002).

Satellite passive microwave sensors afford advantages over optical-infrared sensors. Despite having a relatively coarse spatial resolution (>5 km), microwave sensors are less impacted by cloud cover, smoke, and atmospheric aerosol effects, and can retrieve surface information day or night, regardless of solar illumination conditions. This represents a significant advantage for regional monitoring at high latitudes. Past and current passive microwave satellite missions include the Special Sensor Microwave/Imager (SSM/I), Scanning Multi-channel Microwave Radiometer (SMMR), and Advanced Scanning Microwave Radiometer flying on the NASA EOS Aqua satellite (AMSR-E).

Microwave emission at low frequencies, e.g. C-band (~6.9 GHz) and L-band (~1.4 GHz), responds to temperature and moisture conditions under vegetation and below the soil surface, though direct sensitivity to these deeper microwave-emitting layers decreases under increasing vegetation water content (Ulaby 1989). The emitting soil layer is shallower and the vegetation opacity is greater for high frequency microwave

observations. The emitting depth is typically between 0.5 and 2.8 cm at C band for soil volumetric moisture contents of 10 and 50% respectively, assuming a soil bulk density of 1.50 g cm^{-3} typical of tundra soils (Ulaby 1989). Frequencies of 10.7 GHz and lower may be susceptible to radio frequency interference (RFI) near densely populated areas depending upon the bandwidth, center frequency, and polarization of the anthropogenic radiation and characteristics of the observing sensor (Njoku 2005; Ellingson & Johnson 2006); however, this may not be a significant problem in sparsely populated high-latitude regions. Low frequency passive microwave observations (<18 GHz) are also sensitive to open surface waters (Fily 2003), vegetation biomass (Paloscia & Pampaloni 1988; Jackson & Schmugge 1991; Njoku & Chan 2006), freeze-thaw state (McDonald 2004; McDonald & Kimball 2005), sea ice (Comiso 2003), and snow cover (Kelly 2003).

Few studies have considered the retrieval of surface temperatures from passive microwave observations, although surface temperature is a vital state variable and an important ancillary parameter in soil moisture retrieval algorithms. McFarland (1990) applied a multiple regression of several frequencies from the SSM/I to derive soil temperature in the central plains of the United States and reported difficulty in retrieving soil temperature under wet and snow-covered conditions. Basist (1998) used a spectral difference method to correct for surface water and snow cover to retrieve screen-height (2 m) air temperatures from the SSM/I. A polarization ratio method was applied to retrieve soil temperatures from a tower-based radiometer over a variety of land cover conditions in Switzerland (Matzler 1994) and from SSM/I 19 GHz brightness temperatures under both frozen and snow-covered winter surfaces (Hiltbrunner 1994). This method was also employed for surface temperature retrieval in the Boreal forest of Finland and was

reported to have larger error over dense vegetation than an empirical multiple-regression method (Pulliainen 1997). A similar polarization ratio method was applied to retrieve surface temperature and surface water fraction over wet Arctic and Boreal regions of northern Canada under snow-free conditions (Fily 2003). Iterative inversion of radiative transfer equations has also been explored (Njoku & Li 1999), as well as learning algorithms such as neural networks, which have been explored for dealing with surface heterogeneity (Aires 2001); both methods require either a great deal of accurate *a priori* information on land cover parameters or large training data sets.

Past studies of land surface microwave emission have gone through great lengths to correct passive microwave brightness temperatures (T_b) for atmospheric influences using re-analysis data (Prigent 1997). We prefer to avoid this approach because re-analysis data can have large biases, especially at high latitudes (Zhang 2007), and systematically building such biases into the microwave algorithms in this study, at least in the absence of a data assimilation framework, would potentially obscure information contained in the microwave observations. The retrieval of atmospheric water vapor estimates from AMSR-E channels is currently limited to ocean regions due to the strong relative influence of land surface emissivities on T_b. This underscores the need to first describe land surface emissivity before considering atmospheric influences in land surface temperature algorithms, although proper consideration of atmospheric influences will surely improve future algorithms.

Low frequency (≤10.7 GHz) passive microwave T_b observations can be highly sensitive to soil moisture content. Theoretical sensitivities show up to a 95 K decrease in C-band (6.6 GHz) H-polarization T_b over bare, smooth loam soil and a homogenous field

of view (Njoku 1999). Under most circumstances for natural surfaces, however, the soil moisture T_b response is intertwined with several other factors. Over most natural surfaces T_b is influenced strongly by surface kinetic physical temperature, which shows large daily to seasonal fluctuations; open water, such as rivers, lakes, and oceans along coasts, which are especially prevalent in high latitude regions; and vegetation canopies, surface litter, and terrain roughness. Surface physical temperature is inversely proportional to daily soil moisture variations through the partitioning of solar energy into latent and sensible heat, although surface temperature trends may mask changes in T_b due to higher soil moisture contents. Open water causes a reduction in T_b similar to soil moisture but usually much more strongly. The open water fraction of the sensor field-of-view dominates the T_b signal, reducing the bulk T_b signal of the footprint.

Vegetation canopies and roughness have similar effects, both increasing T_b in the H-polarization and quickly reducing the sensitivity of H-polarization T_b to soil moisture. Recent investigations have shown that wet vegetation litter, dew, and canopy rain interception, which tend to correspond with soil moisture, can make such effects more severe (Shi 2002). The response of T_b at V-polarization to these factors can be an increase or decrease depending on the amount of radiation absorbed relative to the amount scattered (Prigent 2005). The spatial resolution of low frequency AMSR-E microwave observations is relatively coarse (~60 km x 60 km at C-band), so scenes contain mixtures of vegetation, open water, and soil that determine the bulk T_b of the scene.

The relative accuracy of microwave soil moisture algorithms depends on how well the competing factors on T_b are reduced or eliminated. Methods usually take a mixture of four approaches to accomplish this including: *i*) polarization or spectral

indices to reduce the dependence on any particular factor, such as using a polarization ratio to reduce surface temperature dependence; *ii*) using ancillary variables, including NDVI from optical observations to correct for vegetation biomass (Jackson 1999); *iii*) time series techniques such as smoothers and filters (Wagner 1999a; De Ridder 2003); *iv*) iterative methods that simultaneously solve for soil moisture and other variables using multiple channels (Njoku 1999; Njoku 2003; Owe 2001).

Tradeoffs exist among the various methods of correcting for confounding effects on T_b. Indices, such as polarization and spectral ratios, provide reduced dependence on one factor, but they sometimes may magnify the influence of other factors. In the case of the polarization ratio, the surface temperature dependence is greatly reduced, but where T_{bv} and T_{bh} (T_b at V- and H-polarization, respectively) move in opposing directions, such as respectively decreasing and increasing as a result of scattering, the polarization ratio shows enhanced response to vegetation or roughness relative to T_{bh} alone (Shi 2006). Ancillary variables introduce bias and uncertainty characteristic of their sources, for example, NDVI as seen by an optical instrument might not correspond to the same vegetation characteristics to which microwaves respond. Time series techniques run the risk of eliminating time trends that occur within similar time-scales as the variable of interest. Iterative methods are attractive alternatives because they can provide information on several variables at once independent of ancillary information. Iterative methods have been used successfully in microwave remote sensing of the ocean, atmosphere, and soil moisture in field-scale experiments; however, current lack of knowledge of land surface emission processes at coarse spatial scales have limited the accuracy of iterative methods for application to regional to global soil moisture retrieval.

Soil moisture validation for satellite scales has been historically hampered by the limited availability of *in situ* observations, lack of correspondence of the depth of those observations to actual satellite sensing depth, and low spatial correspondence between point observations and satellite retrievals integrated over relatively coarse spatial scales (~60 km x 60 km; Crow 2007). These factors are also present for surface temperature and vapor pressure deficit (VPD) validation comparisons; however, the spatial variability of soil moisture is usually much greater than for these typically smoothly distributed parameters as soil moisture is impacted by micro-topography, soil properties, vegetation, and precipitation patterns, which introduce spatial heterogeneity (Western & Bloschl 1999).

Soil moisture estimation from airborne and satellite microwave remote sensing over agricultural landscapes has been extensively investigated; however, much less attention has focused on regional soil moisture estimation over heterogeneous natural land surfaces. Microwave algorithms for soil moisture estimation differ primarily in how satellite observations are corrected for the impacts of surface physical temperature, vegetation biomass, surface roughness, and open water fraction. Jackson (1999) developed an algorithm that uses NDVI and infrared surface temperatures to sequentially correct the brightness temperature at a single frequency and polarization to estimate soil moisture. Njoku (2003) used a multi-frequency dual-polarization approach to simultaneously estimate vegetation biomass and soil moisture. Owe (2003) employed a single-frequency approach that simultaneously retrieves both vegetation biomass and soil moisture and accounts for vegetation biomass using the ratio of two polarizations. Wagner (1999a; 1999b) used scaled radar backscatter observations from the European

Remote Sensing System (ERS)-1 scatterometer for global soil moisture retrieval. Bassist (2001) employed an approach over the continental United States that considers the combined influence of soil moisture and open water as a "wetness index" described by the spectral difference of several frequencies.

Current approaches are limited by the accuracy and availability of ancillary information, by limited knowledge of the frequency and polarization dependence of the microwave emission models, and lack of knowledge of how emission model parameters vary over natural landscapes. An advantage of process-based methods is that they incorporate information on physical processes and mechanisms they can give insight into radiative transfer processes; they can also be refined for different land cover types, transferred between sensors, and refined as more information is obtained. Drawbacks of process-based approaches are that their solutions can be unstable or indeterminate if the model parameters are inaccurately specified or if the model itself does not capture the dominant components of the radiative transfer process; they also often require much ancillary information or detailed knowledge of multi-frequency and polarimetric responses to emission processes.

II. Objectives and Hypotheses

The objectives of this investigation are to *i*) evaluate the spatial and seasonal dynamics of multi-frequency, dual-polarized AMSR-E brightness temperature data relative to surface biophysical station observations of daily soil, land surface, and meteorological observations, *ii*) develop approaches to retrieve soil and air temperatures,

land fraction soil surface wetness, and daily average VPD information from AMSR-E under temporally dynamic surface physical conditions, and *iii*) determine the information content and accuracy of the algorithms relative to point observations, simple model simulations, and observations from other satellite products including AMSR-E operational Level 3 products, MODIS products, and JERS-1 products in Arctic and Boreal biomes.

We develop and apply algorithms to retrieve surface (<5 cm depth) soil temperature, and daily air temperatures (~2 m height) for future use in biophysical modeling at high-latitudes. A simple approach to derive near-surface daily VPD from daily am-pm overpass AMSR-E observations is also developed. We additionally develop a method to derive soil wetness by correcting for vegetation biomass and open water fraction effects, and compare this method with the NASA operational Level 3 soil moisture product (Njoku 2004) relative to process-model simulations of soil water status and site observations of soil moisture.

We employ satellite observations from MODIS and *in situ* observations for fitting parameters, driving simple soil moisture models, and assessing satellite algorithm performance; these data were collected at three Ameriflux (Oechel 2000), three FLUXNET Canada eddy-covariance flux towers (Flanagan and Johnson 2005; Griffis 2004; Dun and Wofsy 2006), two Kuparuk river basin sites administered by the University of Alaska Fairbanks Water and Environmental Research Center (Kane and Hinzman 2006), and two sites administered by the Natural Resources Conservation Service (NRCS) located in five distinct vegetation and land cover regimes representing major Boreal forest and Arctic tundra biomes (Paetzold 2006). The satellite data are

from footprint extractions of spatially re-sampled AMSR-E L2A orbital-swath data and windows of MODIS optical data centered at each tower location. Additionally AMSR-E L2A Northern Hemisphere EASE grid data for 2003 is employed for gaining an understanding of broad-scale emission patterns.

III. Methods

1. Study Sites

The eight study sites are representative of five distinct vegetation types (Table 1; Fig. 1). The vegetation types are coastal lowland wet-sedge tundra, upland tussock tundra, Boreal evergreen forest, Boreal deciduous forest, and Boreal grassland. Tundra landscapes are generally a mosaic of tussock and sedge tundra vegetation types; however, for convenience the tundra sites were grouped according to the dominant vegetation type. Wet sedge tundra dominates in moist poorly drained lowland and coastal areas, whereas tussock tundra dominates the drier upland/foothill sites. Coastal wet-sedge tundra is represented by the BRW, UPAD, and ATQ sites and is characterized by low topography and a shallow water table with numerous thaw lakes. The vegetation is predominantly composed of low-growing sedges and mosses, interspersed with areas of shallow standing water. Soils are highly organic and consist of a shallow active layer that thaws each growing season and is underlain by continuous permafrost (Oechel 1995; Kwon 2006). Wet sedge tundra lacks the hummocky micro-topography of tussock tundra, but may contain polygonal features formed by frost-wedge action, which consist of raised

surfaces surrounded by shallow troughs (high center polygons), or low centers surrounded by a raised rim (low-center polygons). Tussock tundra at IVO and HPV is characterized by *Eriophorum vaginatum*, also known as 'cotton grass,' and low shrubs (Epstein 2004). These two sites are located within ~40 km of the Brooks Range and the active layer tends to be thicker than that of coastal sites (Hinkel & Nelson 2003).

The Boreal sites are located in central Canada. Boreal evergreen coniferous forest is represented by the Northern Old Black Spruce (NOBS) site and is dominated by mature black spruce (*Picea marianna*) forest with a canopy height of 10-13 m and low topographic relief (Dunn & Wofsy 2006; Dunn 2006). The Old Aspen (OAS) site is composed of deciduous broad-leaf Boreal forest dominated by aspen (*Populus tremuloides*) with a mean canopy height of 21 m and low topographic relief (Griffis 2004). The Lethbridge (LTH) Boreal grassland site is the southern-most study site and is composed of semi-arid short-grass prairie on relatively flat terrain (Flanagan & Johnson 2005).

2. *In Situ* Observations

Soil temperatures were obtained from tower and hydrologic monitoring site investigators. Soil temperature data were recorded at a variety of measurement depths at each location. The 0-5 cm depth was selected as the primary focus of this investigation because it was readily available across all study sites. Although lower range of this depth is greater than the expected microwave emitting depth of 2.5 cm at C-band or less for higher frequencies and greater soil moisture levels (Njoku 1995), we observed that daily

temperature differences between near surface soil depths and daily minimum air temperatures (above and below canopy for forested sites) are highly correlated with brightness temperatures under all conditions (r >0.70; p<0.001). For simplicity we assumed that the near surface soil profile (e.g. <5 cm) is generally isothermal. Vertical and horizontal heterogeneity in soil temperature within and across the field-of-view also potentially adds variability to the brightness temperature observations. For this reason we compare the surface temperature retrievals to three independent measures of surface temperature. Observations of T_{soil} and T_{min} bracket the upper and lower bounds of the emitting-layer, while MODIS Land Surface Skin Temperature (LST) observations are used to assess sub-grid scale spatial heterogeneity in surface temperature conditions within the AMSR-E footprint. Soil and air temperature measurements from the study sites were reported at either 30-minute or 1-hour intervals and aggregated to daily minimums for comparison with daily satellite morning (AM) overpass observations. Daily minimums of soil temperature (5 cm) were not significantly different (p>0.05) from the temperature at overpass time and the temperature at time of the minimum temperature gradient between the 2 and 5 cm depths at all sites. This assumption holds well for Arctic and Boreal soils which have a large amount of thermal inertia relative to drier mid-latitude soils with more intense diurnal heating.

Soil moisture, air temperatures, and VPD (or other relative humidity information) time series were obtained for the sites or nearby locations (within 25 km) within the AMSR-E footprint where data was available. Soil moisture observations ranged from 2-10 cm depths between sites and were reported as daily or sub-daily values. Soil moisture data was required to show time series variability during the thawed season to be included

in the analysis. Data from sites that remained saturated throughout the summer were omitted. Soil moisture data were inspected for anomalous offsets between observational periods. These types of offsets were likely due to changes in sensor calibration or loss of soil contact. If an offset was detected, the longest period on either side of the offset was included in the analysis and the remaining data were discarded. Soil moisture observations also represented a wide range of soil characteristics between site locations and soil characteristics for each sensor location were not necessarily reported. Soil moisture values were therefore scaled between local maximum and minimum values to represent a relative (% saturation) index of surface wetness for the study period (June 2002 to December 2004) within each location. All air temperature and VPD information was reported at either 30- or 60-minute intervals. This allowed for determining air temperature close to the time of satellite overpass, in addition to minimum and maximum daily values. All *in situ* data were obtained from June 2002 to December 2004 to coincide with AMSR-E observations, which began with the launch of the Aqua satellite in May of 2002.

3. AMSR-E Satellite Data

The Advanced Microwave Scanning Radiometer on EOS (AMSR-E) flies on the Aqua satellite platform and measures brightness temperatures at frequencies of 6.9, 10.7, 18.7, 23.8, 36.5, and 89 GHz, for vertical and horizontal polarizations (Table 2). Aqua is polar-orbiting with 1 AM and 1 PM equatorial crossing times, providing multiple daily acquisitions in Polar Regions (Njoku 1999). For high-latitude regions, the overlapping

orbital swaths allow 2 to 4 T_b observations per footprint overpass with a typical standard deviation of ~1 K (max = 5 K) at 6.9 GHz and <1 K (max =3.5 K) at 89 GHz. T_b measurements were extracted at each test site from the AMSR-E level 2A orbital swath data spatially re-sampled to the ~60 km x 60 km 6.9 GHz resolution (Ashcroft and Wentz 1999).

The T_b observations were only extracted from sensor footprints whose centroid falls within 5 km of each tower location. Therefore the observations can be considered to be representative of a ~60 km x 60 km pixel centered at the tower location. The minimum T_b of the descending (AM) overpass was selected on a daily basis for each site location under the assumption that the diurnal temperature minimum is more representative of surface soil layer temperatures. The descending overpass occurs from 3-6 AM local time in the study region and was chosen because the near surface soil and air temperatures were expected to be closer to thermal equilibrium.

The brightness temperatures were inspected for radio frequency interference (RFI) using the difference between the 6.9 and 10.7 GHz channels and the difference between the 10.7 and 18.7 GHz developed by (Njoku 2005). For LTH, where RFI was expected to be most severe, a mean thawed condition RFI index for the 6.9 GHz (10.7 GHz) band V-polarization of 0.51 K (-0.25 K) and a standard deviation of 0.99 K (1.11 K) were calculated. These values are well below the 3 K 6.9 GHz and -0.25 K 10.7 GHz index thresholds suggested for identifying moderate to strong RFI (Njoku 2005). The H-polarization mean 6.9 GHz and 10.7 GHz RFI indices were similarly small (0.14 K for 6.9 GHz and 0.14 K at 10.7 GHz) at LTH. The RFI index for the 6.9 GHz band did range as high as 9.0 K for frozen conditions, but was assumed to be from the effects of snow

cover and not RFI. These results indicate that moderate RFI was not detected in either the 6.9 GHz or the 10.7 GHz channel at H- or V-polarization at the study sites, and filtering of the brightness temperatures for RFI was not necessary.

In addition to the site extractions of AMSR-E L2A data, Northern Hemisphere 25-km Equal Area Scalable Earth (EASE) grids were also obtained for Jan. 1 to Dec. 31, 2003. The EASE grid data were employed to gain an understanding of the overall response of AMSR-E T_b to land, ocean, and atmospheric factors, and to empirically fit algorithm parameters over specific land cover types, but were not otherwise employed in the analysis.

4. MODIS Satellite Data and Correlation Analysis

Land cover heterogeneity within each AMSR-E tower footprint was assessed by extracting 60 km x 60 km windows centered over each tower site from the MODIS 1 km x 1 km resolution global land cover classification (Friedl 2002). The MODIS land cover extraction subsets were obtained from Maosheng Zhao. Relative proportions of the International Geosphere-Biosphere Program (IGBP) based land cover classes were calculated from the MODIS land cover classification results within each window. MODIS Leaf Area Index (LAI) estimates were also obtained.

Simple linear correlation coefficients were computed between daily time-series AMSR-E V-polarized T_b and available *in situ* soil and near-surface air temperature measurements under thawed conditions to gain an understanding of the relation between sensor T_b from individual bands and the surface temperature profile for each study site.

Previous studies have shown that V-polarized T_b is generally more sensitive to surface temperature than H-polarized T_b (McFarland 1990; Njoku 1995) because V-polarization observations are less sensitive to soil moisture and open water.

Five indices were compared to site observations of soil moisture (< 10 cm) and MODIS Leaf Area Index (LAI). The indices included 6.9 GHz H-polarization brightness temperatures (T_{bh}), 6.9 GHz H-polarization effective emissivities (e_h) calculated using the observed site air temperatures at the time of the descending overpass, simple polarization ratio (T_{bv}/T_{bh}), a spectral ratio (36.5 GHz T_{bh}/6.9 GHz T_{bh}), and a spectral cross-polarization ratio (36.5 GHz T_{bv} / 6.9 GHz T_{bh}).

5. Basic Principles of Passive Microwave Land Surface Remote Sensing

Passive microwave observations of the Earth's surface are influenced by the physical temperature, dielectric properties, and physical structure of the terrain. Radiometers are passive sensors that observe a target's natural thermal emission. Thermal radiance is generally expressed as a brightness temperature (T_b) in Kelvin relative to a perfect blackbody emitter and is specified by frequency and polarization. The brightness temperature at polarization p (e.g. T_{bp}) of the Earth's surface at atmospheric window channels can be approximated as the product of the object's physical temperature (T_s) and its apparent emissivity (e_p):

$$T_{bp} = e_p T_s \tag{1}$$

In (1) the physical temperature is integrated over the contributing depth and emissivity as a unitless scalar that can range from 0 to unity, with unity representing a perfect blackbody emitter. Emissivity is related to the reflectivity (r_p) of a surface by Kirchoff's Law (e.g. $e_p = 1 - r_p$) based on the assumption that nonscattered energy emitted from the soil surface must equal the down welling radiation absorbed by the soil if the soil is in thermal equilibrium with its surroundings (Shi 2002). The quantity r_p provides a conceptual link between passive and active (radar) microwave remote sensing. The apparent emissivity is determined by the dielectric and scattering properties of observed materials.

The dielectric constant describes how a material's molecules respond to an applied electromagnetic field by a complex number (ε_r):

$$\varepsilon_r = \varepsilon_r' - j\varepsilon_r'' \tag{2}$$

The real part (ε_r') of (2) represents the permittivity of the material relative to that of a vacuum and is related to the material's ability to store an electric field. The imaginary component (ε_r'') of the dielectric constant is related to the energy loss of an electromagnetic wave propagating through the medium. Liquid water has a high ε_r at microwave frequencies relative to other common earth-surface materials. The locking of molecules into a crystal lattice as freezing occurs reduces water's ε_r and produces marked changes in satellite observations of wet landscapes during the freezing or thawing processes (McDonald 2005). The ε_r of liquid water increases with frequency from 3 at

100 GHz to 85 at 1.4 GHz (L-band). The Fresnel coefficients relate the reflectivity of a smooth surface at given incidence angle to the material's ε_r (Ulaby 1987). The difference between reflectivities at vertical (*v*) and horizontal (*h*) polarizations is greatest at a critical angle, the Brewster angle, where all the energy at vertical polarization is transmitted into the material. Microwave instruments are designed to take advantage of land surface information contained in the polarization difference by viewing the Earth from near the Brewster angle.

Scattering typically increases with frequency in the microwave spectral region. Rough surfaces including complex topography and agricultural windrows, and porous media, such as snow or vegetation canopies, scatter microwave radiation, mixing polarizations and mixing the directions of wave propagation. Physical models of land surface scattering are typically too complex for application to satellite remote sensing observations, so several simple parameterizations have been suggested (Shi 2006; Matzler 2006; Escorihuela 2007) most based on the *Q*-*h* model of Wang and Choudhury (1995) relating rough surface reflectivity at polarization *p* (r_{sp}) to smooth surface reflectivity at polarization *p* (r_{op}) and orthogonal polarization *q* (r_{oq}):

$$r_{sp} = [(1-Q)r_{op} + Qr_{oq}]\exp(-h) \tag{3}$$

The empirical factors *Q* and *h* depend on the root mean square (RMS) height and horizontal correlation length. Several parameterizations based on (3) have been applied. Discrepancies of the *Q*-*h* model with detailed field radiometric observations over bare soil and detailed physical scattering models have been noted (Li 2000). Recent

investigations have shown that the *Q*-*h* model implies a dependence of the roughness parameters *Q* and *h* on soil moisture, which does not follow current physical knowledge that scattering of rough surfaces is independent of soil moisture content (Shi 2006; Matzler 2007). Nevertheless, the *Q*-*h* model has been widely applied as a useful semi-empirical model with the *Q* and *h* parameters empirically fit to observations.

Simple radiative transfer models incorporating first-order effects are applied to describe vegetation and other land cover effects. A scene containing vegetation-covered soil can be described as (Njoku & Chan 2006):

$$T_{bp} = T_s\{e_{sp}\exp(-\tau_c) + (1-\omega_p)[1-\exp(-\tau_c)][1+r_{sp}\exp(-\tau_c)]\} \quad (4)$$

where the soil skin temperature is assumed equal to the temperature of the vegetation and that multiple scattering effects and scattering at soil-atmosphere and vegetation-atmosphere interfaces are negligible. These assumptions are considered valid for lower frequency observations (≤ 18.7 GHz) where scattering is expected to be less significant. Soil with emissivity (e_{sp}) is covered by a continuous layer of vegetation with single scattering albedo (ω_p) and opacity (τ_c). The effective emissivity of a scene is made up of three components, including: soil emission attenuated by the canopy; radiation emitted upwards by the canopy itself, and radiation emitted downwards by the vegetation and reflected by the soil back through the canopy.

The canopy absorption of upwelling radiation is controlled by τ_c:

$$\tau_c = b_c W_c / \cos(\theta) \quad (5)$$

Here b_c is the canopy absorption loss factor dependent on canopy type and frequency (Jackson & Schmugge 1991; Van de Griend & Wigneron 2004). W_c is the vegetation water content usually expressed in kg m^{-2}. The denominator accounts for a longer path length though the canopy from a view of angle θ from nadir. If the canopy is sufficiently opaque that the signal is dominated by canopy emission, (4) is dominated by radiation scattered upward from the canopy and becomes $T_{bp} = T_s(1-\omega_p)$ (Ulaby 1987).

The case of snow cover is analogous to that of vegetation, by considering the snow pack as a single-scattering absorbing and emitting layer (Grody & Bassist 1997):

$$T_{bp} = T_s[(1-\omega_{sn})(1-\exp(-\tau_{sn})) + e_{sp}\exp(-\tau_{sn})] \quad (6)$$

In contrast to the vegetation situation, this case only considers the emission of the snow and the emission of the underlying soil attenuated by the snow, neglecting reflected down welling radiation. The underlying soil is usually considered frozen with emissivity e_{sp}, the pack opacity is τ_{sn}, and the upward scattering of the pack is described by ω_{sn}. The opacity of the pack is determined by:

$$\tau_{sn} = \exp(-b_{sn}W_s \sec(\theta)/\lambda) \quad (7)$$

Where the snow loss factor (b_{sn}) describes how rapidly the water content of the snow, W_s usually in equivalent water depth, masks the snow signal, which depends on the view angle, θ, and the free-space wavelength λ (Grody & Bassist 1997).

The atmosphere influences T_{bp} in (1) by absorbing surface emission ($T_{bp,surf}$) or scattering the emitted radiation and contributing additional thermal emission in upward (T_u) and downward directions (T_d):

$$T_{bp} = T_u + \exp(-\tau_a)[T_d r_{sp} \exp(-\tau_c) + T_{bp,surf}] \quad (8)$$

The atmospheric opacity (τ_a) is determined by absorption from oxygen and columnar water, including water vapor and clouds. An increasing atmospheric opacity generally leads to an increase in the observed satellite brightness temperatures and associated increases in atmospheric thermal emission. Below about 18.7 GHz the transmissivity of the atmosphere ($\exp(-\tau_a)$; ranging from opaque at 0 to transparent at unity) is generally >0.9, although absorption by active rainfall can effect all frequencies. Aside from a water vapor absorption band at about 22.3 GHz, the influence of atmospheric absorption increases with frequency above 18.7 GHz due to an increasing sensitivity to water vapor. In the higher frequencies atmospheric effects can also drastically reduce brightness temperatures as in the case of scattering from rain and ice particles.

Microwave observations are influenced by several land surface and atmospheric factors and deriving information on any single signal requires techniques that reduce or eliminate signal dependence on these additional effects. Often observations and models developed for field-scale applications do not hold true for coarser-scale satellite observations. The complexities of natural landscapes limit the rigor with which process-based algorithms can be applied over entire regions. Interpreting passive microwave

satellite observations, particularly over land surfaces typically requires a mix of empirical-statistical and physically-based approaches.

IV. Algorithms

1. Soil and Land Surface Temperature

A. Multiple Regression Approach: Passive microwave T_b observations can be highly correlated with land surface temperatures (Pulliainen 1997; McFarland 1990); however, the correlation of T_b observations can degrade under various conditions, such as open water, snow cover, and changing atmospheric conditions. Multiple regression exploits the information contained in the different spectral and polarization responses of T_b for estimating land surface response to changing surface conditions and thus can improve the accuracy of land surface temperature estimates above what is obtainable from a single band. Multiple regression can produce accuracies similar to those from more sophisticated physical approaches (Pulliainen 1997). Although simple and often accurate, a significant drawback to multiple regression approaches are that such algorithms are only valid for the locations and sensor characteristics for where they were fitted and they do not give physical insight for improving estimates from future sensors, under different conditions, or over different regions with different land cover characteristics.

An empirical multiple-regression approach was applied to multi-frequency AMSR-E observations for retrieval of land surface temperature information (Jones 2007).

Two equation sets were developed. The first set consisted of two equations for estimating morning AM (descending overpass) soil temperature (< 5 cm) under thawed and frozen seasonal conditions. The second set contained three equations for temperature estimates for input into the VPD and soil moisture algorithms that were fit to daily screen height (~2 m) air temperatures under thawed conditions. Two equations used the descending (AM) overpass and the ascending (PM) overpasses fit respectively to minimum daily temperature (T_{min}) and maximum daily temperature (T_{max}) for determining VPD. The third equation used the descending (AM) overpass fit to the temperature at the time of satellite overpass (T_{am}) for determining effective emissivity for the soil moisture algorithm. The multiple regression coefficients were fit to several T_b channels and to index variables derived from those channels, such as the polarization difference ratio (ζ) (McFarland 1990; Njoku 1995; Pulliainen 1997) defined as:

$$\zeta = (T_{bv} - T_{bh}) / (T_{bv} + T_{bh}) \tag{9}$$

Such that the surface temperature (T_s) was described as a linear function of V-polarized T_b and ζ at various frequencies making up the columns of the design matrix **X**:

$$\mathbf{T_s} = \mathbf{X\beta} + \boldsymbol{\varepsilon} \tag{10}$$

The vector $\boldsymbol{\beta}$ contains model parameters and $\boldsymbol{\varepsilon}$ is a vector of errors between the T_s observations and model predictions. Index variables, such as ζ and channel differences, can be used to account for non-linearity caused by changing surface conditions that

cannot be described simply by the equation structure (Njoku 1995). Similar results can be obtained by incorporating H-polarization brightness temperatures in lieu of ζ.

The multiple regression algorithm was developed by stepwise forward selection on a full frequency set containing all bands of the V-polarized brightness temperatures and ζ values for each band as it was determined that the V-polarized brightness temperatures alone could not well account for surface wetness. At each step, the least significant term in the regression was dropped, where $p < 0.05$ was considered significant. The resulting equation was chosen when the root mean squared error (RMSE) of the estimate was not reduced by more than 0.5 K and the R^2 did not change significantly with the addition of another parameter. The results of the stepwise regression yielded the equation terms and parameters β tabulated in Table 3 and Table 4 for soil and near surface (~2 m) air temperatures, respectively. The model fit for soil temperature at all sites resulted in: $R^2 = 0.75$ and RMSE = 2.82 K for thawed conditions; and $R^2 = 0.48$ and RMSE = 4.68 K for frozen conditions. For T_{min} and T_{max} the model fit was $R^2 = 0.78$ and RMSE = 2.75 K and $R^2 = 0.89$ and RMSE = 2.99 K, respectively. For T_{sam} the overall model fit resulted in $R^2 = 0.85$ and RMSE = 2.65 K.

B. Freeze-Thaw Classification: The freeze-thaw transition can be identified through a change detection analysis of large (5-15 K) shifts in the AMSR-E T_b time series, which are pronounced at wet tundra sites. Other satellite microwave remote sensing studies have shown similar temporal behavior in microwave backscatter and emissions coinciding with temporal changes in land surface dielectric properties such as the landscape transitions between predominantly frozen and thawed conditions (Kimball 2001; Kimball

2004a; Kimball 2004b). This dynamic response is driven by the change in soil matrix dielectric as water transitions between solid and liquid phases, and the seasonal brightness temperature pattern for wet, cold lands (McDonald & Kimball 2005). An accurate freeze-thaw classification can be readily automated by applying the methods developed by McDonald (2004). However, to limit this potential source of error we identified seasonal freeze-thaw transitions through visual inspection of the AMSR-E time series data in conjunction with observed air and soil temperatures at each location. The spring (fall) transition was chosen when more air temperatures remained above than below (below than above) freezing in an 8 day period. A single classification was performed for each season.

C. Process-Based Approach: The aim of the process-based method is to reduce the dimensionality of the surface temperature problem by exploiting the expected frequency-dependence of AMSR-E brightness temperatures (T_b) to geophysical variables that influence the surface emissivity. This approach uses empirical parameters describing the frequency dependence of geophysical parameters within a simplified radiative transfer model (Jones 2007). In addition to surface temperature, additional parameters including vegetation water content/roughness equivalent and snow water equivalent parameters are simultaneously produced. Retrieved surface temperature and additional parameters represent linear spatial averages within the AMSR-E footprint.

The influence of the atmosphere was ignored when parameterizing the process-based method under the assumption that changes in apparent surface emissivity generally have a much stronger influence than the atmosphere over the study region even at

frequencies above 18.7 GHz. The high correlation of SSM/I satellite observations with concurrent soil brightness temperature observations from a ground-based radiometer on the North Slope of Alaska (Kim & England 2003) indicates that this is a reasonable first-order assumption. The main contributing atmospheric influence is columnar water vapor. As a result of colder atmospheres and low tropopause height, high latitude atmospheres generally contain less atmospheric water vapor than lower latitudes.

Across large regions of sub-Arctic Canada, Fily (2003) observed that apparent emissivities at H and V polarization were linearly related by empirical parameters *a* and *b*:

$$e_v = ae_h + b \tag{11}$$

In Arctic regions during summer, Fily (2003) showed e_h and e_v vary linearly between the emissivity of open water (approximately 0.57 for pure water at 20 °C observed at 6.9 GHz V-polarization) to that of dense vegetation over dry soil (approaching unity at V- and slightly less than unity at H- polarizations). A linear trend can therefore be fit to effective e_h and e_v data scatters to describe the expected change in emissivity with changes in open water fraction. Expressed in terms of surface temperature (T_s), (11) becomes:

$$T_s = \frac{T_{bv} - aT_{bh}}{b} \tag{12}$$

A variation of this simple relation with constant atmospheric parameters was used by Fily (2003) for surface temperature and water fraction retrieval in these regions using the 19 and 37 GHz channels on the SSM/I during summertime conditions. Matzler (1994) used another variation of (12) for temperature retrieval in Switzerland and Pulliainen (1997) used a variation for the Boreal forests of Finland. AMSR-E T_b observations over our sites show such a linear trend in effective e_h and e_v (Fig. 2); however, the value of the a and b parameters are clearly dependent on spatial and temporal variations in vegetation biomass among sites (Fig. 3).

An examination of T_b over the tower locations indicates that during both summer and winter, a and b have a dependence on vegetation density that appears to shift a towards unity and b towards zero from their typical thawed-condition values reported in Table 5. Whereas higher frequencies (>18.7 GHz) saturate quickly with even small amounts of vegetation, the lower bands (≤18.7 GHz) have a greater sensitivity to surface dielectric constant and therefore have a greater dynamic range of response to an overlying layer masking the surface. Winter snow has a similar impact on the apparent e_h and e_v relation, but the influence increases with frequency due to volume scattering within the snow pack. The influence of vegetation during the thawed season and of snow and sea/lake ice during the winter frozen season required a modification of (12) for frozen conditions.

BRW was used as a calibration site for a and b over quasi-specular surfaces, due to locally large swings in emissivity in response to the annual cycle of sea ice formation and retreat occurring within the BRW tower window. Although BRW is not an ideal calibration location because it contains vegetation during summer and snow/ice during

winter, the large amount of open water and relatively shallow snow pack reduces the overall impact of vegetation and snow on the calibration. During winter, the slope (*a*) of the calibrated H-V relation decreased relative to its summer value, while the intercept (*b*) increased relative to its summer value at sites with little vegetation. The specular values fitted to BRW were modified by radiative transfer for vegetation and snow cover.

A simplified radiative transfer model was applied to describe the modification of the *a* and *b* parameters by vegetation opacity. Njoku and Chan (2006) assumed $\omega_p \approx 0$ to produce a simplified parameterization of (4):

$$T_{bp} = T_s[1 - r_{sp}\exp(-\alpha(f)g)] \tag{13}$$

The canopy opacity (τ_c) is rewritten in terms of a frequency-dependent parameter, $\alpha(f)$, and a vegetation/roughness quantity (*g*) in equivalent kg/m^2. Values for $\alpha(f)$ were determined by extending the exponential relationship presented by Njoku and Chan (2006). By inserting (13) into (11) and solving for the surface temperature as in (12) we arrive at:

$$T_s = (T_{bv} - aT_{bh})/[1 - a - \gamma + \exp(-\alpha g)(b - 1 + a + \gamma)] \tag{14}$$

The addition of the empirical parameter γ was necessary to adjust the value of the denominator where the vegetation opacity becomes saturated. This parameter was set to a constant value of 0.012 and is added to partially account for extinction due to scattering

and the exclusion of ω_p in (13). As can be seen from (14) and (12), if the effect of vegetation is the same at both polarizations the influence of vegetation is entirely by modifying the intercept (*b*). This confirms that the apparent shift in the slope (*a*) with vegetation is caused by reduced sensitivity to the quasi-specular wet surface emission. The quantity *g* is an effective value that describes the average vegetation opacity over the satellite footprint, meaning that a footprint with a greater amount of open water will automatically have a lower value of *g*, even if the vegetation/roughness amount of the land fraction is equivalent to another pixel that contains less open water. The quantity *g* enters as an additional unknown and is determined using an iterative technique.

Additional terms for snow cover were added to the vegetation radiative transfer model for winter conditions. Snow pack radiative transfer was described using (6) and (7). In (7) the parameter b_{sn} is set constant at 0.025 and W_s was interpreted as a simple snow signal that includes the combined influence of snow pack water content, particle size, and total snow depth. As the purpose of this study is surface temperature determination, an effort was not made to define W_s in terms of actual snow-water equivalent as in other studies (Matzler 1994). By inserting (7) into (6), combining with (14) and solving for surface temperature as in (12), the expression for snow cover below a vegetation canopy becomes:

$$T_s = (T_{bv} - aT_{bh}) / \{B + \exp(-\alpha g)[\exp(-\tau_{sn})... \\ ...*[(1-a)(1-\omega_{sn}) + b\exp(-\tau_{sn}) - B]\} \quad (15)$$

where $B = 1 - a - \gamma$. Like g, the quantity W_s is an additional unknown and is determined using an iterative technique.

The radiative transfer equations (14) and (15) use a constrained, one-dimensional iterative minimization technique to solve for one of the additional quantities *g* and W_s with T_s, while holding the other parameter (*g* or W_s) constant. The quantities *g* and W_s were bracketed within some expected bounds (0 to 6 kg/m^2 and 0 to 10 cm, respectively). The physical temperature sensed by adjacent spectral bands is expected to be similar, so the weighted sum of squares of the pair-wise differences between the surface temperature estimated between adjacent bands was used as the cost function (Cf):

$$Cf = \sum_{k=2}^{N} \{[\hat{T}_s(k) - \hat{T}_s(k-1)]/\sigma(k)\}^2 \tag{16}$$

Where $\hat{T}_s(k)$ denotes the surface temperature estimated at band $(k-1)$ and $\sigma(k)$ is the weight for the k^{th} comparison summed over *N* bands. A golden section search with parabolic interpolation was used to minimize Cf. Surface temperature estimated at each frequency minimized Cf, and the quantities g and W_s were produced. All bands were employed in Cf as it was determined that the use of all bands gave the best overall results.

2. Daily Vapor Pressure Deficit

The vapor pressure deficit (VPD) algorithm takes advantage of surface temperature retrievals from descending (am) and ascending (pm) satellite overpasses and the assumption of equivalence between minimum daily temperature and the dew point. VPD and dew point temperature (T_{dew}) represent two measures of air humidity. The dew point (T_{dew}) is the temperature at which the air becomes saturated. VPD is the difference between the partial pressure of water vapor (e_a) in a parcel of air and the partial pressure of water vapor in an equivalent saturated parcel of air (e_s). The e_s of water vapor in Pascals (Pa) of a parcel of air under non-frozen conditions at T in °C can be approximated by Running & Waring (1998):

$$e_s = 6107.8 * \exp(17.269 * T/(237 + T)) \quad (17)$$

This relation can also be applied for determining e_a, and thereby VPD, by substituting T_{dew} for T.

The difference between air temperature and T_{dew} often decreases at night as a result of radiative cooling of the atmosphere near the land surface. At night, the air temperature often reaches T_{dew} at which point water is removed from the atmosphere as dew. In the absence of strong surface resistance to evaporation, T_{dew} tends to come into equilibrium with minimum daily air temperature (T_{min}) at night. T_{min} can therefore be used as an indirect measure for T_d over non-arid regions with relatively abundant surface water, conditions that are usually satisfied in high latitude regions (Kimball 1997a).

AMSR-E provides observations for twice daily overpasses with the descending (AM) overpass occurring near the time of daily T_{min} and the ascending (PM) overpass occurring near the time of daily T_{max} in the typical diurnal course of near surface air temperatures. An empirical regression algorithm (Section IV.1.A) was employed to retrieve T_{min} (T_{max}) information from AMSR-E descending (ascending) overpasses. The empirical regression algorithm was favored over the process-based approach for temperature retrieval because *i*) the parameters were easily tuned to represent T_{min} and T_{max} without more complicated modeling of the relation between soil surface skin temperature at the time of satellite overpass and T_{min} and T_{max}, and *ii*) the empirical algorithm produced better overall accuracy relative to temperature measurements at the study sites (Section VI.2.A). The maximum daily VPD was determined from AMSR-E retrieved T_{min} and T_{max} with (17) by assuming $T_{\min} = T_{dew}$ and that the maximum daily VPD was coincident with T_{max}.

3. Land Surface Wetness, Vegetation Phenology, and Open Water Fraction

Our approach solves for land fraction surface wetness and additional variables by employing a simple emission model and time-series techniques using the AMSR-E 6.9 GHz band. The method can be conceptualized as the inverse of the process-based surface temperature method. Instead of using iterative inversion of several bands to simultaneously produce T_s and vegetation biomass estimates, the surface wetness model employs empirical Ts retrievals and uses a time-series smoother to obtain vegetation optical depth. This approach avoids uncertainties in the frequency dependence of

emission processes and avoids employing higher-frequency bands that are more sensitive to surface scattering and atmospheric effects. Soil moisture is then determined by inverting the vegetation emission model in terms of soil emission. A flow chart of the land surface wetness algorithm and the other algorithms developed in this study is presented in Fig. 4.

A. Interpretation of Regional T_b Observations: H-V Histograms: We find it useful to develop the model by visualizing the impact of land surface conditions on plots of regional V-polarization T_b vs. H-polarization T_b (henceforth termed H-V space) with points from simple theoretical emission model predictions. Histograms of H-V space (1 K bins) for the Northern Hemisphere for 2003 reveals a roughly triangular shape (Fig. 5). The triangle will be termed the "H-V emissivity triangle" and its vertices are formed by pixels dominated by open water (OW), desert pixels devoid of vegetation (D), and pixels composed entirely of dense forest (F).

Notable features of H-V space for high frequencies (18.7 – 36.5 GHz) are snow, and atmospheric water vapor. Sea ice, glaciers, and other snow- or ice-covered regions scatter microwaves, reducing T_{bv} and increasing T_{bh}. These areas are marked SN in Fig. 5. Atmospheric water represents a region of high observation occurrence extending from OW. This region denoted WV (for water vapor) was confirmed to be associated with storm systems over the oceans. Due to WV's stronger impact at higher spectral frequencies it is likely related to the atmospheric water vapor absorption increasing T_{bh} and T_{bv} along the line OW-WV line above the ocean T_b background.

The emissivity triangle becomes more compact with increasing frequency, representing decreased sensitivity to open water, soil moisture, and saturation of bulk land surface by canopy emission. In other words, vegetation canopies are more opaque to higher frequency radiation, compressing the triangle along the base DF and reducing fluctuations in T_{bh} due to soil moisture. Increased scatter along a line between OW and D in the 6.9 GHz plots show soil moisture fluctuations, which relative to time-stable open water and vegetation conditions have a low frequency of occurrence over the course of the year, especially over areas with sparse vegetation. Soil moisture is also correlated with vegetation and therefore tends to fall within the triangle and is not visually separable from vegetation in the histograms.

T_b has a similar dependence on soil moisture and open water, but the dependence can be separated by considering the case of a pixel composed of a mix of open water, dry soil, and wet soil components. If the real portion of the surface dielectric constant (ε_r) is specified along an interval ranging from dry soil to open water (3.6-70), the Fresnel equations predict a concave-downward shape for T_{bv} as a function of T_{bh} (Fig 6). It can be seen from Fig. 5 and also from Fig. 2 introduced previously that observed data do not follow such a concave shape. In fact, the data are distributed linearly connecting open water to dry soil in Fig. 6 along line OW-D. If wet soil is added as a third component to the mix, the resulting point must always fall to the left of the line for the scene composed of only dry soil and open water (Fig. 6). This is because the pixel average dielectric of a scene composed entirely of wet soil is always less than the average dielectric of a scene composed entirely of open water. Therefore, a pixel with wet soil should have a T_b signature distinct from a pixel without wet soil in the presence of open water. The

presence of vegetation and roughness will foreshorten the line between dry and wet soil, and translate their relative position in an arc about the effective emissivity of open water.

H-V space gives an indication of the relative influence of surface components on the emissivity triangle; however, further interpretation is necessary to tie temperature-dependent H-V space to actual emissivity values and thereby calibrate the radiative transfer model for deriving surface information. In H-V space, rays of slope T_{bv}/T_{bh} extending from the origin represent changes in surface physical temperature at constant effective emissivity for window channels (recall (1)). Therefore the H-V plot represents translation of congruent triangles along these lines. The emissivity triangle can be described as a mix of land ($T_{b,land}$; emissivity varying from bare soil to dense vegetation) and open water ($T_{b,water}$; constant emissivity) components weighted by the fractional open water cover (f_w):

$$T_b = (1 - f_w) * T_{b,land} + f_w * T_{b,water} \tag{18}$$

For simplification, the pixel is assumed to have an averaged effective physical temperature of its land and water components, allowing (18) to be rewritten in terms of effective emissivities.

B. Algorithm Parameter Fitting: The term $T_{b,land}$ in (18) contains soil moisture and vegetation information and can be modeled using (4). The terms $e_{p\,water}$, and ω are considered as constant parameters, while the terms e_{sp} and r_{sp} are specified for dry baseline soil conditions. The ε_r of dry loam soil at the wilting point (~0.15 volumetric

moisture content) was modeled using the Dobson soil dielectric model (Dobson 1985) and the Fresnel equations were employed to determine e_{sp} and r_{sp}, which for low biomass conditions will correspond to point D in the H-V diagram. The constant terms were determined from H-V space as follows. We recognize from (12) that T_s can be determined from T_{bv} and T_{bh} through the constants a and b and in H-V space as T_s adjusts the intercept.

We assume that the bottom edge of the histograms denoted by line OW-F represents the freezing point of water (~273 K). This assumption allows values for the emissivity of open water and for the single scattering albedo of forest to be empirically determined. The emissivity of open water was determined by finding the lowest values of a T_{bh} and T_{bv} on a histogram for the entire Northern Hemisphere (Fig. 7) and dividing these by 273.15 K for the AMSR-E 6.9 GHz frequency. These results yielded the values $e_{v,water} = 0.586$ and $e_{h,water} = 0.289$. The single scattering albedo (ω_p) at 6.9 GHz was determined to be about 0.05 and independent of polarization (denoted ω). This value is within the range reported by several radiometer studies (van de Griend & Owe 1994; Pellarin 2006). If values of ω are considered < 0.05, (24) gives unreasonable values of τ_c (e.g. $\tau_c < 0$ or not a real number). The reasoning that ω is polarization independent for natural forest vegetation is supported by the fact that points in H-V space for forests are distributed along the 1:1 line (Fig. 5).

C. Water Fraction and Vegetation Determination: The first step in determining baseline water fraction and land fraction vegetation conditions is to estimate the effective emissivity using AMSR-E *Ts* retrievals and T_b observations. This effective emissivity

contains information from the respective land fraction and water fractions of the composite sensor footprint. The effective emissivity of open water at low frequencies is assumed constant and fit empirically. The effective emissivity of the land fraction is modeled using (4). Given a point of observed effective emissivities (e_p^*) for H and V-polarization, a line with slope ($\hat{a}$) and intercept ($\hat{b}$) is defined relative to the open water point (Fig. 6):

$$\hat{a} = \frac{(e_v^* - e_{v,water})}{(e_h^* - e_{h,water})} = \frac{(e_{v,land} - e_{v,water})}{(e_{h,land} - e_{h,water})} \tag{19}$$

$$\hat{b} = \hat{a} * e_{h,water} - e_{v,water} \tag{20}$$

This line further defines an intersection with line D-F representing the modeled emissivity of the land fraction ($e_{v,\,land}$) on the right side of (20) with specific soil moisture and vegetation water content.

In order to provide a stable algorithm, we employ only the 6.9 GHz band, and thus avoid the need for undesirable aspects of employing higher frequency bands with scattering and atmospheric effects. This allows the vegetation baseline to be left as a frequency dependent optical depth without defining a frequency dependent loss factor that relates frequency to vegetation water content, avoiding uncertainties in the canopy loss factor and its dependence on vegetation characteristics which could potentially be quite different from those values fitted for cropland (Jackson & Schmugge 1991) or the Sahel (Njoku & Chan 2006). Baseline conditions of τ_c were determined using by smoothing $\hat{a}$ with a 30-day moving window median smoother. This approach helps to

separate baseline conditions from soil moisture because seasonal vegetation/roughness changes are less time variant than the surface (< 2 cm) soil moisture signal at C-band as surface soil layers quickly wet during significant precipitation events in the absence of canopy interception and are closely coupled with the atmosphere. Furthermore, $\hat{a}$ shows minor sensitivity to soil moisture variability relative to other metrics such as the polarization ratio (e.g. T_{bv}/T_{bh}).

Vegetation optical depth (τ_c) was determined by inserting (4) into (11) and inverting. This gives τ_c in terms of a quadratic equation of the form $A\tau_c^{\,2}+B\tau_c+C=0$, where:

$$A = (1-\omega)*(r_{sv} - \hat{a}*r_{sh}) \tag{21}$$

$$B = \hat{a}*e_{sh} - e_{sv} + (1-\omega)[\hat{a}*r_{sh} - r_{sv} + 1 - \hat{a}] \tag{22}$$

$$C = (1-\omega)*(\hat{a}-1) + e_{v,water} - \hat{a}*e_{h,water} \tag{23}$$

And τ_c is determined using the standard quadratic formula:

$$\tau_c = \frac{-B - \sqrt{B^2 - 4*A*C}}{2*A} \tag{24}$$

Although two roots exist, (24) shows the only root that satisfies τ_c as a non-zero real number. The vegetation optical depth (τ_c) only applies to the land fraction of the sensor footprint in contrast to (12) in the process-based model where τ_c (determined from *g*)

applied to the entire pixel. This can be seen by remembering that *g* could only modify *b* in (12), whereas *a* is also allowed to vary with vegetation in (19).

Once τ_c was determined, open water fraction (f_w) could be calculated by:

$$f_w = \frac{(e_{v,land} - e_v^*)}{(e_{v,land} - e_{v,water})} \tag{25}$$

The V-polarization was used to reduce the dependence of the f_w estimate on soil moisture. The resulting f_w value was smoothed using a 30-day moving median filter similar to $\hat{a}$. It would have been preferable to use a moving minimum smoother to reduce soil moisture dependence; however, while soil moisture increases f_w at locations with little open water, atmospheric water vapor slightly decreases f_w at locations with much open water, and the median smoother was used to balance these biases between sites.

D. Wetness of the Land Fraction: Once baseline conditions of open water and vegetation were determined, the wetness of the land fraction was determined by re-employing the daily effective emissivities and the emission model. The land fraction emissivity was calculated for H-polarization:

$$e_{h,land} = \frac{(e_h^* - f_w * e_{h,water})}{(1 - f_w)} \tag{26}$$

The soil reflectivity (r_{sh}) was then calculated by inverting (4):

$$r_{sh} = 1 - \frac{e_{h,land} * \exp(\tau_c) - (1-\omega) * [1 - \exp(-\tau_c)]}{1 - (1-\omega) * [1 - \exp(-\tau_c)]} \quad (27)$$

Error in the estimation of land fraction r_{sh} introduced by estimating e_p^* with AMSR-E surface temperature increases with $1/(1-f_w)$ (Fig. 8). This requires that the variability of r_{sh} be dampened by the estimated open water fraction:

$$r_{sh,corr} = (r_{sh} - \bar{r}_{sh}) * (1 - f_w) + \bar{r}_{sh} \quad (28)$$

Where $r_{sh,corr}$ is r_{sh} with its variability dampened and $\bar{r}_{sh}$ is the long-term mean r_{sh} estimated for the pixel. The value $r_{sh,corr}$ roughly falls within bounds for bare loam soil between dry soil conditions (~0.05% volumetric moisture content) and saturation (~0.46% volumetric moisture content) modeled by the Dobson (1985) dielectric model. Values for $r_{sh,corr} < r_{sh,dry}$ were assumed to be the result of frozen soil or atmospheric absorption from precipitation and were eliminated. The *time series* for $r_{sh,corr}$ was then smoothed using a low-pass filter (Wagner 1999) and scaled between 0 and unity for each location. The resulting values were again scaled between 10 and 95 to account for dry soil (0.05% vmc is ~10% saturation).

4. NASA Operational L3 Soil Moisture Algorithm

The NASA AMSR-E operational global Level 3 algorithm data (Njoku 2004) are available from the National Snow and Ice Data Center (NSIDC). The algorithm relies on change-detection with dual-polarized low frequency observations with regression equations adopted from a simplified radiative transfer equation for vegetation-covered soil (Njoku & Chan 2006). Although the 6.9 GHz frequency on AMSR-E has greater soil moisture sensitivity, the 10.7 GHz frequency was used in the global algorithm to avoid radio frequency interference over populated areas in the 6.9 GHz band (Njoku 2005).

Monthly minima of the normalized T_b polarization difference ratio (e.g. ζ) at 10.7 GHz linearly interpolated between months ($\zeta_{min,interp}$) provides a daily lumped vegetation and roughness factor ($\overline{w}$), and also defines dry soil conditions (Njoku & Chan 2006):

$$\overline{w} = \beta_0 + \beta_1 * \log(\zeta_{min,interp}) \tag{29}$$

The vegetation and roughness factor ($\overline{w}$) is included in an exponential term that amplifies the change in the daily polarization ratio observations above the dry soil baseline to determine volumetric soil moisture (m_v):

$$m_v = \alpha_0 + \alpha_1 * \overline{w} + \alpha_2 * (\zeta - \zeta_{min,interp}) * \log(\alpha_3 * \overline{w}) \tag{30}$$

The β and α coefficients were determined from expected soil moisture regimes across transects of increasing vegetation biomass in moisture-limited regions (S. K. Chan, pers. comm.). As can be seen from (29) and (30) the algorithm does not explicitly account for open water fraction, but the use of the monthly minimum polarization ratio for determining a baseline reduces its influence.

5. Soil Moisture Models

A. Antecedent Precipitation Index: The Antecedent Precipitation Index (API) is simply a one day lagged auto regression of daily precipitation observations (P_i):

$$API_i = \gamma_l * API_{i-1} + P_i \tag{31}$$

Where the water loss coefficient (γ_l) is related to the evapotranspiration and infiltration properties of the soil and assigned a constant value of 0.85. The purpose for using API is two-fold: *i*) It indicates the "fast" response of the surface to precipitation wetting events (although not to snow pack thaw) and *ii*) the API has been used for regional scale satellite soil moisture validation to compensate for the lack of coarse-scale soil moisture observations, and gaining an understanding of how it compares to observed soil moisture at specific sites is crucial (Crow 2007; Crow & Zhan 2007).

B. BIOME-BGC Soil Water State: The soil moisture state variable derived from the Biome Bio-Geochemistry (BIOME-BGC) ecosystem process model was used to indicate

potential soil profile moisture conditions. BIOME-BGC simulates hydrological and ecological processes under the assumption that process rates are determined by climate and general plant functional characteristics (Running & Hunt 1993). The hydrologic portion of the model uses daily meteorological observations including T_{min}, T_{max}, and precipitation to predict evapotranspiration, soil outflow, snow water equivalent, soil water outflow, and integrated soil profile water content (Kimball 1997b). The water-holding properties of the soil layer are determined from specified soil texture, which were determined for each study location from a literature review (Oechel 1995; Griffis 2004; Flanagan 2005; Kwon 2006; Dunn 2006). The soil water content is fed by precipitation minus canopy interception and melting snow water equivalent, which accumulates from precipitation until the daily air temperature exceeds 1°C, at which point the snow pack ablates. The soil loses water to direct bare-soil evaporation and transpiration through the vegetation canopy. Soil water above saturation is drained into outflow. Below saturation, extra soil water is partitioned into outflow at half the previous rate until the soil reaches field capacity.

V. Validation and Inter-comparison of Algorithms

1. Soil Temperature

The *in situ* soil temperature data and corresponding daily T_b values were divided into a set for fitting algorithm parameters and a test set for evaluating algorithm performance. Days with missing soil or brightness temperature data were omitted from

the analysis (10.8 % of the entire test set). As the API and BGC models required continuous forcing data, precipitation information was gap-filled when not available for the site by scaling observations from an adjacent weather station to the ratio of long-term annual precipitation between the site and the adjacent weather station. The ATQ and IVO sites had relatively short duration datasets so these entire datasets were included in the test phase only, while for the other sites the entire year 2004 was set aside for algorithm testing. The remaining data for years 2002 and 2003 for five of the seven sites were used for fitting algorithm parameters. Daily AMSR-E soil temperature (T_s) retrievals for both retrieval methods under frozen and thawed conditions were compared to daily minimum soil (T_{soil}) and air temperatures (T_{min}).

MODIS Aqua night time Land Surface Temperature (LST; Wan 1999) 1 km x 1 km resolution grid subsets were extracted from ~60 km x 60 km windows centered at each tower site corresponding to the AMSR-E L2A spatial resolution. Since MODIS and AMSR-E are both located on the Aqua satellite, they have essentially coincident observation times. The mean and standard deviation of the 1 km x 1 km resolution, eight-day MODIS LST values were determined within each 60 km x 60 km tower window and used as a surrogate measure of sub-grid scale temperature variability for the corresponding AMSR-E microwave based temperature retrievals.

2. AMSR-E Air Temperature and VPD

The *in situ* air temperature and VPD datasets were divided into test and development sets as in the soil temperature analysis. Daily AMSR-E retrievals of T_{min},

T_{max}, and T_{am} were compared to the corresponding observed values at each study location. Evaluation of the AMSR-E VPD algorithm contained three components. First, an error propagation analysis was conducted to determine the amount of error introduced into the AMSR-E VPD estimates for 1, 2, and 4°C levels of root mean square error (RMSE) and for error levels determined in this study in the air temperature retrievals. Error propagation was also determined for error levels in T_{min} and T_{max} determined by this study. Errors in T_{min} and T_{max} retrievals were considered independent. Second, the VPD algorithm was run using the *in situ* T_{max} and T_{min} observations as inputs, instead of the AMSR-E retrievals, and compared against *in situ* VPD observations to test the amount of error that was introduced by the assumption of $T_{min} = T_{dew}$ alone. Third, the AMSR-E VPD results were compared directly to *in situ* VPD observations to determine the overall accuracy of the VPD algorithm at the study locations.

3. AMSR-E Soil Moisture

The analysis of this study takes the philosophy that the valuable component of soil moisture estimates are the relative correspondence of their anomalies, placing less emphasis their absolute accuracy. Other authors have convincingly argued that climatological modeling is best served by retrievals with high information contents rather than high absolute accuracy (Crow 2005). Perhaps the best way to accomplish this is in a data assimilation framework as in Crow (2007). Due to the exploratory nature of this analysis we chose to simply make comparisons using more traditional metrics, co-

registering units to coincident measurement scales, and putting more emphasis on correlations and frequency distribution correspondence more than relative bias.

Time series of *in situ* observations, model predictions, and satellite algorithm retrievals were examined for coherent temporal responses. Soil moisture modeled from *in situ* precipitation observations was employed to gain a better picture of the amount of soil wetness at each location. The Antecedent Precipitation Index (API) and BIOME-BGC soil moisture models were used to indicate soil surface and profile conditions, respectively. All satellite, model predictions, and *in situ* observations were scaled between minimum and maximum values for the observational period to produce values between 0 and 1. These values were then scaled again to vary between 10 and 95% to ensure that all observations and predictions were co registered to equivalent unit scales. The resulting quantities were expressed as proportional (%) units of saturation. Pair wise correlations and error statistics were calculated for each time series to gain an understanding of overall agreement among methods within each study location. Histograms of the sample frequency of observed, modeled, and retrieved values of soil moisture were constructed and compared to gain an understanding of the agreement between the distributional characteristics of soil moisture, model predictions, and satellite retrievals.

Retrievals of open water fraction and 6.9 GHz optical depth were compared to independent observations related to these factors at each study location. Maximum annual AMSR-E open water fraction was compared against open water fraction calculated from 60 km x 60 km window extractions of MODIS MOD-12Q1 1 km x 1 km resolution land cover maps centered over the study sites for each of the three observation

years (2002-2004). AMSR-E open water fraction was also compared to a Japanese Earth Resources Satellite (JERS-1) Synthetic Aperture Radar L-Band (1.23 GHz) mosaic open water fraction product binned to 25 km x 25 km EASE grid cells for the North Slope of Alaska. One EASE grid cell was extracted for each respective study site located on the North Slope of Alaska. These data were generated by Erica Podest and Kyle McDonald of the Jet Propulsion Laboratory, California Institute of Technology, Pasadena, California. Retrievals of 6.9 GHz optical depth were compared to extractions of MODIS MOD15A2 Leaf Area Index (LAI). These data represent 8-day composite 60 km x 60 km window means of 1 km x 1 km pixels passing the quality filter. A linear least squares regression analysis was conducted to compare retrieved 6.9 GHz optical depth to MODIS LAI.

VI. Results and Discussion

1. Landscape and Seasonal Signatures of T_b at the Study Locations

A. Land Cover Effects: Percent semi-permanent land cover determined by MODIS at the eight study sites is presented in Fig. 9. The MODIS land cover windows indicated that BRW, UPAD, and ATQ had the greatest amount of open water with 66 %, 30%, and 10% respective coverage (Fig. 9). NOBS had 9 % open water and OAS contained 8% open water, while the remaining locations had < 6 % open water. Tundra vegetation at BRW, ATQ, IVO, and HPV was classified as open shrubland, which varied in extent from 17 % at BRW to 96 % at HPV, and as grassland, which varied in extent from 60 %

at ATQ to < 1 % at the other tundra sites. Cropland coverage was dominant at LTH (59%) followed by grassland (34 %). Evergreen needle-leaved forest was dominant at NOBS (80%), but was also present at OAS (25%). The OAS window also had significant proportions of mixed forest (28%) and croplands (39%). MODIS detected urban areas at LTH and NOBS, but represented < 1% of the total window area.

B. Soil and Air Temperatures: The correlation between T_b and shallow (<20 cm) soil temperatures was greater than 0.75 for all AMSR-E spectral bands for sites without significant open water, as defined from the MODIS land cover windows (Fig. 11). The higher frequencies (23.8 – 89 GHz) were well correlated ($r \geq 0.70$; $P < 0.001$) with *in situ* temperature observations for all soil depths ≤22 cm in both forested and non-forested sites. The highest correlations were observed at the 89 GHz band, which was somewhat surprising considering expected greater sensitivity to the atmosphere; however, precipitable water and cloud liquid water content influence atmospheric opacity and emission at 89 GHz and also tend to be correlated with surface temperature and tropospheric lapse rates. A similar analysis was conducted over Finland (Pulliainen 1997) and found that the 85 GHz channel from the SSM/I showed lower correspondence with surface temperature relative to 37 GHz. The AMSR-E lower frequencies (≤18.7 GHz) showed significant, but generally lower correspondence ($r \geq 0.65$; $P < 0.001$) with air and soil temperatures for all sites.

In non-forested locations (Fig. 10a,b), the AMSR-E brightness temperatures showed greater correspondence to shallow (<20 cm) soil temperatures (r = 0.80-0.91) than minimum daily air temperatures (r = 0.65-0.85); however, in forested locations (Fig.

10c,d) the brightness temperatures corresponded more closely to minimum daily air temperatures (r = 0.91-0.95) than soil temperatures (r = 0.75-0.90). Differences in T_b correlations with minimum air temperatures measured above and below the OAS forest canopy were small, while both were greater than correlations with site-specific soil temperatures. The greater correspondence between T_b and air temperatures is due to the larger vegetation contribution to bulk surface microwave emission at the forested sites and soil temperatures insulated from below canopy air temperatures by additional leaf litter and a thicker humus layer. Figure 11 shows that the correlation of multi-frequency V-polarization T_b to air temperature (~2 m) at the time of the descending overpass followed the same general patterns as soil and minimum daily air temperatures.

Examples of 6.9 GHz brightness temperature time series and air and soil temperature traces for representative locations are presented in Fig. 12. Sites such as BRW, with a relatively large proportion of open water within the sensor footprint, showed a negative correlation between T_b and surface temperatures. The response was attributed to emissivity reductions from surface water. An increase in surface temperature leads to a decrease in T_b where ice is melted to form liquid water. Open water also increases the polarization ratio most strongly at lower frequencies, as indicated by the seasonal fluctuation of open water surface at BRW, whereas over vegetation, such as grassland at LTH, the difference between H and V brightness temperatures shows a decreasing trend during the growing season, the result of an increase in the depolarizing properties of a developing leaf canopy (Fig. 12).

C. Soil Moisture and Leaf Area Index: The correlation between AMSR-E simple indices and their expected direction for soil moisture and LAI are displayed in Table 6. Significant correlations ($p < 0.05$) and correlations of expected sign are shown in bold. For passive microwave remote sensing, soil moisture and vegetation have opposing effects on T_b, which is opposite to active microwave remote sensing (radar) where soil moisture and vegetation both increase backscatter (Wagner 1999; Prigent 2005). The indices at sites BRW, HPV, NOBS, OAS, and LTH all showed significant correlation with site soil moisture, although correlation at BRW and NOBS was relatively weak. Only LTH displayed significant correlations between LAI and all indices (r ranged from 0.39 to 0.57), while at OAS three of the five indices (T_{bh}, Tb_v/T_{bh} and T_{bv36}/T_{bh6}) showed significant correlation (r ranged from 0.23 to 0.42). T_{bh} had the highest correlation of the five indicies for both soil moisture and LAI with magnitudes ranging from 0.21 to 0.56 and 0.43 to 0.74, respectively. The correlation of T_{bh} with LAI dropped rapidly with increasing open water, while the relation for soil moisture also appears to decrease but not as strongly (Fig. 13). No clear trend of T_{bh} correlation to soil moisture and LAI with annual maximum LAI was observed, likely because the open water signal was the dominant factor reducing correlation, so locations with much open water automatically had lower correlation even if they also had lower LAI.

In general, sites that showed relatively strong correspondence with soil moisture (LTH and OAS) also showed significant correlation with LAI. The interpretation of this result is that the 6.9 GHz signal contains contributions from both vegetation and underlying soil at these locations, indicating the appropriateness of a two-layer radiative transfer model. HPV indices showed insignificant correlation to LAI ($p > 0.05$), likely

because the magnitude of seasonal LAI variability is much less than that for lower latitude grassland (LTH) and mixed forest (OAS) locations, yet AMSR-E observations at HPV were sensitive to soil moisture. The lack of strong correlation at BRW, UPAD, and ATQ is likely due to the dominance of the open water signal at these locations. The lack of strong correlation at NOBS is likely due to the dense evergreen forest land cover, masking soil emission and providing a T_b signature saturated by canopy emissions.

2. Surface Temperature Retrievals

Fig. 14 shows the overall thawed season results of the AMSR-E surface temperature retrievals and relevant statistics. The regression method was more accurate than the process-based method overall (RMSE = 3.11 K vs. RMSE = 3.93 K). Fig. 15 shows time series of soil temperature retrievals at each of the study locations. The corresponding statistical results are summarized in Tables 7 and 8 for thawed and frozen conditions, respectively. Both methods are generally able to capture the annual cycles and daily variability of soil and air temperatures at each site. More favorable results are obtained during the summer thawed season relative to winter frozen conditions. The use of the 89 GHz in estimating T_s did not degrade the retrievals in either of the AMSR-E T_s methods. The T_s results for the process-based method for each frequency were nearly equivalent where the value of Cf was low.

Several instances of either systematic bias or anomalous, short-term spikes or dips in AMSR-E retrieved T_s are worthy of detailed discussion (Fig. 15). Correspondence of AMSR-E T_s with T_{soil} and T_{min} varied among sites as the latitudinal range of the sites

presented different soil-to-air temperature gradients at each location. Sub-pixel spatial heterogeneity was also a significant factor for the microwave T_s retrievals. The freeze-thaw transition and snow during the winter season significantly impacted winter retrievals. Land cover characteristics, such as open water and vegetation phenology, presented a range of temporally dynamic and spatially variant emissivities within and among sites. The accuracy of the temperature retrievals under these conditions indicates the skill of the retrieval method to account for these dynamic effects.

A. Comparison to *in situ* Air and Soil Temperatures and MODIS LST: The process-based approach obtained lower errors at the Arctic sites relative to the Boreal locations with the exception of HPV (RMSE<3 $^{\circ}$C vs. RMSE>3 $^{\circ}$C; Table 7). This demonstrates the model correctly accounts for changes in surface emissivity in response to open water surfaces which dominate regional land cover conditions at higher latitudes. The regression method also performed well over the Arctic tundra sites, but had higher error at HPV. The somewhat poorer performance of both methods for HPV relative to IVO, another tussock tundra site, can be partially attributed to erroneous predictions during the freeze-thaw transition which were more severe at HPV. For both the IVO and HPV tussock sites the regression method consistently over-predicted T_s (MR= -3.71 $^{\circ}$C and -4.43 $^{\circ}$C respectively). The overestimation at the tussock sites was therefore attributed to ζ similar to forested sites, but the thermal gradient between soil and canopy temperatures was much different than forested sites as shown in Section VI.2.A and Fig. 10. IVO and HPV have ζ that was more similar to the Boreal forest sites than to the grassland site, LTH, despite the short stature tussock tundra vegetation. The summer

minimum ζ at 6.9 GHz varied from 0.0107 at IVO, 0.0099 at HPV, and 0.0112 at NOBS, to 0.0149 at LTH. Anisotropy of tussock tundra has previously been noted in (Kim & England 2001; Kim 2007 pers. comm.). The regression method had generally less bias over the Boreal sites relative to the process-based method.

Bias can be explained by the near-surface soil-to-air temperature gradient. Summer soil temperature observations at the high latitude Arctic sites were only slightly warmer than the daily minimum air temperatures. These daily temperature differences increased for lower latitude Boreal locations, with the greatest average difference of about 5°C occurring during mid-summer conditions at LTH. Maximum daily differences between T_{soil} and T_{min} decreased with increasing latitude and ranged from 24 °C for LTH to 9.65 °C at BRW. These differences reflect stronger surface heating and larger diurnal temperature gradients at drier, lower latitude locations; these conditions impact the soil temperature comparisons by increasing surface temperature spatial and vertical heterogeneity, and decreasing the correspondence between relatively coarse scale AMSR-E based T_s and *in situ* soil temperature measurements. In contrast, reduced solar irradiance at higher latitudes and the relatively large heat capacity of water and enhanced latent energy transfer in areas with large amounts of surface water moderates T_{min} and T_{soil} differences for tundra sites. As a result, the AMSR-E process-based retrieval method underpredicted soil temperatures at OAS and LTH relative to *in situ* measurements (Table 7). The bias is removed or reversed when the retrieval is compared to T_{min}, indicating the bias was mostly the result of the near-surface soil-to-air temperature gradient and not assumptions in the vegetation model. The greater under prediction at OAS and LTH might also be attributed to soil moisture variability at these locations, as

the process-based approach did not seek to separate the influences of open water and soil moisture. The under prediction was greatest with the process-based approach relative to the regression method because the coefficients of the regression approach were tuned to the soil temperature when the equation coefficients were established.

The relatively coarse scale AMSR-E results from the two approaches are in general agreement with the footprint mean LST derived from MODIS. MODIS LST shows that mean surface skin temperatures within the AMSR-E field-of-view generally correspond more closely to T_{min} rather than soil temperature, due to the descending (morning) overpass time and shallow penetration depth. At the tundra locations (BRW, ATQ, and HPV), MODIS LST shows generally colder temperatures relative to T_{min} and both AMSR-E T_s methods. The standard deviation of the LST within each pixel ranges from <1°C in winter to 11°C during the fall freeze-thaw transition. Summer season LST pixel standard deviations are ~3.6°C at the Arctic sites and ~2.7°C at the Boreal sites. These values suggest that LST spatial heterogeneity within the tower windows is on the order of the AMSR-E-based temperature accuracy determined from pixel-to-point comparisons with *in situ* observations during the thawed season.

B. Winter Retrievals and the Freeze-Thaw Transition: The onset of winter induces rapid changes in surface dielectric properties during the transition to frozen conditions. Soil to air temperature gradients and the accumulation of a scattering snow pack are also important factors. It is therefore not surprising that the AMSR-E based temperature retrievals significantly degrade during the winter months. A marked increase in retrieval error during freeze-thaw transitions was evident for the process-based method (Fig. 15).

This error was more severe during the fall than in spring because the seasonal thaw transition generally occurred rapidly, while the transition to seasonal frozen conditions was more gradual, with multiple freeze-thaw events occurring over a relatively long duration. The erroneously high temperature retrievals between late September and early October at ATQ and HPV indicate that this effect is strongest at tundra sites (Fig. 15). The relatively simplistic freeze-thaw classification approach used for this investigation does not account for spatial heterogeneity or multiple freeze-thaw events occurring within the sensor footprint. Also, freeze-thaw state varies within each ~60 km x 60 km microwave footprint during the transition. An earlier study on the North Slope of Alaska compared tower-based 37 GHz brightness temperatures and SSM/I observations, concluding that the satellite- and ground-observed brightness temperatures differ as a result of spatial heterogeneity in landscape dielectric properties during the seasonal freeze-thaw transition (Kim & England 2003).

Snow cover also impacts the AMSR-E temperature retrievals of both methods by insulating soil temperatures. As can be seen from Figure 15, the AMSR-E temperature retrievals correspond more closely to minimum daily air temperatures and MODIS LSTs than soil temperatures for sites under seasonal snow cover for the process-based approach. A similar pattern is evident at NOBS, where soil temperatures fluctuate near 0.0°C, while air temperatures range as low as -40°C. The positive bias relative to *in situ* temperature measurements at BRW (MR = -6.6°C; Table 8) is also the result of the regression equation representing an insulating snow pack that was present at most of the other sites (Fig. 15).

C. Evaluation of Additional Parameters from the Process-Based Method: The accuracy of the process-based T_s retrieval under temporally dynamic surface conditions indicates the skill of the method to account for the effects of changing emissivities. The assumption of a linear relation between T_{bh} and T_{bv} accounts for changes in surface bulk dielectric constant. As stated earlier, this relationship is related to the scale of the microwave observations over quasi-specular surfaces and appears to shift with surface freeze-thaw state and does not separate open water and soil moisture influences. Earlier studies have used this relation for surface temperature retrieval at both site (Matzler 1994) and regional scales (Fily 2003); however, the impact of the absorption of quasi-specular surface emissions by vegetation and volume scattering within snow pack required the use of simple radiative transfer equations to describe the behavior of the polarization difference over these surfaces. In addition to surface temperature, the inversion of these equations enabled the retrieval of canopy water content/roughness equivalent (g) and a snow-water equivalent parameter W_s.

The results for the g parameter are given in Fig. 16 and indicate that g corresponds closely with variations in the 8-day MODIS leaf area index (LAI) among the sites, as well as the seasonal trends at each site for 2003. One anomalous spike in g at ATQ in 2003 (Fig.16) during the fall freeze is similar to such a spike in 2004 causing over prediction of T_s during the fall freeze (Fig. 15). The influence of g is to modify the b parameter in (12), increasing the predicted surface temperature. The surface temperature prediction at 6.9 GHz is most sensitive to the influence of g because this band is most sensitive to surface water and thus will have a greater relative response to the masking of the underlying surface, whereas the 89 GHz band saturates quickly with even a small

amount of vegetation. The best T_s results were obtained by employing all bands equally weighted in the iterative minimization. When only the highest frequency bands (18.7 to 89 GHz) were included, T_s was over predicted and retrieved values of g approached 6 kg/m^2 at NOBS, which was assumed unreasonable for Boreal forest given the results of (Pulliainen 1997). Similarly, when only the lowest bands (18.7 GHz and less) were included, T_s was under predicted. The inclusion of a more detailed radiative transfer equation, such as (4), may further improve results by accounting for scattering effects. However, the surface temperature results of this investigation show that bias introduced by scattering within the vegetation canopy is a relatively small factor and can be mitigated with the empirical parameter γ.

In contrast to a vegetation canopy, scattering is the main effect of snow cover on the linear relation between T_{bh} and T_{bv}. Scattering decreases the T_s estimates from (6) more strongly at higher frequencies relative to lower frequencies, which is the opposite spectral effect of vegetation absorption. This poses a difficulty for the current algorithm where vegetation persists above the snow pack in winter, such as the Boreal forest at NOBS and OAS (Fig. 17). The opposing effects of vegetation and snow on predicted T_s cause g to unreasonably decline to zero during winter at the NOBS evergreen forest site and gives an unreasonably low estimate of W_s, rising only above zero when the snow pack scattering spectral signal is strong enough to overwhelm the vegetation absorbance spectral signature. This pattern is also evident at the OAS site where W rises only briefly above zero, corresponding to the peak depth of the *in situ* snow pack observation. Some of the error in the process-based winter T_s retrieval can be attributed to this effect because

minimizing Cf can not arrive at an unbiased T_s estimate when a portion of the spectral signature is confounded by the vegetation effect.

Snow packs also vary greatly in their physical characteristics (Matzler 1994) and the simplistic treatment in this study does not account for changes in snow grain size, the formation of ice lenses and associated impacts on the extinction and scattering coefficients influencing ω_{sn} and b_{sn}, which were held constant in this investigation. However, the radiative transfer treatment of the snow pack did produce a clear snow signal (Fig. 17). We lacked ground data on snow for most sites in this study with the exception of BRW and OAS; however, the snow signal shows the expected seasonal pattern, accumulation throughout the winter, peaking before a rapid decline in spring.

3. Air Temperature Retrieval Validation

The overall retrieval accuracies across sites for T_{am} (RMSE = 2.82°C) were slightly lower than for T_{min} (RMSE = 2.88°C), which was much more accurate than for T_{max} (RMSE = 3.31°C). These results are expected given that T_{am} corresponds more closely to the AQUA overpass time than does T_{min}. Steep near-surface temperature gradients from solar heating in the afternoon increase spatial heterogeneity and reduce the accuracy of T_{max} relative to T_{min}. The overall accuracy for T_{am} and T_{min} was also an improvement over the soil temperature accuracy for the same overpass (RMSE = 3.10 °C).

Site-specific results for T_{max}, T_{min}, and T_{am} retrievals are presented in Table 9. Site-specific accuracies and biases are graphically presented in Fig. 18 and Fig. 19,

respectively. Relative retrieval accuracy among sites was similar across all air temperature estimates and regressions derived soil temperatures, but was different from the process-based soil temperature estimates, which show a general pattern of decreasing accuracy with latitude (Fig. 18). Bias in the air temperature retrievals does not show any specific patterns among sites, with the exception of UPAD, displaying under prediction in all instances (Fig 19). Bias in soil temperatures did show a pattern between sites, which was previously discussed.

A. Effective Emissivity Accuracy for LSW Algorithm: The overall accuracy of effective emissivities calculated from AMSR-E T_{am} relative to those calculated from observed T_{am} were (RMSE=0.0089 and RMSE=0.0081 for e_v and e_h, respectively). The greatest error in effective emissivities was at HPV with (RMSE=0.0012 for both e_v and e_h). The overall effective e_h standard deviation for sites with <10% open water is 0.0248, so the uncertainty in estimating effective e_h overall from AMSR-E is low relative to the variability in effective e_h calculated from site observations. For NOBS the variability in e_h is sufficiently low (stdev. = 0.0137) that effective e_h estimation can overwhelm any soil moisture signal contained in e_h. In general, the estimation of effective e_h does not pose a significant source of error for soil moisture estimation because locations with low e_h variability, which are areas contributing mostly canopy emission (such as forests) have low intrinsic sensitivity to soil moisture.

B. Correlation of Error Between T_{min} and T_{max} Retrievals: Residual errors for T_{min} and T_{max} were significantly ($p < 0.001$) correlated at four of the eight locations. The

greatest residual correlation was at HPV (r = 0.44), followed by ATQ (r = 0.40), OAS (r = 0.37), and LTH (r = 0.30). The significant correlations between T_{min} and T_{max} residuals were always positive; indicating that T_{min} under prediction (over prediction) was associated with T_{max} under prediction (over prediction). This situation indicates that the influence of correlated AMSR-E T_{min} and T_{max} errors will tend to introduce bias, into the VPD retrievals rather than inaccuracy. For ATQ the mean residual was positive for both T_{min} and T_{max} (1.5°C and 1.95°C, respectively) and for LTH the mean residual was negative for both T_{min} and T_{max} (-0.51°C and -0.76°C, respectively). The MRs were in opposing directions for the other locations with positive residual correlation, indicating that introduced VPD bias could be either positive or negative for HPV and OAS (Fig. 19).

4. Vapor Pressure Deficit Algorithm Validation

A. VPD Error Sensitivity Analysis: The error analysis for daily maximum VPD is presented in Fig. 20. The amount of error introduced into predicted VPD from uncertainty in both T_{min} and T_{max} is dependent on the magnitude of VPD. Error increases with increasing temperature and VPD, so the smallest errors occur at the lowest temperatures and lowest VPD and the largest error is introduced at the highest temperature and highest VPD. Range in VPD error for error in estimated surface temperature (δT) are 189 to 816 Pa for δT = 1°C. Range in VPD error for δT = 2°C is 243 to 851 Pa VPD and the range in VPD error for δT = 4°C is 425 to 980 Pa.

Meaningful VPD information can be derived for sites with mean annual VPD greater than 216, 276, and 490 Pa for δT = 1°C, 2°C, and 4°C, respectively (Fig. 20c).

B. VPD Algorithm Evaluation: The results for VPD retrieval are shown in Table 10 and in conjunction with overall T_{min} and T_{max} results in Fig. 21. The overall accuracy of the AMSR-E VPD retrievals were RMSE = 427.9 Pa (R^2 = 0.71), whereas the overall accuracy of the VPD algorithm run on the site meteorology was RMSE=307.4 Pa (R^2=0.86). The bias for AMSR-E VPD was 4.8 Pa vs. 46.6 Pa for the VPD algorithm run on the site meteorology. The scatterplots in Fig. 21 indicate that the bias in VPD predicted from site meteorology was introduced at higher levels of VPD (e.g. drier days and locations). Similar bias is visible in the AMSR-E retrievals (Fig. 21), but appears reduced due to error introduced by the surface temperature estimation.

Site specific VPD accuracies are presented in Fig. 22 and Table 10. Site specific results also show that more error is introduced into VPD at lower latitudes, although the forested sites showed somewhat more error in VPD than the grassland location (LTH). These two general patterns were independent of meteorology used to drive the VPD estimates. Fig. 23 shows that both AMSR-E VPD and VPD estimated with site meteorology tend to under predict VPD at the Boreal locations, but also tend to over predict VPD at the Arctic locations. This pattern can mostly be attributed to the underlying assumptions of the VPD algorithm and not to error in surface temperature retrievals, because the VPD algorithm run on the site meteorology shows the same pattern. The under prediction at the southern sites is an expected consequence of violations of the underlying assumption of $T_{min} = T_{dew}$ when the air is especially dry;

however, the over prediction at the Arctic sites is somewhat unexpected and indicates the air is generally wetter than one would expect if $T_{min} = T_{dew}$.

The comparison of VPD estimates using the site meteorology vs. VPD estimates using AMSR-E indicate the relative amount of VPD prediction error introduced by AMSR-E meteorology was 28.2% of the overall error in the AMSR-E VPD estimates across sites. This shows that the bulk of the error (71.8%) is in the underlying assumptions of the VPD algorithm, which is corroborated by the systematic offsets for Boreal vs. Arctic regions. Site-specific results for relative error introduced by AMSR-E are presented in Fig. 24. Contributions of AMSR-E meteorology to overall VPD error varied from 11.01% at OAS to 47.58% at LTH. Sites where the relative amount of error between site and AMSR-E meteorologies was high did not tend to be sites where VPD was also high. These results show that AMSR-E meteorology represents half or less of the error introduced in the AMSR-E VPD estimates, with the remaining error attributable to the underlying assumptions of the algorithm.

5. Land Surface Wetness and Baseline Land Surface State

A. Open Water Fraction: Comparisons of maximum annual open water fractions retrieved from AMSR-E to JERS-1 radar mosaic and MODIS land cover derived open water fractions are displayed in Fig. 25. The accuracy of AMSR-E open water fraction was greatest relative to MODIS (RMSE = 0.10) and slightly less favorable relative to JERS-1 (RMSE=0.18). AMSR-E estimates showed overestimation relative to both methods with MR=-0.13 for JERS-1 and MR=-0.06 for MODIS. The AMSR-E

overestimation relative to JERS-1 and MODIS was controlled by locations with the greatest open water fractions (ATQ, UPAD, BRW). AMSR-E estimates for the remaining locations, all with $f_w \leq 0.10$, did not show noticeable bias. All three open water fraction methods show the same relative amounts of open water between sites with the exception that JERS-1 estimates more open water for ATQ (0.29) relative to UPAD (0.20), whereas both AMSR-E and MODIS predict greater open water fraction at UPAD (AMSR-E f_w = 0.44-0.49; MODIS f_w = 0.30) than ATQ (AMSR-E f_w = 0.29-0.30; MODIS f_w = 0.10).

The inter-annual variability in open water fraction estimated by AMSR-E among the three years of observation (2002-2004) ranged up to 0.06 at LTH. The inter-annual variability at UPAD was 0.05 for the greatest inter-annual variability of a site with $f_w > 0.1$. It is important to note that the use of a moving window smoother may introduce inter-annual variability in AMSR-E estimated f_w that is actually related to long-term soil moisture levels than variability in open water fraction. The three methods of estimating open water fraction also represent different window sizes and shapes relative to each other. This difference can explain the modest accuracy against JERS-1 compared to that against MODIS, where the MODIS 60 x 60 km window more closely resembles the oblong (75 km x 43 km) AMSR-E footprint than does the JERS-1 binned 25 km x 25 km EASE grid cell open water product. The difference in cell size is also consistent with the greater deviations between methods at sites with more open water, as locations with more open water represent landscapes with greater heterogeneity.

Time series of AMSR-E open water fraction presented in Fig. 26 show seasonality in open water fraction across sites. Open water fraction is generally stable

throughout the thawed season except for sites along the coastal Arctic Ocean (BRW and UPAD). These two coastal locations both show increases in open water fraction from the spring thaw date to a maximum in late August and early September. The ~60 km x 60 km 6.9 GHz AMSR-E footprint can contain a significant ocean fraction in coastal areas. The timing of maximum annual open water fraction corresponds with the typical timing of annual minimum Arctic Ocean sea ice extent (Comiso 2003). Even if the ice edge itself has retreated offshore, ice floes and bergs may contribute significantly to reduction in open water fraction throughout the thawed season.

B. Vegetation Phenology: Retrievals of baseline landscape conditions of 6.9 GHz optical depths compared to MODIS LAI are shown in Fig. 27. All locations with <11% open water fraction show significant positive trends with LAI (Table 11). Locations with >11 % open water fraction show significant negative relationships with LAI at BRW ($p < 0.01$) and a relatively weak negative relationship at ATQ ($p < 0.05$). These two locations have small LAI ($\leq$1.6 m^2 m^{-2}) relative to IVO and HPV (LAI $\leq$2.6 m^2 m^{-2}), two other locations that have land fractions with similar land cover classes as BRW and ATQ, but displayed positive trends with LAI. Open water fraction and optical depth should not be significantly correlated from the algorithm formulation, so this result is somewhat unexpected; however, the combination of low LAI and location in HV-space close to the open water point (e.g. T_b signal dominated by T_b signal from water) add considerable uncertainty into the estimation of optical depth at these locations and especially at BRW with ~80% estimated open water fraction.

The regression slopes for grassland (LTH) and tussock tundra (IVO and HPV) are greater than those for the forested locations (NOBS and OAS). This gives the appearance of an overall logarithmic-shaped relationship between LAI and optical depth (Fig. 27), with optical depth saturating at higher levels of LAI (3-5 m^2 m^{-2}). Optical depth is usually assumed to be linearly related to vegetation water content in low-frequency microwave remote sensing as seen in (5). Wen and Su (2004) suggested that vegetation water content displays a logarithmic relationship with LAI. These conjectures are both consistent with our results.

The appearance of the 6.9 GHz optical depth vs. MODIS LAI plot (Fig. 27) closely resembles a figure of SeaWinds on Quickscat Ku-band (13.4 GHz) backscatter (σ^o) in dB vs. MODIS LAI plot produced for North America (Fig. 2 in Frolking (2006)). Each land cover type occupies the same relative position and has the same relative slope magnitudes on the AMSR-E 6.9 GHz optical depth plot as compared to the SeaWinds 13.4 GHz backscatter plot. This result provides an empirical link between passive and active microwave remote sensing observations of vegetation phenology. This link provides a potentially promising avenue for passive/active microwave synergy for land surface parameter retrieval particularly relevant to future passive/active satellite missions.

Time series traces of AMSR-E 6.9 GHz canopy optical depth (τ_c) and MODIS LAI are shown in Fig. 28. Time series of the AMSR-E NASA L3 soil moisture algorithm baseline parameter ($\overline{w}$) derived from interpolated monthly minima of the 10.7 GHz polarization ratio (ζ) are shown in Fig. 29. The τ_c relative magnitude and seasonal timing of peak conditions between sites corresponds well with the relative magnitude and peak timing of MODIS LAI between Boreal sites. The values of τ_c at the tundra

locations relative to other sites are higher than the values of LAI at the tundra locations relative to other sites. This indicates greater microwave canopy loss per unit of LAI over tundra canopies relative to grass or forest canopies, which could potentially be caused by absorbance of microwave emission by low-bulk density wet organic material and litter for tundra.

Over locations with little open water τ_c and $\overline{w}$ are correlated, although over locations with significant open water (ATQ, UPAD, and BRW) $\overline{w}$ shows a seasonal trend inverted relative to the trend shown by τ_c and LAI. The $\overline{w}$ parameter results are much lower for NOBS than for HPV and IVO in contrast to τ_c, which showed relatively higher results for forested NOBS than for the tundra sites HPV and IVO. Both of these differences between $\overline{w}$ and τ_c trends is caused by open water increasing the 10.7 GHz monthly minima and decreasing the $\overline{w}$ bar parameter at the tundra sites with open water and densely forested NOBS, which would otherwise be expected to have a high $\overline{w}$ parameter were it not for the ~10% open water at this site.

C. Land Surface Wetness Results: The results of the soil moisture model-algorithm inter-comparison are presented in Figure 30 and pair wise statistics can be found Tables 12a-12d. The two AMSR-E algorithms showed favorable correspondence with observed soil moisture at three of the six study locations for which soil moisture was available ($r > 0$; $p < 0.001$). Correlation coefficients for these locations for the NASA L3 algorithm ranged from $r = 0.76$ at HPV to $r = 0.40$ at LTH with intermediate correlation at OAS ($r = 0.54$). For the LSW algorithm, correlation was higher at LTH ($r = 0.64$), somewhat lower for HPV ($r = 0.49$), and non-significant at OAS ($r = 0.15$).

At OAS, the LSW algorithm was significantly correlated with the API model (r = 0.48), while the correspondence with API was non-significant for the NASA L3 algorithm (r = 0.13), although the API and soil moisture observations were correlated (r = 0.42). At LTH and HPV, the two algorithms both correspond significantly with API (Tables 12c and 12d). Relatively weak correspondence was also observed between the LSW index and both API and BGC modeled soil moisture at ATQ, r = 0.219 and r = 0.238, respectively. The L3 algorithm showed weak correspondence to BGC soil moisture at BRW and UPAD (r = 0.28 and r = 0.36, respectively), but not to either soil moisture or API at these two locations. No correspondence was detected between LSW to either the site observations or the model results at these two locations. Additionally, the two AMSR-E algorithms did not correspond to either the site soil moisture observations or the model results at NOBS and also at IVO.

Locations where the NASA L3 Algorithm and the LSW showed correspondence to site and modeled soil moisture, the two algorithms also showed correspondence to each other, including HPV, OAS, and LTH (Tables 12c and 12d). The BGC and API results showed correlation in these three locations with soil moisture and generally with each other (with the exception of HPV). Where the NASA L3 Algorithm and the LSW showed no correspondence to site and modeled soil moisture, the two algorithms did not correspond to each other. At two of these locations, BRW and NOBS, the BGC and API results showed significant correlation with soil moisture and each other. At UPAD, BGC and API results corresponded with each other, but not with observed soil moisture. The models and AMSR-E algorithms did not show any correlation with each other at IVO (Table 12b). This result could have been caused by a relatively large number of missing

precipitation data points at IVO (103 days missing out of 312 daily observations or 33.0%).

The absolute accuracy to site soil moisture observations was more favorable for the LSW algorithm at sites where the algorithms showed significant correspondence. The lowest error was at LTH (RSME = 20.2% of saturation) for the LSW algorithm. This corresponds to ~0.091 m^3m^{-3} error in volumetric soil moisture content (VMC) for loam soil (composed of 30% clay, 60% silt, and 30% sand). The RMSE for the LSW compared to the API and BGC models at LTH were more favorable (15%, e.g. ~0.068 m^3m^{-3} VMC) and 17.3 % (~0.078 m^3m^{-3} VMC), respectively. The error for LSW compared against API at OAS was 16.5 % (~0.074 m^3m^{-3} VMC). The error for LSW compared against site observations at HPV was 27 m^3m^{-3} (~ 0.12 m^3m^{-3} VMC), and compared against API was 20.1 % (~ 0.091 m^3m^{-3} VMC). The pre-launch accuracy of soil moisture retrieval from AMSR-E was estimated at ~0.06 m^3m^{-3} (Njoku 2003) and is expected to be ~0.04 m^3m^{-3} for L-band radiometers planned for the near future (Kerr 2001; Entekhabi 2004).

The accuracy for the NASA L3 algorithm was much more modest than for the LSW algorithm for most locations. The L3 algorithm had the lowest error compared to site observations at OAS (RMSE = 26.8% or ~ 0.12 m^3m^{-3} VMC). The accuracy of the L3 algorithm was 29.7% (~ 0.13 m^3m^{-3} VMC) at LTH and was greatest at HPV, despite relatively high correlation (r = 0.76), with 41% (~ 0.18 m^3m^{-3} VMC). The L3 product showed much improved accuracy when compared to API (RMSE = 15.7% or ~0.067 m^3m^{-3} VMC for both HPV and LTH).

The modest accuracy of the L3 product was driven by strong low bias as evidenced by the low values for the slope statistic relative to those for the LSW algorithm. For LTH the slope statistic was 0.42 for LSW and 0.18 for the L3 product and at HPV the slope statistic was 0.30 for LSW and 0.13 for the L3 product. These results indicate under prediction of soil moisture values for the two algorithms, but the under prediction was especially acute for the L3 product and subsequently produced modest values for overall accuracy indicated by the large RMSE statistics. This characteristic of the L3 algorithm has been noted by others for the central United States (Wood 2006; Crow 2007). Under prediction was persistent even after scaling the soil moisture values to equivalent scales, indicating fundamentally different properties in the distributional characteristics of both satellite prediction methods compared to those of observed <10 cm soil moisture (Fig. 32).

By comparison, Wagner (2006) obtained RMSE values of 0.12 m^3m^{-3} VMC for the AMSR-E L3 soil moisture product compared to soil moisture observations (~2-8 cm) over Mediterranean vegetation in arid central Spain. Wagner (2006) also obtained a value of 0.091 m^3m^{-3} VMC for the AMSR-E soil moisture algorithm described in Owe (2003), a value of 0.10 m^3m^{-3} VMC for the ERS C-Band Scatterometer product (Wagner 1999), and a value of 0.099 m^3m^{-3} VMC for a METEOSAT product based on an optical-infrared thermal inertia approach described in Verstraeten (2006). Few additional published studies have compared the accuracy of operational AMSR-E to soil moisture observations distributed across regions of natural land cover.

D. Soil Wetness Seasonality: Time series of daily soil moisture results are presented in Figure 31. The correspondence of the AMSR-E soil wetness products to wetting events indicated by *in situ* soil moisture observations and the models is evident at HPV, OAS, and LTH. The LSW algorithm appears to show some response to mid-summer wetting events for all of the tundra locations, although the statistics were not significant. A coherent time signal appears in mid-summer between tundra locations, linking HPV, where AMSR-E LSW showed significant correspondence to soil moisture, to the other tundra sites where AMSR-E LSW showed an insignificant response; whereas the low variability in the L3 product at the tundra locations with open water did not allow such a comparison.

Particularly of note is a 15 August, 2002 extreme precipitation event that is registered as a rise in LSW, and modeled and observed soil moisture where available, at all of the tundra locations. This event is confirmed by Kane (2004) who observed 40-cm of wet snow falling in a 24-hour period that overwhelmed their rain gauges in the Upper Kuparuk drainage basin (~100 km from HPV). The recording of this event by both the AMSR-E LSW and NASA L3 algorithms at HPV and the apparent response of the LSW algorithm to this event at the other North Slope tundra location indicates that AMSR-E contains information of soil wetness in tundra locations, despite the lack of detection of significant correlation at several of the sites.

For some years at all locations the LSW algorithm indicates dry conditions relative to observed soil moisture early in the spring. The cause of this pattern is unknown, but one potential explanation is that a significant portion of the scene is frozen and thus appears ‘dry’ (low dielectric constant) to microwave observations. This pattern

was especially evident at the tundra locations with large open water fractions (BRW, UPAD, and ATQ), which suggests that it might be related to lake and sea ice that persists for a few days after the thaw of the surrounding landscape. Sea and lake ice emission was not considered to be distinct from land fraction emission in the LSW algorithm and as previously discussed sea ice was likely present at the coastal tundra locations for at least part of the summer.

E. Soil Moisture Frequency Distributions: The histograms presented in Figure 32 indicate that the sample frequency distribution of site soil moisture observations (< 8 cm) is relatively uniform at the locations where the satellite observations showed correspondence to observed soil moisture (HPV, OAS, and LTH). The models and AMSR-E retrievals, however, all show strongly aggregated distributions, consisting mostly of low values of soil moisture with spikes of extremely high soil moisture. This resulted in overall under prediction of soil moisture by the satellite methods and also by the API as can be seen in Figs. 30 and 31. The bias is somewhat removed by comparing the satellite products to the API instead of to soil moisture and this can partly explain the better accuracy occasionally obtained when the AMSR-E products were compared to API vs. soil moisture observations. The physical interpretation of this is that AMSR-E responds to the moisture content of the 'fast' surface soil layer which responds rapidly to wetting events, but dries quickly in the absence of wetting events. The use of time series smoothers in the two AMSR-E algorithms would also increase this type of correspondence.

F. The Challenge of Soil Moisture Validation: Validation of satellite soil moisture products against point soil moisture observations and precipitation-driven models is limited by several factors that are particularly severe in high-latitude regions. Actual soil moisture state integrated across a 60 km x 60 km satellite footprint can be much different than soil moisture measured at a single location within the footprint. Arctic and Boreal regions also have landscape features that can have vastly different soil moisture states in close proximity, for example, saturated lowland mires directly adjacent to dry upland heaths. Tussock tundra in particular is composed of relatively dry tussocks surrounded by near saturated inter-tussock areas.

High organic matter content soils with low bulk density and high porosity can cause soil moisture to be much different between near-surface organic layers and deeper mineral layers in tundra and Boreal landscapes (Kane 2004). The common Time Domain Reflectometry (TDR) technique for soil moisture used at all the study sites in this study is usually itself only accurate to ~ 0.03 m^3m^{-3} VMC (Boike & Roth 1997). TDR can also give erroneous readings in high-organic-matter, low-bulk-density soils when the probes are not in good contact with the soil matrix (Yoshikawa 2004).

It is well known that precipitation observations in high latitude regions under-represent actual precipitation by as much as a factor of three (Kane 2004). This will affect time-variability in model predictions of soil water state especially when the magnitude of extreme precipitation events is under-represented and small precipitation events are missed altogether. Furthermore, models may not be well suited to the hydrologic environment in which they are applied. The BIOME-BGC model employed

in this investigation only represents mineral soil, so the hydraulic properties of high-organic matter, low-bulk density soils are not well represented.

VII. Conclusion

The seasonal dynamics of multi-frequency AMSR-E T_b observations and their correlation with near-surface soil and air profile temperatures at high latitude sites were evaluated. The results demonstrate that brightness temperatures were strongly correlated (r >0.85) with minimum daily air temperatures at forested locations and better correlated with soil temperatures (r >0.80) than with minimum daily air temperatures at non-forested locations, with the highest correlation at frequencies >18.7 GHz. AMSR-E indicies, including T_{bh}, effective eh, 6.9 GHz polarization ratio, and 6.9 GHz to 36.5 GHz V and H-polarization spectral gradients, were sensitive to soil moisture variations (r ranged in magnitude from 0.23 to 0.56) and LAI seasonality (r ranged from 0.29 to 0.74) at locations with < 10 % open water and max annual LAI < 5 $m^2 m^{-2}$.

Methods were developed to retrieve soil temperature, maximum/minimum daily air temperatures, air temperature at time of overpass, daily maximum vapor pressure deficit, and a daily land surface wetness index from AMSR-E passive microwave observations. Land cover phenology including open water fraction and vegetation parameters were also retrieved as additional information. Visualization of Northern Hemisphere and pan-Arctic basin regional AMSR-E T_{bh} vs. T_{bv} histograms aided in formulating a method for retrieving open water and vegetation phenology from a single low-frequency AMSR-E channel. Interpretation of the T_{bh} vs. T_{bv} histograms also aided

in empirically fitting emission model parameters. Multiple regression, emission process-based radiative transfer models, and time series smoothers proved useful for separating the dependencies of factors influencing AMSR-E dual polarization, multi-frequency brightness temperature observations for retrieval of multiple land surface and meteorological state variables.

State variables retrieved from AMSR-E were evaluated for correspondence and accuracy against *in situ* observations, simple land-surface process model results, and other operational satellite products at eight Boreal and Arctic monitoring stations. For soil temperature, a multiple regression method had lower overall error (RMSE = 3.11 K) than a process-based method (RMSE = 3.93 K); however, the relative performance of the two methods was highly dependent on land cover type and condition between sites. Multiple regression methods were able to retrieve daily air temperatures including air temperature at time of overpass (T_{am}), minimum daily air temperature (T_{min}), and maximum daily air temperature (T_{max}) to accuracies of RMSE = 2.82°C, 2.88°C, and 3.31°C, respectively.

Daily maximum vapor pressure deficit (VPD) retrieved using AMSR-E daily AM/PM overpass surface temperature retrievals was accurate to within 427.9 Pa overall across locations. Substituting site meteorology reduced error to 307.4 Pa, indicating that 71.8% of the overall error was related to the underlying VPD algorithm assumptions with the remainder attributable to the AMSR-E air temperature retrievals. Open water fraction estimated from AMSR-E corresponded well with JERS-1 L-band radar open water fraction EASE grid cells (RMSE = 0.18), and MODIS land cover extractions of open water fraction (RMSE = 0.18), though the rigor of the comparisons was restricted by

differing spatial representations. Vegetation phenology represented by AMSR-E 6.9 GHz optical depth estimates corresponded well ($r = 0.52$ to $r = 0.80$) with MODIS 8-day LAI at sites with ≤ 11% open water. Relative linear trends among land cover classes of AMSR-E 6.9 GHz optical depth with MODIS LAI are similar to those obtained from Ku-band SeaWinds Scatterometer observations over North America (Frolking 2007).

Land surface wetness (LSW) and NASA L3 soil moisture retrievals contained significant information ($p < 0.001$) relative to site observations at three of the six locations for which soil moisture observations were available. Significant correspondence ranged from $r = 0.49$ to $r = 0.76$ at these locations for both methods. Correspondence degraded at locations with ≥ 25% open water and max annual LAI ≥ 4 m^2 m^{-2} despite efforts to correct for the influence of open water. Overall accuracy for the LSW algorithm compared against soil moisture observations and a simple API model ranged between ~ 0.068% to ~ 0.091% volumetric moisture content, which is comparable to results from similar studies for lower latitude locations. Accuracy of the NASA L3 algorithm was lower (~ 0.067% to ~ 0.12% volumetric) due to a dry bias. Histograms of AMSR-E satellite LSW and the NASA L3 algorithm indicate that these estimates potentially correspond more closely to the 'fast' response of the soil surface layer rather than the slow, average response of the 2-8 cm soil moisture observations. Point soil moisture observations and precipitation-driven models represent an imperfect means by which to validate coarse-resolution satellite estimates of soil wetness status.

The results of this investigation demonstrate that AMSR-E brightness temperatures contain a vast amount of useful information on land surface and meteorological state variables at high latitude locations. These variables can generally be

retrieved over natural landscapes though accuracies are dependent on land cover type, freeze-thaw status, snow, and potentially the atmosphere. Soil wetness estimates are generally possible over regions without much open water and without significant forest vegetation, although the precise range of influence of these factors is still uncertain. The algorithms employed are relatively simple, and require little ancillary data from other (and potentially error-prone) sources other than the AMSR-E radiometer itself. The products of this study are appropriate for biophysical modeling activities in Arctic and Boreal regions. The techniques and interpretations of high-latitude terrestrial brightness temperature signatures presented in this investigation will likely prove useful for future passive microwave missions.

REFERENCES

Aires, F., C. Prigent, W. B. Rossow, M. Rothstein. 2001. A new neural network approach including first guess for retrieval of atmospheric water vapor, cloud liquid water path, surface temperature, and emissivities over land from satellite microwave observations. *J. Geophys. Res.* 106 (D14): 14887-907.

Anderson, M.C., J.M. Norman, J.R. Mecikalski, J.A. Otkin, W.P. Kustas. 2007. A climatological study of evapotranspiration and moisture stress across the continental United States based on thermal remote sensing: 1. Model formulation. *J. Geophys. Res.* 112: D10117. doi:10.1029/2006JD007506.

Ashcroft, P., F. Wentz. 1999. Algorithm Theoretical Basis Document, AMSR level 2A algorithm," *RSS Tech. Report 121 599B-1.* Santa Rosa, CA.

Basist, A., N. C. Grody, T. C. Peterson, C. N. Williams. 1998. Using the Special Sensor Microwave/Imager to monitor land surface temperatures, wetness, and snow cover. *J. of Appl. Meteor.* 37: 888-911.

Bassist, A., C. Williams, N. Grody, T. F. Ross, S. Shen, A. T. C. Chang, R. Ferraro, M. J. Menne. 2001. Using the Special Sensor Microwave Imager to monitor surface wetness. *J. Hydromet.* 2: 297-308.

Boike, J., K. Roth. 1997. Time domain reflectometry as a field method for measuring water content and soil water electrical conductivity at a continuous permafrost site. *Permafrost and Periglacial Processes* 8: 359-70.

Bunn, A.G., S.J. Goetz, J.S. Kimball, K. Zhang. 2007. Northern high-latitude ecosystems respond to climate change. *EOS Trans.* 88(34).

Chan, S. K. 2007. Personal communication. Aug 15, Missoula, MT.

Christensen, J., M. Hulme, H. Von Storch, P. Whetton, R. Jones, L. Mearns, C. Fu. 2001. Chapter 10: Regional Climate Information Evalution and Projections. In *Climate Change 2001: The Scientific Basis*, J. T. Houghton, Y. Ding, D. J. Griggs, M. Noguer, P. J. van der Linden, X. Dai, K. Maskell, and C. A. Johnson, Eds., IPCC.

Comiso, J. C. 2002. Warming trends in the Arctic from clear sky satellite observations. *J. of Climate* 16 (21): 3498-510.

Comiso, J.C., D. J. Cavalieri, T. Markus. 2003. Sea ice concentration, ice temperature, and snow depth using AMSR-E Data. *IEEE Trans. Geosci. Rem. Sens.* 41(2): 243-52.

Crow, W.T., E.F. Wood. 2002. The value of coarse-scale soil moisture observations for regional surface energy balance modeling. *J. Hydromet.* 3(4): 467-482.

Crow, W. T., X. Zhan. 2007. Continental-scale evaluation of remotely sensed soil moisture products. *IEEE Geosci. Rem. Sens. Letters* 4(3): 451-52.

DeRidder, K. 2003. Surface soil moisture monitoring over Europe using Special Sensor Microwave/Imager (SSM/I) imagery. *J. Geophys. Res.* 108 (D14): doi: 10.1029/2002JD002796.

Dobson, M. C., F. T. Ulaby, M. T. Hallikainen, M. A. El-Rayes. 1985. Microwave dielectric behavior of wet soil-Part II: Dielectric mixing models. *IEEE Trans. Geosci. Rem. Sens.* GE-23: 35-46.

Dunn, A. L. 2006. Carbon fluxes and the Boreal forest mosaic. PhD. dissertation. Department of Earth & Planetary Sciences, Harvard University, Cambrige, MA.

Dunn, A. L., S. C. Wofsy. 2006. Boreal forest CO_2 flux, soil temperature, and meteorological data. Department of Earth & Planetary Sciences, Harvard University, Cambrige, MA.

Epstein, H. E., M. P. Calef, M. D. Walker, F. S. Chapin, A. M. Starfield. 2004. Detecting changes in Arctic tundra plant communities in response to warming over decadal time scales. *Global Change Biology* 10(8): 1325-34.

Entekhabi, D., E. G. Njoku, P. Houser, M. Spencer, T. Doiron, Y. Kim, J. Smith, R. Girard, S. Belair, W. Crow, T. J. Jackson, Y. H. Kerr, J. S. Kimball, R. Koster, K. C. McDonald, P. E. O' Neill, T. Pultz, S. W. Running, J. C. Shi, E. F. Wood, J. van Zyl. 2004. The Hydrosphere State (Hydros) Satellite Mission: An Earth System Pathfinder for Global Mapping of Soil Moisture and Land Freeze/Thaw. *IEEE Trans. Geosci. Rem. Sens.* 42(10): 2184-95.

Escorihuela, M. J., Y. H. Kerr, P. de Rosnay, J. P. Wigneron, J. C. Calvet, F. Lemaitre. 2007. A simple model of bare soil microwave emission at L-band. *IEEE Trans. Geosci. Rem. Sens.* 45(7): 1978-87.

Eugster, W., W.R. Rouse, R.A. Pielke, J.P. McFadden, D.D. Baladocchi, T.G. Kittel, F.S. Chapin, G.E. Liston, P.L. Vidale, E. Vaganov, S. Chambers. 2000. Land-atmosphere energy exchange in Arctic tundra and Boreal forest: Available data and feedbacks to climate. *Global Change Biology* 6: 84-115.

Euskirchen, E.S., A.D. McGuire, D.W. Kicklighter, Q. Zhuang, J.S. Clein, R.J. Dargaville, D.G. Dye, J.S. Kimball, K.C. McDonald, J.M. Melillo, V.E. Romanovsky, N.V. Smith. 2006. Importance of recent shirts in soil thermal dynamics on growing season length, productivity, and carbon sequestration in terrestrial high-latitude ecosystems. *Global Change Biology* 12: 731-50.

Fily, M., A. Royer, K. Goita, C. Prigent. 2003. A simple retrieval method for land surface temperature and fraction of water surface determination from satellite

microwave brightness temperatures in sub-Arctic areas. *Rem. Sens. Environ.* 83: 328-38.

Flanagan, L. B., B. G. Johnson. 2005. Interacting effects of temperature, soil moisture and plant biomass production on ecosystem respiration in a northern temperate grassland. *Agri. & For. Meteor.* 130(3-4):237-53.

Friedl, M.A., D. K. McIver, J. C. F. Hodges, X. Y. Zhang, D. Muchoney, A. H., Strahler, C. E. Woodcok, S. Gopal, A. Schneider, A. Cooper, A. Baccini, F. Gao, C. Schaaf. 2002. Global land cover mapping from MODIS: algorithms and early results. *Rem. Sens. Environ* 83(1-2): 287-302.

Frolking, S., T. Milliman, K. McDonald, J. Kimball, M. Zhao, M. Fahnestock. 2006. Evaluation of the Sea Winds Scatterometer for regional monitoring of vegetation phenology. *J. Geophys. Res.* 111(D17302): doi: 10.1029/2005JD006588.

Gates, W. L., J. F. B. Mitchell, G. J. Boer, U. Cubasch, and V.P. Meleshko. 1992. Climate modeling, climate prediction and model validation. In *Climate change 1992: the supplemental report to the IPCC scientific assessment*, J.T. Houghton, B.A. Callander, & S.K. Varney, Eds. Cambridge University Press, Cambridge, UK: 97-135.

Gillespie, A., S. Rokugawa, T. Matsunaga, J.S. Cothern, S. Hook, A.B. Kahle. 1998. A temperature and emissivity separation algorithm for Advanced Spaceborne Thermal Emission and Reflection Radiometer (ASTER) Images. *IEEE Trans. Geosci. Rem. Sens.* 36 (4): 1113-26.

Gillies, R. R., Carlson, T. N., Gui, J., Kustas, W. P., & Humes, K. S. 1997. A verification of the 'triangle' method for obtaining surface soil water content and energy fluxes from remote measurements of the Normalized Difference Vegetation Index (NDVI) and surface radiant temperature. *Int. J. Rem. Sens.* 18 (15): 3145–66.

Goita, K., A. Royer, N. Bussieres. 1997. Characterization of land surface thermal structure from NOAA- AVHRR data over a northern ecosystem. *Rem. Sens. Environ.* 60: 282-98.

Griffis, J., T. A. Black, D. Gaumont-Guay, G. B. Drewitt, Z. Nesic, A. G. Barr, K. Morgenstem, and N. Kljun. 2004. Seasonal variation and partitioning of ecosystem respiration in a southern Boreal aspen forest. *Agri. & For. Meteor.* 125(3-4): 207-23.

Grody, N.C., A. N. Bassist. 1997. Interpretation of SSM/I Measurements over Greenland. *IEEE Trans. Geosci. Rem. Sens.* 35: 360-6.

Heinsch, F. A., M. Zhao, S. W. Running, J. S. Kimball, R. R. Nemani, K. J. Davis, P. V. Bolstad, B. D. Cook, A. R. Desai, D. M. Ricciuto, B. E. Law, W. C. Oechel, H.

Kwon, H. Luo, S. C. Wofsy, A. L. Dunn, J. W. Munger, D. D. Baldocchi, L. Xu., D. Y. Hollinger, A. D. Richardson, P. C. Stoy, M. B. S. Siqueira, R. K. Monson, S. P. Burns, L. B. Flanagan. 2006. Evaluation of remote sensing based terrestrial production from MODIS using AmeriFlux eddy tower flux network observations. *IEEE Trans. Geosci. Rem. Sens.* 44 (7): 1908-25.

Hiltbrunner, D., C. Matzler, A. Wiesmann. 1994. Monitoring land surfaces with combined DMSP-SSM/I and ERS-1 scatterometer data. *Proc. IGARSS '94 Symp* , Pasadena, CA:1945-7.

Hinkel, K. M., F. E. Nelson. 2003. Spatial and temporal patterns of active layer thickness at Circumpolar Active Layer Monitoring (CALM) sites in northern Alaska, 1995-2000. *J. Geophys. Res.* 108 (D2): 8168-81.

Hinzman, L. D., D. L. Kane. 1992. Potential response of an Arctic watershed during a period of global warming. *J. Geophys. Res.* 97: 2811-20.

Hinzman, L. D., 2004. Evidence and implications of recent climate change in northern Alaska and other Arctic regions. *Climatic Change* 72: 251-98.

Jackson, T. J., T. J. Schmugge. 1991. Vegetation effects on the microwave emission from soils. *Rem. Sens. Environ.* 36: 203-12.

Jackson, T. J., D. M. LeVine, A. Y. Hsu, A. Oldak, P. J. Starks, C. T. Swift, J. D. Isham, M. Haken. 1999. Soi moisture mapping at regional scales using microwave radiometry: The Southern Great Plains Hydrology Experiment. *IEEE Trans. Geosci. Rem. Sens.* 37(5): 2136-50.

Jones, L. A., J. S. Kimball, K. C. McDonald, S. K. Chan, E. G. Njoku, W. C. Oechel. 2007. Satellite microwave remote sensing of Boreal and Arctic soil temperatures from AMSR-E. *IEEE Trans. Geosci. Rem. Sens.* 45(7): 2004-18.

Kane, D.L. and Hinzman, L.D. 2006. Climate data from the North Slope Hydrology Research project. University of Alaska Fairbanks, Water and Environmental Research Center. Fairbanks, AK. [Online]. Available: http://www.uaf.edu/water/projects/NorthSlope/

Kelly, R.E., A. T. Chang, L. Tsang. J. L. Foster. 2003. A prototype AMSR-E global snow area and snow depth algorithm. *IEEE Trans. Geosci. Rem. Sens.* 41(2): 230-42.

Kerr, Y. H., P. Waldteufel, J. P. Wigneron, J. M. Martinuzzi, J. Font, M. Berger. 2001. Soil moisture retrieval from Space: The Soil Moisture and Ocean Salinity (SMOS) Mission. *IEEE Trans. Geosci. Rem. Sens.* 39(8): 1729-35.

Kane, D. L., R. E. Gieck, D. C. Kitover, L. D. Hinzman, J. P. McNamara, D. Yang. 2004. Hydrological cycle on the North Slope of Alaska. In: D. L. Kane, D. Yang (Eds.) *Northern research basins water balance*. Oxfordshire, UK: IAHS Publication 290: 224-36.

Kim, E. J., A. W. England. 2001. Diurnal and seasonal cold land signatures in SSM/I-scale microwave radiometery of the North Slope of Alaska. *IEEE Int. Geosci. Rem. Sens. Symp. (IGARSS '98)* 5: 2127-29.

Kim, E. J., A. W. England. 2003. A yearlong comparison of plot-scale and satellite footprint-scale 19 and 37 GHz brightness of the Alaskan North Slope. *J. Geophys. Res.*, 108 (D13): 4388-404.

Kim, E. J. 2007. Personal communication. Aug 16, Missoula, MT.

Kimball, J. S., S.W. Running, R. Nemani. 1997a. An improved method for estimating surface humidity from daily minimum temperature. *Ag. For. Meteorol.* 85: 87-98.

Kimball, J. S., M. A. White, S. W. Running. 1997b. BIOME-BGC simulations of stand hydrologic processes for BOREAS. *J. Geophys. Res.* 102(D24): 29043-51.

Kimball, J. S., K. C. McDonald, A. R. Keyser, S. Frolking, S. W. Running. 2001. Application of the NASA scatterometer (NSCAT) for classifying the daily frozen and non-frozen landscape of Alaska. *Rem. Sens. Environ.* 75: 113-26.

Kimball, J. S., K. C. McDonald, S. Frolking, S. W. Running. 2004a. Radar remotes sensing of the spring thaw transition across a Boreal landscape. *Rem. Sens. Environ.* 89:163-75.

Kimball, J. S., K. C. McDonald, S. W. Running, S. Frolking. 2004b. Satellite radar remote sensing of seasonal growing seasons for Boreal and sub-alpine evergreen forests. *Rem. Sens. Environ.* 90:243-58.

Kwon, H. J., W. C. Oechel, R. C. Zulueta, S. J. Hastings. 2006. Effects of climate variability on carbon sequestration among adjacent wet sedge tundra and moist tussock tundra ecosystems. *J. Geophys. Res.* 111(G03014): doi: 10.1029/2005JG000036.

Li, Q., L. Tsang, J. C. Shi, C. H. Chan. 2000. Application of physics-based two-grid method and sparse matrix canonical grid method for numerical simulations of emissivities of soils with rough surfaces at microwave frequencies. *IEEE Trans. Geosci. Rem. Sens.* 38: 1635-43.

Matzler, C. 1994. Passive microwave signatures of landscapes in winter. *Meteorol. Atmos. Phys.* 54: 241-60.

Matzler, C., P. W. Rosenkranz. 2006. Dependence of microwave brightness temperature on bistatic surface scattering: Model functions and applications to AMSU-A. *IEEE Trans. Geosci. Rem. Sens.* 45(7): 2130-38.

McDonald, K. C., J. S. Kimball., E. G. Njoku, R. Zimmerman, M. Zhao. 2004. Variability in springtime thaw in the terrestrial high latitudes: Monitoring a major control on the biospheric assimilation of atmospheric carbon dioxide with spaceborne microwave remote sensing. *Earth Interactions* 8(20):1-23.

McDonald, K. C., J. S. Kimball. 2005. Chapter 53: Freeze-thaw states using both active and passive microwave sensors. In *Encyclopedia of Hydrological sciences*, M. G. Anderson, (Ed.); John Wiley and Sons, Hoboken, N.J.

McFarland, M. J., R. L. Miller, C. M. Neale. 1990. Land surface temperature derived from the SSM/I passive microwave brightness temperatures. *IEEE Trans. Geosci. Rem. Sens.* 28(5): 839-45.

Nemani, R., L. Pierce, S.W. Running, S. Goward. 1993. Developing satellite-derived estimates of surface moisture status. *J. Appl. Meteor.* 32: 548-56.

Njoku, E. G. 1995. Surface temperature estimation over land using satellite microwave radiometry. In *Passive microwave remote sensing of land-atmosphere interactions*, B.J. Choudbury, Y. H. Kerr, E. G. Njoku, and P. Pampaloni (Eds.), Utrecht, The Netherlands: VSP; 509-30.

Njoku, E. G. 1999. AMSR land surface parameters," *ATBD 3.0.* Jet Propulsion Laboratory, Pasadena, CA. [Online]. Available: http://eospso.gsfc.nasa.gov/ftp_ATBD/REVIEW/AMSR/atbd-amsr-land.pdf

Njoku, E. G., L. Li. 1999. Retrieval of land surface parameters using passive microwave measurements at 6-18 GHz. *IEEE Trans. Geosci. Rem. Sens.* 37(1): 79-93.

Njoku, E. G., T. J. Jackson, V. Lakshmi, T. K. Chan., S. V. Nghiem. 2003. Soil moisture retrieval from AMSR-E. *IEEE Trans. Geosci. Rem. Sens.* 41(2): 215-29.

Njoku, E. G. 2007. AMSR-E/Aqua Daily L3 Surface Soil Moisture, V001, *National Snow and Ice Data Center*, Boulder, CO, USA. Digital Media. Updated daily.

Njoku, E. G., P. Ashcroft, T. K. Chan, L. Li. 2005. Global survey and statistics of radio-frequency interference in AMSR-E land observations. *IEEE Trans. Geosci. Rem. Sens.* 43(5): 938-47.

Njoku, E. G., S. K. Chan. 2006. Vegetation and surface roughness effects on AMSR-E land observations. *Rem. Sens. Environ.* 100: 190-99.

Oechel, W.C., S. J. Hastings, G. L. Vourlitis, M. Jenkins, G. Riechers, N. Grulke. 1993. Recent change of Arctic tundra ecosystems from a net carbon dioxide sink to a source. *Nature* 361: 520-3.

Oechel, W.C., G.L. Vourlitis, S.J. Hastings, S.A. Bockarev. 1995. Change in Arctic CO_2 flux over two decades: Effects of climate change at Barrow, Alaska. *Ecol. Appl.* 5(3): 846-55.

Oechel, W.C., G.L. Vourlitis, S.J. Hastings, R.P. Ault, P. Bryant. 1998. The effects of water table manipulation and elevated temperature on the net CO_2 flux of wet sedge tundra ecosystems. *Global Change Biology* 4(1): 77-90.

Oechel, W. C., G. L. Vourlitis, S. J. Hastings, R. C. Zulueta, L. Hinzman, D. Kane. 2000. Acclimation of ecosystem CO_2 exchange in the Alaskan Arctic in response to decadal climate warming. *Nature* 406: 978-81.

Osterkamp, T. E., V. E. Romanovsky. 1999. Evidence for warming and thawing of discontinuous permafrost in Alaska. *Permafrost and Periglacial Processes* 10: 17-37.

Owe, M., R. de Jeu, J. Walker. 2001. A methodology for surface soil moisture and vegetation optical depth retrieval using the microwave polarization difference index. *IEEE Trans. Geosci. Rem. Sens.* 39(8): 1643-54.

Paetzold, R. F., F. E. Nelson, K. M. Hinkel. 2006. Meteorologic and soil data from Alaska North Slope Sites.

Paloscia, S., P. Pampaloni. 1988. Microwave polarization index for monitoring vegetation growth. *IEEE Trans. Geosci. Rem. Sens.* 26: 617-621.

Pellarin, T., Y. H. Kerr, J. P. Wigneron. 2006. Global simulation of brightness temperatures at 6.6 and 10.7 GHz over land based on SMMR data set analysis. *IEEE Trans. Geosci. Rem. Sens.* 44(9): 2492-05.

Prigent, C., W. B. Rossow, E. Matthews. 1997. Microwave land surface emissivities estimated from SSM/I observations. *J. Geophys. Res.* 102(D18): 21867-90.

Prigent, C., F. Aires, W. B. Rossow, A. Robock. 2005. Sensitivity of satellite microwave and infrared observations to soil moisture at a global scale: Relationship of satellite observations to *in situ* soil moisture measurements. *J. Geophys. Res.* 110(D07110): doi:10.1029/2004JD005087.

Pulliainen, J. T., J. Grandell, M. T. Hallikainen. 1997. Retrieval of Surface Temperature in Boreal Forest Zone from SSM/I data. *IEEE Trans. Geosci. Rem. Sens.* 35(5): 1188-1200.

Sandholt, I., K. Rasmussen, J. Andersen. 2002. A simple interpretation of the surface temperature/vegetation index space for assessment of surface moisture status. *Rem. Sens. Environ.* 79: 213-24.

Ellingson, S. W., J.T. Johnson. 2006. A polarimetric survey of radio-frequency interference in C- and X-bands in the continental United States using WindSat radiometry. *IEEE Trans. Geosci. Rem. Sens.* 44(3): 540-48.

Running, S. W., R. E. Hunt. 1993. Generalization of a forest ecosystem process model for other biomes, BIOME-BGC, and an application for global-scale models. In: J. R. Ehlinger, C. B. Fields, Scaling Physiologic Processes: Leaf to Globe. San Diego, CA: Academic Press: 141-58.

Running, S. W., R. H. Waring. 1998. Forest ecosystems: Analysis at multiple scales. 2nd edition. San Diego, CA: Academic Press.

Serreze, M. C., J. E. Walsh, F. S. Chapin, T. Osterkamp, M. Dyurgerov, V. Romanovsky, W. C. Oechel, J. Morison, T. Zhang, and R. G. Barry. 2000. Observational evidence of recent change in the northern high-latitude environment. *Climatic Change* 46 (1-2): 159-207.

Shi, J. C., K. S. Chen, Q. Li, T. J. Jackson, P. E. O'Neill, L. Tsang. 2002. A parameterized surface reflectivity model and estimation of bare-surface soil moisture with L-band radiometer. *IEEE Trans. Geosci. Rem. Sens.* 40(12): 2674-86.

Shi, J. C., L. Jiang, L. Zhang, K. S. Chen, J. P. Wigneron, A. Chanzy, T. J. Jackson. 2006. Physically based estimation of bare-surface soil moisture with passive radiometers. *IEEE Trans. Geosci. Rem. Sens.* 44(11): 3145-53.

Stieglitz, M., J. Hobbie, A. Giblin, G. Kling. 1999. Hydrologic modeling of an Arctic tundra watershed: Toward Pan-Arctic predictions. *J. Geophys. Res.* 104 (D22): 27507:18.

Sturm, M., Racine, C., K. Tape. 2001. Increasing shrub abundance in the Arctic. *Nature* 411: 546-7.

Ulaby, F. T., R. K. Moore, A. K. Fung. 1986. *Microwave Remote Sensing: Active and Passive.* Vol. 1-3, Dedham, MA, USA: Artech House.

Van de Griend, A. A., M. Owe. 1994. The influence of polarization on canopy transmission properties at 6.6 GHz and implications for large scale soil moisture monitoring in semi-arid environments. *IEEE Trans. Geosci. Rem. Sens.* 32(2): 206-16.

Van de Griend, A. A., J. P. Wigneron. 2004. The b-factor as a function of frequency and canopy type at H-polarization. *IEEE Trans. Geosci. Rem. Sens.* 42(4): 786-94.

Verstraeten, W.W., F. Veroustraete, C.J. van der Sande, I. Grootaers, J. Feyen. 2006. Soil moisture retrieval using thermal inertia, determined with visible and thermal spaceborne data, validated for European forests. *Rem. Sens. Environ.* 101: 299-314.

Wagner, W., G. Lemione, H. Rott. 1999a. A method for estimating soil moisture from ERS Scatterometer and soil data. *Rem. Sens. Environ.* 70: 191-207.

Wagner, W., J. Noll, M. Borgeaud, H. Rott. 1999b. Monitoring soil moisture over the Canadian Prairies with the ERS Scatterometer. *IEEE Trans. Geosci. Rem. Sens.* 37(1): 206-16.

Wagner, W., V. Naeimi, K. Scipal, R. de Jeu, J. Martinez-Fernandez. 2006. Soil moisture from operational meteorological satellites. *Hydrogeology Journal* doi:10.1007/s10040-006-0104-6.

Wan, Z. 1999. MODIS Land Surface Temperature Algorithm Theoretical Basis Document. *ATBD 3.3.* University of California, Santa Barbara, CA. [Online]. Available: http://modis.gsfc.nasa.gov/data/atbd/land_atbd.php

Wan, Z., Y. Zhang, Q. Zhang, Z. Li. 2002. Validation of the land-surface temperature products retrieved from Terra Moderate Resolution Imaging Spectroradiometer data. *Rem. Sens. Environ.* 83 (1): 163-80.

Wang, J. R., B. J. Choudhury. 1995. Passive microwave radiation from soil: Examples of emission models and observations. In: B. J. Choudhury, Y. Kerr, E. G. Njoku, and P. Pampaloni (Eds.), *Passive microwave remote sensing of land-atmosphere interactions*. Utrecht, The Netherlands: VSP.

Wen, J., Z. Su. 2004. An analytical algorithm for the determination of vegetation Leaf Area Index from TRMM/TMI data. *Int. J. Rem. Sens.* 25(6): 1223-34.

Western, A. W., G. Bloschl. 1999. On the spatial scaling of soil moisture. *J. Hydro.* 217: 203-24.

Yoshikawa, K., P. P. Overduin, J. Harden. 2004. Moisture content measurements of moss (*Sphagnum* spp.) using commercial sensors. *Permafrost and Periglacial Processes* 15: 309-18.

Zhang, K., J.S. Kimball, M. Zhao, W. C. Oechel, J. Casano, S.W. Running. 2007. Sensitivity of pan-Arctic terrestrial net primary productivity simulations to daily surface meteorology from NCEP-NCAR and ERA-40 re-analyses. *J. Geophys. Res.* 112: doi:10.1029/2006JG000249.

TABLES

Table 1: Biophysical network sites used for this investigation. NSA NOBS refers to the Northern Study Area Old Black Spruce; SSA OAS refers to the Southern Study Area Old Aspen tower sites located within the Boreal Ecosystem-Atmosphere Study (BOREAS) region of central Canada; these sites are currently associated with the Boreal Ecosystem Monitoring and Research Sites (BERMS) project.

Site	Abbrev.	Lat. Long.	Vegetation	Topog.
Barrow	BRW	71.32 N 156.62 W	Wet-sedge Tundra	flat
UPad/Betty Pingo	UPAD	70.28 N 148.88 W	Wet-sedge Tundra	flat
Atqasuk	ATQ	70.47 N 157.40 W	Wet-sedge/Tussock Tundra	flat
Ivotuk	IVO	68.47 N 155.73 W	Tussock Tundra	foothills
Happy Valley/Sagwon	HPV	69.13 N 148.83 W	Tussock Tundra	foothills
NSA NOBS	NOBS	55.88 N 98.48 W	Boreal spruce forest	flat
SSA OAS	OAS	53.63 N 106.20 W	Boreal mixed forest/Crops	flat
Lethbridge	LTH	49.70 N 112.93 W	Grassland/Crops	flat

Table 2: AMSR-E sensor instrument specifications.

Center Frequency (GHz)	6.9	10.7	18.7	23.8	36.5	89.0
Bandwidth (MHz)	350	100	200	400	1000	3000
3-dB Footprint (km)	75 x 43	51x 29	27 x 16	32 x 18	14 x 8	6 x 4
Resolution (km x km)	60	60	25	25	15	5

Table 3: Coefficients (standard errors) fit to the multi-band, multiple regression equation for soil temperature retrieval in (10).

All Sites	β_0	β_1	β_2	β_3	β_4	β_5
Thawed	74.792	0.915	-0.640	-0.927	1.42	230.553
	(4.743)	(0.122)	(0.208)	(0.189)	(0.093)	(9.217)
Frozen	246.905	0.913	-0.084	-2.618	1.892	-35.016
	(5.422)	(-0.159)	(0.240)	(0.187)	(0.093)	(8.338)

Table 4: Coefficients (standard errors) fit to the multi-band, multiple regression equation for maximum daily air temperature (T_{max}), minimum daily air temperature (T_{min}), and air temperature at time of Aqua satellite descending (morning) overpass retrieval.

	β_0	β_1	β_2	β_3	β_4	β_5
Tmax	13.889	-0.807	0.168	1.617	-75.384	342.025
	(-3.091)	(0.052)	(0.053)	(0.030)	(8.020)	(12.107)
Tmin	40.826	-0.384	-0.091	1.346	-80.348	338.752
	(3.946)	(0.049)	(0.049)	(0.026)	(6.600)	(10.782)
Tam	16.595	-0.959	0.342	1.586	-99.169	357.934
	(3.944)	(0.049)	(0.049)	(0.026)	(6.555)	(10.530)

Table 5: Constant Parameters calibrated to the BRW site for the process-based method. The α values were obtained using a frequency power relation (Njoku and Chan 2006). The values for *a* and *b* are also given for frozen conditions (a_{sn} and b_{sn}).

Model Parameters					
Band (GHz)	***a***	***b***	a_{sn}	b_{sn}	***α***
6.9	0.631	0.402	0.592	0.450	0.486
10.7	0.607	0.416	0.574	0.468	0.566
18.7	0.601	0.418	0.578	0.466	0.688
23.8	0.557	0.453	0.523	0.508	0.749
36.5	0.554	0.455	0.526	0.506	0.87
89	0.518	0.481	0.508	0.515	1.188

Table 6: Correlation between site soil moisture observations and MODIS 8-day Leaf Area Index (LAI) to AMSR-E observations, including 6.9 GHz H-pol. brightness temperature observations (T_{bh}), 6.9 GHz H-pol. effective emissivity (e_h), and indices computed from V and H pol. brightness temperatures at 6.9 GHz and 36.5 GHz. Bold font denotes that the correlation is significant ($p < 0.05$) and of expected sign for microwave radiometry.

Site Soil Moisture Correlations									
Index	**BRW**	**UPAD**	**ATQ**	**IVO**	**HPV**	**NOBS**	**OAS**	**LTH**	**Expected Sign (+/-)**
Tbh	**-0.21**	0.47	NA	NA	**-0.51**	0.05	**-0.42**	**-0.56**	-
eh	**-0.21**	0.53	NA	NA	**-0.50**	0.15	**-0.28**	**-0.46**	-
Tbv/Tbh	**0.26**	-0.44	NA	NA	**0.42**	0.07	**0.33**	**0.47**	+
Tbh36/Tbh6	**0.29**	-0.44	NA	NA	-0.11	**0.15**	**0.23**	**0.39**	+
Tbv36/Tbh6	**0.28**	-0.49	NA	NA	0.12	**0.13**	**0.32**	**0.47**	+
MODIS Leaf Area Index (LAI) Correlations									
Index	**BRW**	**UPAD**	**ATQ**	**IVO**	**HPV**	**NOBS**	**OAS**	**LTH**	**Expected Sign (+/-)**
Tbh	-0.28	-0.29	-0.19	**0.49**	0.32	**0.43**	**0.74**	**0.60**	+
eh	-0.28	-0.35	-0.63	-0.79	-0.21	-0.53	0.03	**0.37**	+
Tbv/Tbh	0.29	0.28	0.41	-0.13	-0.32	0.18	**-0.50**	**-0.55**	-
Tbh36/Tbh6	0.27	0.19	0.18	0.40	-0.03	0.46	-0.14	**-0.33**	-
Tbv36/Tbh6	0.29	0.26	0.36	0.32	-0.14	0.42	**-0.29**	**-0.46**	-

Table 7: Thawed condition validation statistics by site for AMSR-E surface temperature methods. The numbers represent comparison of retrieved T_s vs. T_{soil} (T_{min}). R^2 = coefficient of determination, RMSE = root mean square error, MAE = mean absolute error, MR = mean residual (observed – retrieved), *n* = sample size.

	Process-Based Method				Regression Method				
SITE	**RMSE**	**R^2**	**MAE**	**MR**	**RMSE**	**R^2**	**MAE**	**MR**	***n***
BRW	2.96 (3.91)	0.45 (0.23)	2.40 (3.27)	1.12 (-1.59)	2.57 (3.47)	0.59 (0.45)	2.14 (2.85)	0.86 (-1.88)	105 (120)
ATQ	2.22 (3.74)	0.69 (0.41)	1.83 (2.90)	-1.19 (-2.53)	2.16 (3.55)	0.69 (0.44)	1.75 (2.84)	-0.94 (-2.31)	99 (100)
IVO	2.94 (4.06)	0.61 (0.19)	2.43 (3.43)	-1.70 (-1.10)	4.032 (4.58)	0.75 (0.22)	3.85 (3.92)	-3.71 (-3.40)	56 (102)
HPV	3.15 (3.84)	0.77 (0.36)	2.69 (3.09)	-2.39 (-1.93)	4.99 (4.69)	0.76 (0.46)	4.54 (4.11)	-4.43 (-3.97)	90 (90)
NOBS	3.72 (5.74)	0.32 (0.30)	2.91 (4.60)	-0.59 (-3.77)	3.00 (5.47)	0.37 (0.30)	2.43 (4.05)	-0.35 (-3.53)	132 (132)
OAS	3.99 (4.81)	0.60 (0.44)	3.22 (3.85)	2.57 (-1.68)	2.71 (5.18)	0.62 (0.44)	2.16 (4.32)	1.05 (-3.20)	186 (186)
LTH	5.55 (5.12)	0.68 (0.44)	4.86 (4.16)	4.72 (-2.61)	2.84 (8.30)	0.65 (0.41)	2.32 (7.32)	0.30 (-7.03)	187 (187)

Table 8: Frozen condition validation statistics by site for AMSR-E surface temperature methods. The numbers represent comparison of retrieved T_s vs. T_{soil} (T_{min}). R^2 = coefficient of determination, RMSE = root mean square error, MAE = mean absolute error, MR = mean residual (observed – retrieved), *n* = sample size.

	Process-Based Method				Regression Method				
SITE	**RMSE**	**R^2**	**MAE**	**MR**	**RMSE**	**R^2**	**MAE**	**MR**	***n***
BRW	7.00 (12.52)	0.24 (0.25)	5.32 (11.05)	-0.91 (-.891)	8.67 (16.31)	0.35 (0.42)	7.86 (14.11)	-6.17 (-13.78)	222 (241)
ATQ	7.85 (13.25)	0.51 (0.21	5.65 (11.32)	-1.24 (-7.24)	4.95 (7.80)	0.70 (0.63)	4.05 (6.40)	2.54 (-3.80)	247 (262)
IVO	10.51 (10.48)	0.49 (0.42)	9.24 (7.67)	5.77 (-5.92)	6.18 (7.54)	0.64 (0.71)	5.23 (6.10)	5.11 (-4.66)	205 (252)
HPV	9.23 (11.05)	0.48 (0.54)	6.83 (9.02)	-2.71 (-8.17)	5.53 (7.06)	0.50 (0.66)	4.32 (5.86)	-3.36 (-4.68)	228 (222)
NOBS	19.48 (7.96)	0.48 (0.68)	16.29 (6.21)	15.44 (-3.07)	3.11 (20.35)	0.14 (0.04)	2.60 (16.88)	2.32 (-16.34)	196 (202)
OAS	7.42 (13.38)	0.22 (0.30)	5.96 (11.36)	4.47 (-0.87)	3.06 (16.78)	0.03 (0.06)	2.51 (14.45)	1.83 (-13.45)	145 (145)
LTH	4.76 (12.83)	0.00 (0.02)	3.57 (9.70)	-1.61 (-8.78)	3.37 (10.56)	0.36 (0.13)	2.96 (7.74)	2.01 (-5.16)	124 (124)

Table 9: Validation statistics for thawed-season AMSR-E 2004 air temperature (T in **°C**; ~2 m height) retrievals by study location. T_{am} stands for air temperature at time of descending (am) overpass; T_{min} is minimum daily air temperature; T_{max} is maximum daily air temperature. Statistical abbreviations as in Table 7.

	Tair [°C]	RMSE	R^2	MAE	MR	Slope	*n*
BRW	T_{am}	3.77	0.55	3.05	1.14	1.01	113
	T_{min}	3.25	0.45	2.62	0.42	0.88	113
	T_{max}	3.79	0.52	3.12	-1.24	0.65	113
UPAD	T_{am}	3.59	0.68	2.94	2.19	0.96	91
	T_{min}	3.71	0.57	3.19	2.41	0.82	91
	T_{max}	4.06	0.68	3.28	1.65	0.70	92
ATQ	T_{am}	1.86	0.84	1.44	-0.13	0.94	99
	T_{min}	1.91	0.84	1.50	0.87	0.83	100
	T_{max}	2.40	0.85	1.95	0.70	0.81	101
IVO	T_{am}	1.95	0.81	1.44	0.03	0.82	61
	T_{min}	2.10	0.87	1.82	1.33	0.83	67
	T_{max}	3.17	0.82	2.57	1.35	0.92	66
HPV	T_{am}	3.54	0.77	2.93	0.66	0.75	130
	T_{min}	3.77	0.74	3.04	1.42	0.67	130
	T_{max}	3.92	0.83	3.00	-1.05	0.84	133
NOBS	T_{am}	3.06	0.73	2.41	0.45	0.74	128
	T_{min}	2.38	0.83	1.79	-1.38	0.82	129
	T_{max}	2.79	0.82	1.85	0.22	0.80	130
OAS	T_{am}	1.93	0.90	1.53	0.31	0.87	187
	T_{min}	2.57	0.84	2.11	0.68	0.73	187
	T_{max}	2.48	0.91	1.92	0.02	0.78	177
LTH	T_{am}	2.46	0.82	1.96	-0.43	0.77	187
	T_{min}	2.74	0.79	2.18	-0.51	0.66	187
	T_{max}	3.61	0.75	2.75	-0.76	0.88	189

Table 10: Validation statistics for thawed-season AMSR-E 2004 Vapor Pressure Deficit (VPD) in pascals (Pa) by algorithm input meteorology and by study site. The VPD algorithm run with T_{min} and T_{max} from AMSR-E is denoted 'VPD AMSRE' and the VPD algorithm run with T_{min} and T_{max} from site observations is denoted 'VPD site met.' Statistical abbreviations as in Table 7.

	VPD [Pa]	RMSE	R^2	MAE	MR	Slope	n
BRW	VPD site met	191.78	0.68	137.72	-93.22	1.33	113
	VPD AMSRE	330.17	0.03	255.23	-178.78	0.25	113
UPAD	VPD site met	102.70	0.79	100.23	11.29	1.29	16
	VPD AMSRE	127.22	0.25	111.79	-19.12	0.37	16
ATQ	VPD site met	250.62	0.79	198.47	-147.09	0.91	100
	VPD AMSRE	284.13	0.63	226.61	-113.84	0.66	99
IVO	VPD site met	201.29	0.86	162.25	-42.96	0.90	68
	VPD AMSRE	321.06	0.69	271.81	4.15	0.87	67
HPV	VPD site met	295.46	0.79	230.23	-77.95	0.75	134
	VPD AMSRE	489.85	0.61	379.64	-256.81	0.80	129
NOBS	VPD site met	441.54	0.80	357.13	246.41	0.87	119
	VPD AMSRE	549.73	0.79	448.90	407.60	0.73	100
OAS	VPD site met	388.05	0.72	257.56	137.35	0.67	198
	VPD AMSRE	436.04	0.60	303.66	121.06	0.61	167
LTH	VPD site met	246.68	0.94	193.43	122.80	0.87	220
	VPD AMSRE	470.57	0.71	369.68	48.79	0.79	159

Table 11: Results for comparison of retrieved AMSR-E 6.9 GHz optical depth to MODIS 8-day LAI by study site. The statistics presented here correspond to regression lines presented in Fig 27.

Site	MODIS LAI Range [m^2 m^{-2}]	AMSR-E 6.9 GHz Optical Depth	*r*	*p*-value	Slope	Int.	*n*
BRW	0.5 - 1.5	0.51 - 1.23	-0.46	0.005	-0.39	1.20	36
UPAD	0.6 - 1.6	0.79 - 1.36	-0.15	0.425	-0.08	1.11	32
ATQ	0.6 - 1.6	0.67 - 1.19	-0.34	0.045	-0.15	1.08	36
IVO	1.0 - 2.0	0.85 - 1.37	0.52	0.001	0.21	0.94	36
HPV	1.2 - 2.6	1.06 - 1.45	0.54	0.001	0.14	1.05	36
NOBS	1.9 - 4.7	1.30 - 1.87	0.75	<0.0001	0.13	1.25	45
OAS	0.8 - 3.8	0.98 - 1.41	0.79	<0.0001	0.07	1.07	56
LTH	0.4 - 2.0	0.68 - 1.16	0.80	<0.0001	0.19	0.74	64

Table 12a: Pairwise soil moisture validation statistics for the period June 2002-December 2004 for BRW and UPAD sites. The data compared include *in situ* soil moisture (< 8 cm) observations (SM Obs), Antecedent Precipitation Index (API) model, BIOME-BGC soil moisture model, the AMSR-E NASA L3 algorithm soil moisture (L3), and AMSR-E Land Surface Wetness Index (LSW). All data are scaled between 10 % and 95 % and assigned units of % Saturation. Comparisons with corresponding slope statistic significantly ($p < 0.001$) greater than zero are in bold. *Na* indicates that soil moisture observations for the location were not available. Statistical abbreviations as in Table 7.

BRW

r

	SM Obs	API	BGC	L3
API	**0.49**			
BGC	**0.44**	**0.22**		
L3	-0.19	-0.04	**0.28**	
LSW	-0.18	-0.03	0.04	0.03

RMSE

	SM Obs	API	BGC	L3
API	**28.2**			
BGC	**27.3**	**26.6**		
L3	33.8	26.4	**25.1**	
LSW	32.0	23.9	27.1	24.1

MAE

	SM Obs	API	BGC	L3
API	**20.8**			
BGC	**20.4**	**18.7**		
L3	28.3	19.9	**19.8**	
LSW	26.7	18.3	22.0	18.2

MR

	SM Obs	API	BGC	L3
API	**18.0**			
BGC	**8.3**	**-6.6**		
L3	11.5	-8.2	**-2.2**	
LSW	7.0	-8.0	-4.1	-0.6

SLOPE

	SM Obs	API	BGC	L3
API	**0.34**			
BGC	**0.44**	**0.32**		
L3	-0.14	-0.05	**0.23**	
LSW	-0.12	-0.03	0.03	0.02

N

	SM Obs	API	BGC	L3
API	263			
BGC	263	303		
L3	241	281	281	
LSW	221	261	261	258

UPAD

r

	SM Obs	API	BGC	L3
API	0.11			
BGC	**0.55**	**0.27**		
L3	0.05	0.19	**0.36**	
LSW	0.13	0.02	0.06	-0.20

RMSE

	SM Obs	API	BGC	L3
API	27.1			
BGC	**20.4**	**25.3**		
L3	25.3	22.0	**20.8**	
LSW	26.3	27.2	29.6	27.0

MAE

	SM Obs	API	BGC	L3
API	19.2			
BGC	**17.8**	**18.8**		
L3	19.2	17.3	**15.8**	
LSW	22.2	22.6	24.5	22.2

MR

	SM Obs	API	BGC	L3
API	14.3			
BGC	**10.8**	**3.5**		
L3	17.0	0.6	**-3.3**	
LSW	-14.1	-9.6	-15.8	-11.2

SLOPE

	SM Obs	API	BGC	L3
API	0.11			
BGC	**0.60**	**0.29**		
L3	0.02	0.14	**0.26**	
LSW	0.17	0.01	0.05	-0.23

N

	SM Obs	API	BGC	L3
API	85			
BGC	85	280		
L3	85	261	261	
LSW	68	234	234	234

Table 12b: Same as Table 12a, but for ATQ and IVO sites.

ATQ

r

	SM Obs	API	BGC	L3
API	Na			
BGC	Na	0.07		
L3	Na	-0.06	**0.49**	
LSW	Na	**0.23**	**0.28**	0.18

RMSE

	SM Obs	API	BGC	L3
API	Na			
BGC	Na	32.5		
L3	Na	27.2	**22.4**	
LSW	Na	**21.9**	**23.8**	21.0

MAE

	SM Obs	API	BGC	L3
API	Na			
BGC	Na	24.7		
L3	Na	19.3	**18.5**	
LSW	Na	**17.4**	**19.3**	15.5

MR

	SM Obs	API	BGC	L3
API	Na			
BGC	Na	-18.1		
L3	Na	-12.0	**5.4**	
LSW	Na	**-13.3**	**3.6**	-1.8

SLOPE

	SM Obs	API	BGC	L3
API	Na			
BGC	Na	0.11		
L3	Na	-0.07	**0.39**	
LSW	Na	**0.20**	**0.16**	0.12

N

	SM Obs	API	BGC	L3
API	Na	326		
BGC	Na	326	326	
L3	Na	307	307	307
LSW	Na	295	295	295

IVO

r

	SM Obs	API	BGC	L3
API	Na			
BGC	Na	0.11		
L3	Na	0.10	0.00	
LSW	Na	-0.02	-0.20	-0.01

RMSE

	SM Obs	API	BGC	L3
API	Na			
BGC	Na	27.4		
L3	Na	20.2	27.1	
LSW	Na	24.4	30.5	24.4

MAE

	SM Obs	API	BGC	L3
API	Na			
BGC	Na	21.5		
L3	Na	14.6	20.0	
LSW	Na	18.9	23.5	21.0

MR

	SM Obs	API	BGC	L3
API	Na			
BGC	Na	-3.3		
L3	Na	7.0	9.5	
LSW	Na	-8.8	-7.7	-17.1

SLOPE

	SM Obs	API	BGC	L3
API	Na			
BGC	Na	0.15		
L3	Na	0.06	0.00	
LSW	Na	-0.01	-0.13	-0.02

N

	SM Obs	API	BGC	L3
API	Na			
BGC	Na	312		
L3	Na	292	292	
LSW	Na	260	260	259

Table 12c: Same as Table 12a, but for HPV and NOBS sites.

HPV

r

	SM Obs	API	BGC	L3
API	**0.38**			
BGC	0.13	0.09		
L3	**0.76**	**0.57**	0.14	
LSW	**0.49**	**0.36**	0.07	**0.27**

RMSE

	SM Obs	API	BGC	L3
API	**35.3**			
BGC	35.3	29.3		
L3	**41.0**	**15.7**	28.9	
LSW	**27.4**	**20.1**	28.9	**23.6**

MAE

	SM Obs	API	BGC	L3
API	**30.4**			
BGC	29.4	22.2		
L3	**37.2**	**10.8**	19.7	
LSW	**22.0**	**16.5**	25.6	**20.5**

MR

	SM Obs	API	BGC	L3
API	**29.3**			
BGC	12.9	-6.7		
L3	**36.4**	**8.3**	14.8	
LSW	**20.2**	**-11.5**	-5.3	**-18.9**

SLOPE

	SM Obs	API	BGC	L3
API	**0.21**			
BGC	0.19	0.14		
L3	**0.13**	**0.25**	0.04	
LSW	**0.30**	**0.36**	0.04	**0.55**

N

	SM Obs	API	BGC	L3
API	118			
BGC	118	316		
L3	111	296	296	
LSW	105	261	261	260

NOBS

r

	SM Obs	API	BGC	L3
API	**0.67**			
BGC	**0.39**	**0.27**		
L3	-0.32	-0.42	0.11	
LSW	-0.24	-0.10	-0.31	0.08

RMSE

	SM Obs	API	BGC	L3
API	**31.6**			
BGC	**21.0**	**29.2**		
L3	39.9	27.0	31.6	
LSW	29.9	30.0	24.2	29.4

MAE

	SM Obs	API	BGC	L3
API	**28.6**			
BGC	**15.4**	**26.0**		
L3	34.3	19.6	28.3	
LSW	25.4	24.8	19.8	26.7

MR

	SM Obs	API	BGC	L3
API	**27.3**			
BGC	**4.7**	**-22.2**		
L3	23.6	1.9	23.8	
LSW	5.7	-19.0	3.2	-20.9

SLOPE

	SM Obs	API	BGC	L3
API	**0.47**			
BGC	**0.27**	**0.25**		
L3	-0.28	-0.40	0.11	
LSW	-0.18	-0.08	-0.30	0.08

N

	SM Obs	API	BGC	L3
API	250			
BGC	250	400		
L3	250	381	381	
LSW	223	337	337	337

Table 12d: Same as Table 12a, but for OAS and LTH sites.

OAS

r

	SM Obs	API	BGC	L3
API	**0.42**			
BGC	**0.68**	**0.48**		
L3	**0.54**	0.13	**0.16**	
LSW	0.15	**0.48**	0.07	**0.22**

RMSE

	SM Obs	API	BGC	L3
API	**41.7**			
BGC	**31.5**	**28.8**		
L3	**26.8**	27.6	**32.1**	
LSW	36.2	**18.8**	32.5	**18.3**

MAE

	SM Obs	API	BGC	L3
API	**33.6**			
BGC	**22.4**	**17.7**		
L3	**23.0**	23.9	**29.6**	
LSW	28.7	**16.5**	27.5	**14.0**

MR

	SM Obs	API	BGC	L3
API	**32.8**			
BGC	**20.9**	**-11.9**		
L3	**12.2**	-21.4	**-9.0**	
LSW	21.1	**-12.3**	0.4	**9.0**

SLOPE

	SM Obs	API	BGC	L3
API	**0.21**			
BGC	**0.72**	**1.02**		
L3	**0.23**	0.11	**0.06**	
LSW	0.07	**0.45**	0.03	**0.25**

N

	SM Obs	API	BGC	L3
API	535			
BGC	535	535		
L3	513	513	513	
LSW	474	474	474	474

LTH

r

	SM Obs	API	BGC	L3
API	**0.47**			
BGC	**0.71**	**0.29**		
L3	**0.40**	**0.32**	**0.44**	
LSW	**0.64**	**0.59**	**0.51**	**0.58**

RMSE

	SM Obs	API	BGC	L3
API	**26.3**			
BGC	**23.5**	**18.9**		
L3	**29.7**	**15.7**	**15.7**	
LSW	**20.2**	**15.0**	**17.3**	**16.8**

MAE

	SM Obs	API	BGC	L3
API	**20.1**			
BGC	**19.3**	**12.7**		
L3	**24.5**	**11.2**	**12.0**	
LSW	**16.2**	**11.2**	**13.9**	**13.5**

MR

	SM Obs	API	BGC	L3
API	**17.3**			
BGC	**17.6**	**0.3**		
L3	**21.7**	**4.4**	**3.9**	
LSW	**10.7**	**-6.8**	**-7.1**	**-11.6**

SLOPE

	SM Obs	API	BGC	L3
API	**0.32**			
BGC	**0.55**	**0.33**		
L3	**0.18**	**0.21**	**0.26**	
LSW	**0.42**	**0.59**	**0.45**	**0.90**

N

	SM Obs	API	BGC	L3
API	566			
BGC	566	576		
L3	547	557	557	
LSW	463	471	471	471

FIGURES

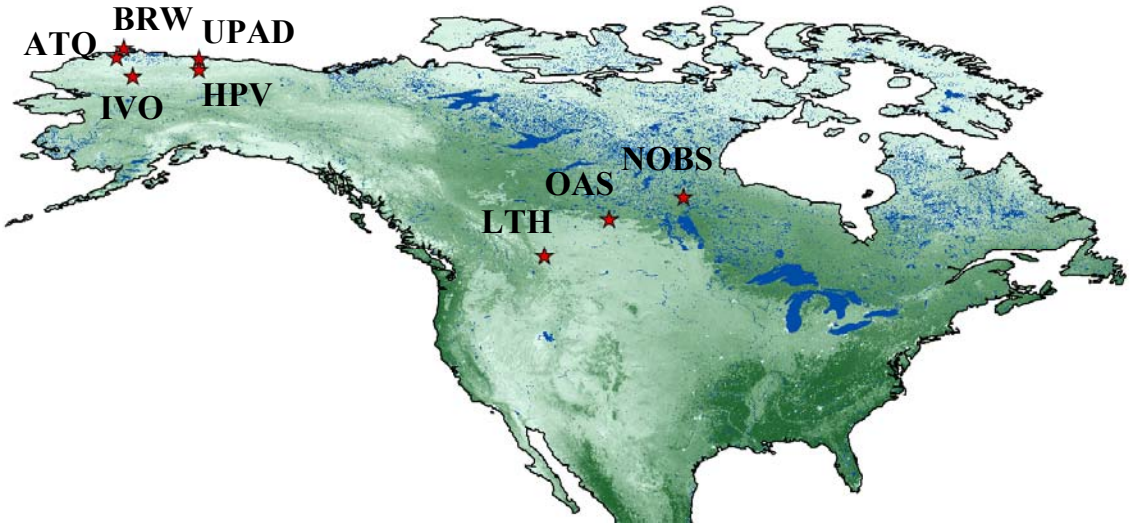

Figure 1: Biophysical network study sites. Site abbreviations described in Table 1.

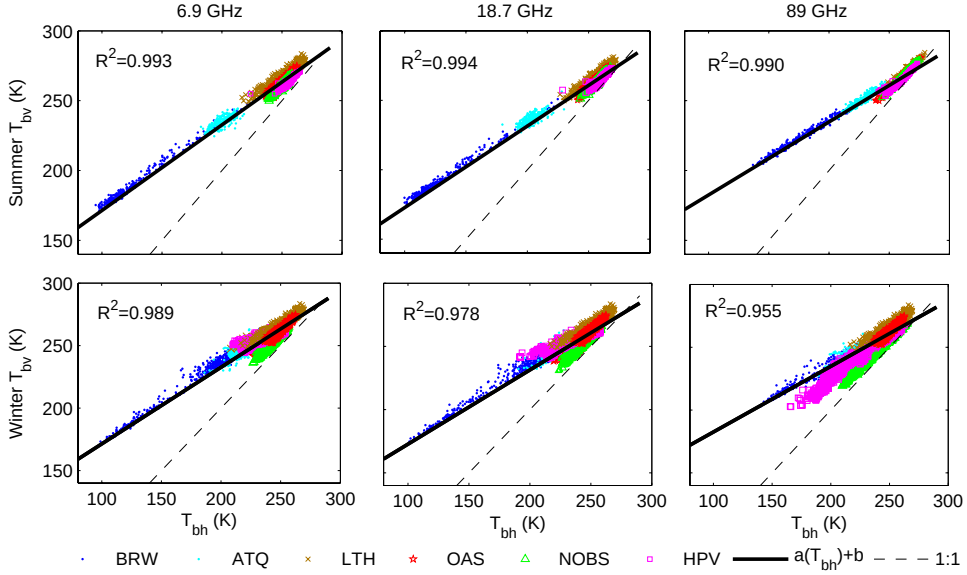

Figure 2: Observed AMSR-E T_{bh} vs. T_{bv} relations at the study sites. The R^2 statistic indicates the level of linear correlation between T_{bh} vs. T_{bv} at BRW for each frequency. The black straight line represents the appropriate *a* and *b* parameters from Table 3 and the mean summer T_{soil} at BRW. The dashed straight line represents a 1:1 relationship.

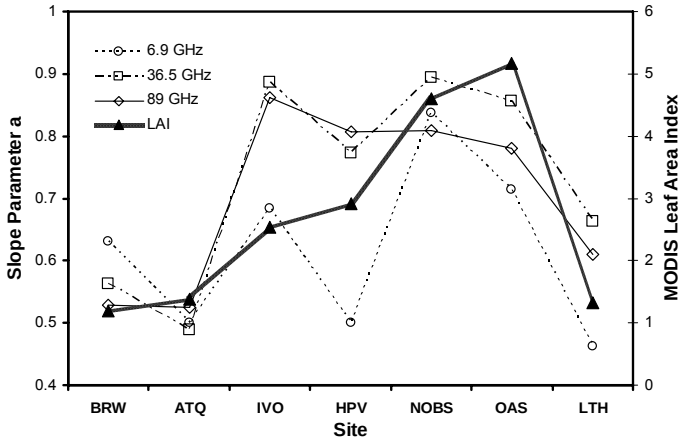

Figure 3: Apparent slope parameter *a* derived by fitting (11) to the e_h vs. e_v emissivity relation at each site for each AMSR-E frequency. Maximum annual MODIS Leaf Area Index (LAI) for the dominant vegetation type is on the secondary y-axis.

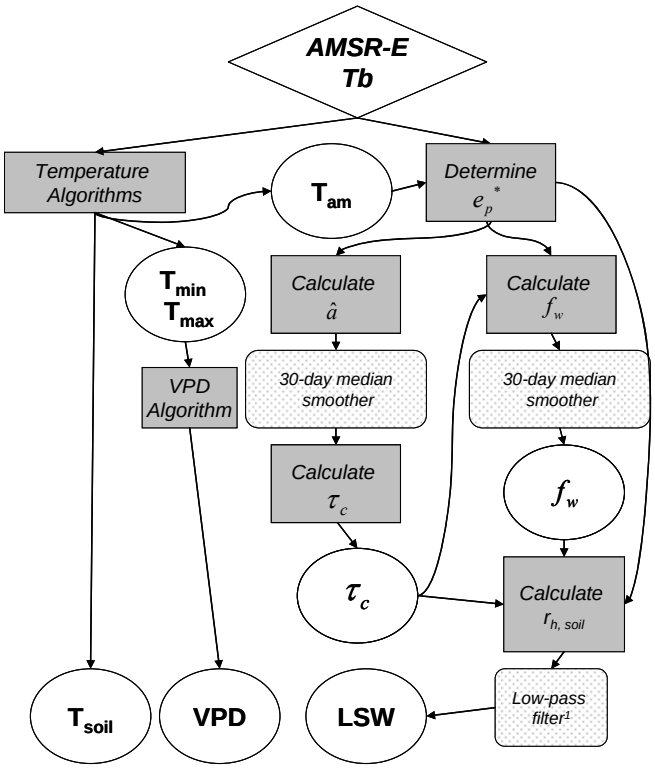

Figure 4: Flowchart showing algorithm structure and processing order of AMSR-E products created in this investigation. The diamond cell represents dual-polarization multi-frequency AMSR-E L2a brightness temperatures, darkly-shaded square cells represent calculations, lightly-shaded square cells represent time-series smoothing and filtering, and circles represent products, which include end products and products re-employed in the processing scheme. See section IV for details and abbreviations.

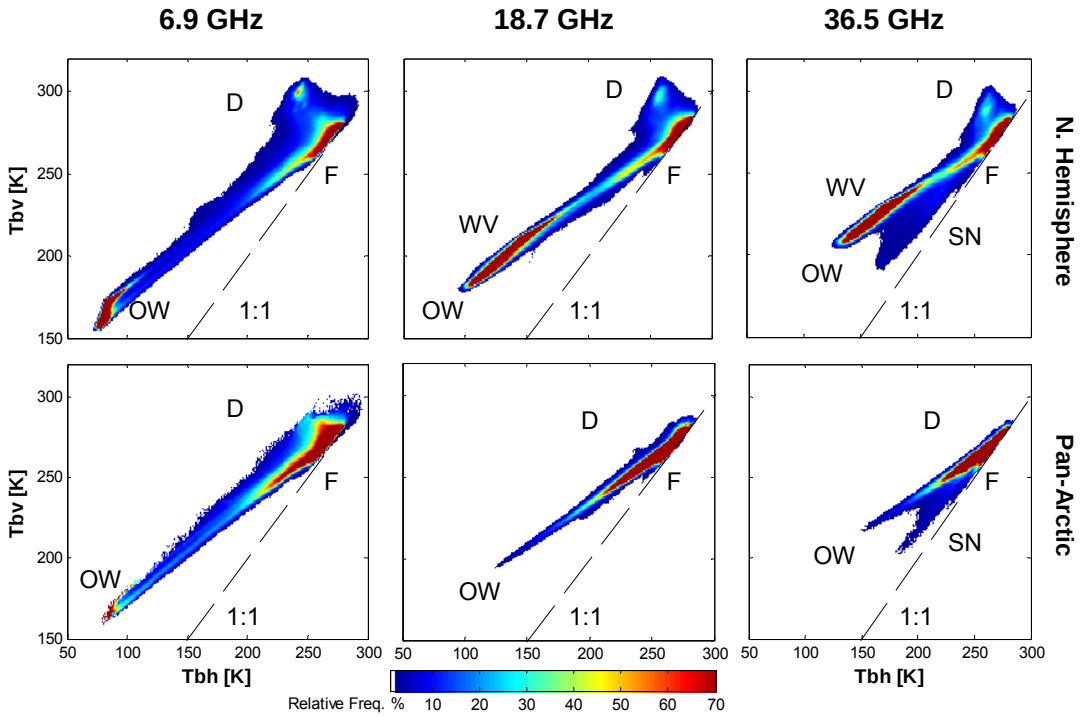

Figure 5: Histograms (1 K bins) of the entire Northern Hemisphere (land and ocean areas; June-September 2003) T_{bv} vs. T_{bh} at 6.9 GHz, 18.7 GHz, and 36.5 GHz frequencies (upper plots). Histograms (1 K bins) for the entire Pan-Arctic basin (land and inland waters with watersheds flowing into the Arctic Ocean; June-September 2003) T_{bv} vs. T_{bh} at 6.9 GHz, 18.7 GHz, and 36.5 GHz frequencies (lower plots). The letter labels represent locations of homogenous *land cover* (or atmospheric effects) that have strong influence on AMSR-E Tb observations: Open water with either fresh or saltwater (OW); Desert locations with sparse or no vegetation (D); Densely forested areas including Boreal, temperate, and tropical forests (F); Snow cover and permanent ice (SN); Atmospheric water vapor absorption (WV) associated with storms over the ocean. Dashed lines indicate 1:1.

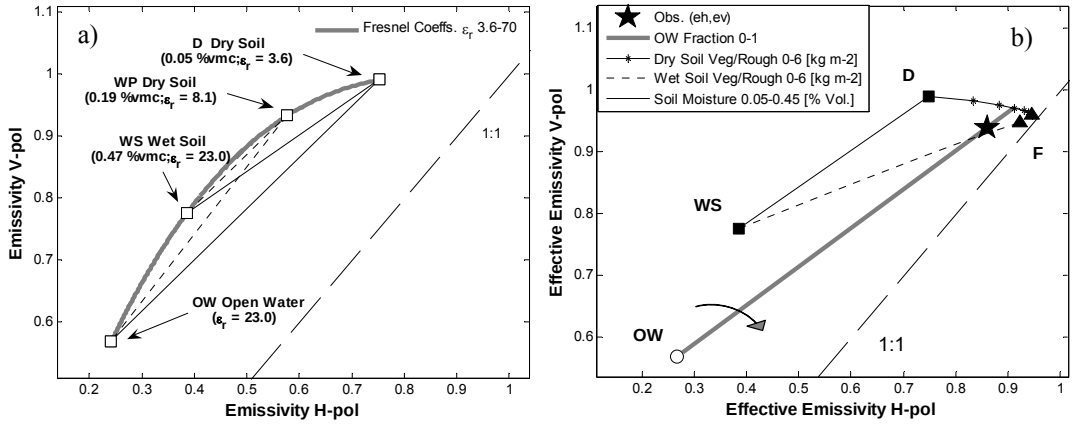

Figure 6: (a) Theoretical basis for separating the influence of open water from soil moisture over bare, smooth soil. Solid gray line represents the Fresnel relationship with the real part of the complex dielectric (ε_r) increasing from 3.6 (Dry Soil) to 70 (Open Water). Solid black lines WS-D and OW-D represent the prediction for a two-component surface with varying fractions of dry loam soil (D) and at saturation (WS) and for dry loam soil and open water (OW), respectively. Finely dashed black lines WS-WP and OW-WP show the same situation but for loam soil at the plant wilting point (WP). (b) Representation of the LSW algorithm in H-V emissivity space. Points D, WS, and OW correspond to the same in (a) and also in Fig. 10 with the addition of F. Increasing vegetation biomass increases the slope of the line between (e_h^*, e_v^*) and point OW (curved arrow). Broadly dashed lines represent 1:1 in both plots.

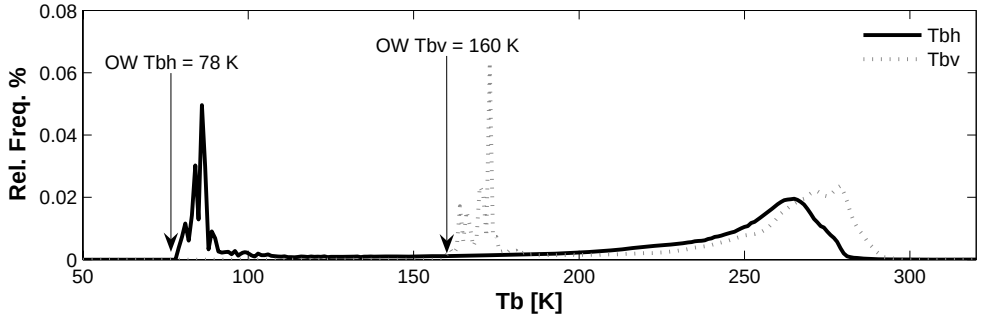

Figure 7: Histograms of 6.9 GHz T_{bh} and T_{bv} for June 1-Sept. 31, 2003 across the Northern Hemisphere used for determining the emissivity of open water (OW). Plot represents the distribution of points from Fig. 5 for the T_{bh} - and T_{bv} - axes.

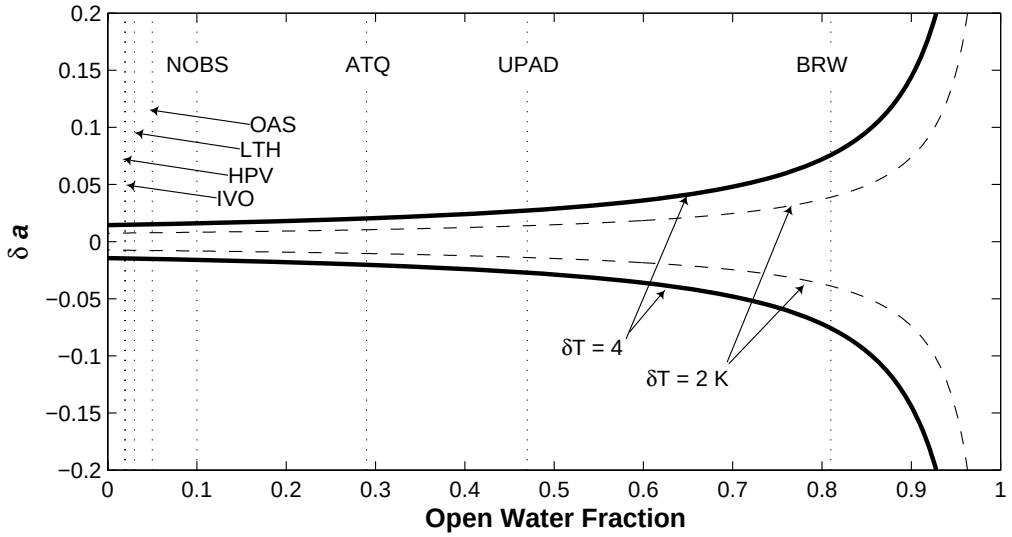

Figure 8: Uncertainty in estimated slope (δa) between land fraction emissivity and open water with increasing open water fraction. Small error in emissivity estimation from errors in land surface temperature estimates (δT), greatly increases uncertainty in land fraction emissivity as open water fraction approaches 1. The effect of 0.5 K radiometer noise is very small and within the thickness of the displayed lines. Mean maximum annual estimated AMSR-E 6.9 GHz for the observation period (June 19, 2002-Dec. 31, 2004) shown as dashed vertical lines.

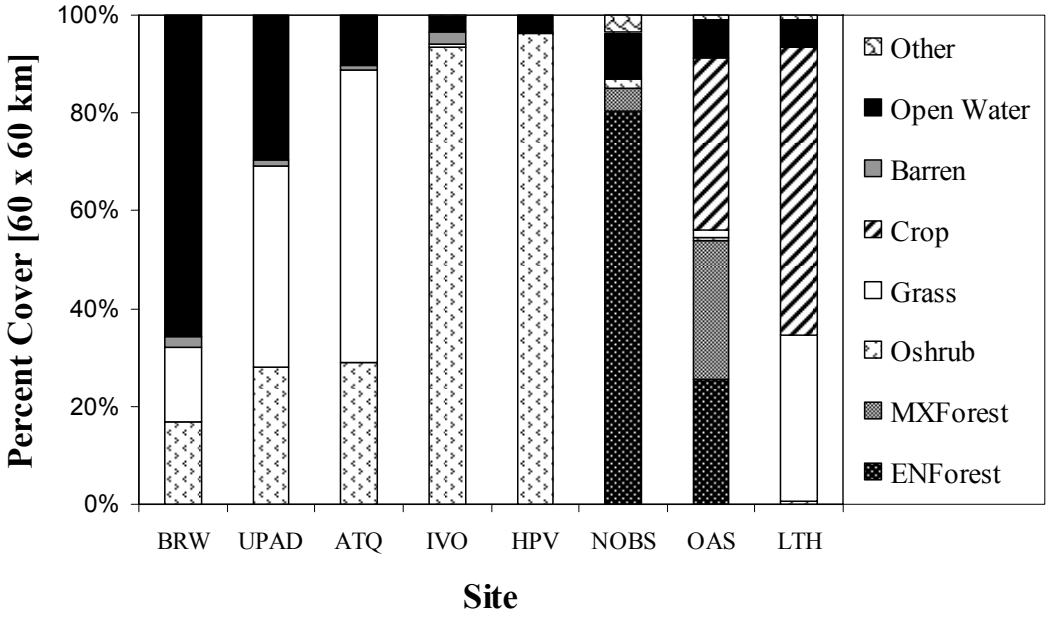

Figure 9: Percent of MODIS International Geosphere-Biosphere Programme (IGBP) 1-km pixels falling into each land cover class for 60 km x 60 km window extracted over the study sites. Land cover classes are open water, barren areas, crops, grass, open shrubland (Oshrub), mixed forest (MXForest), evergreen needle-leaf forest (ENForest), and other for any IGBP land cover class within the window outside of those listed.

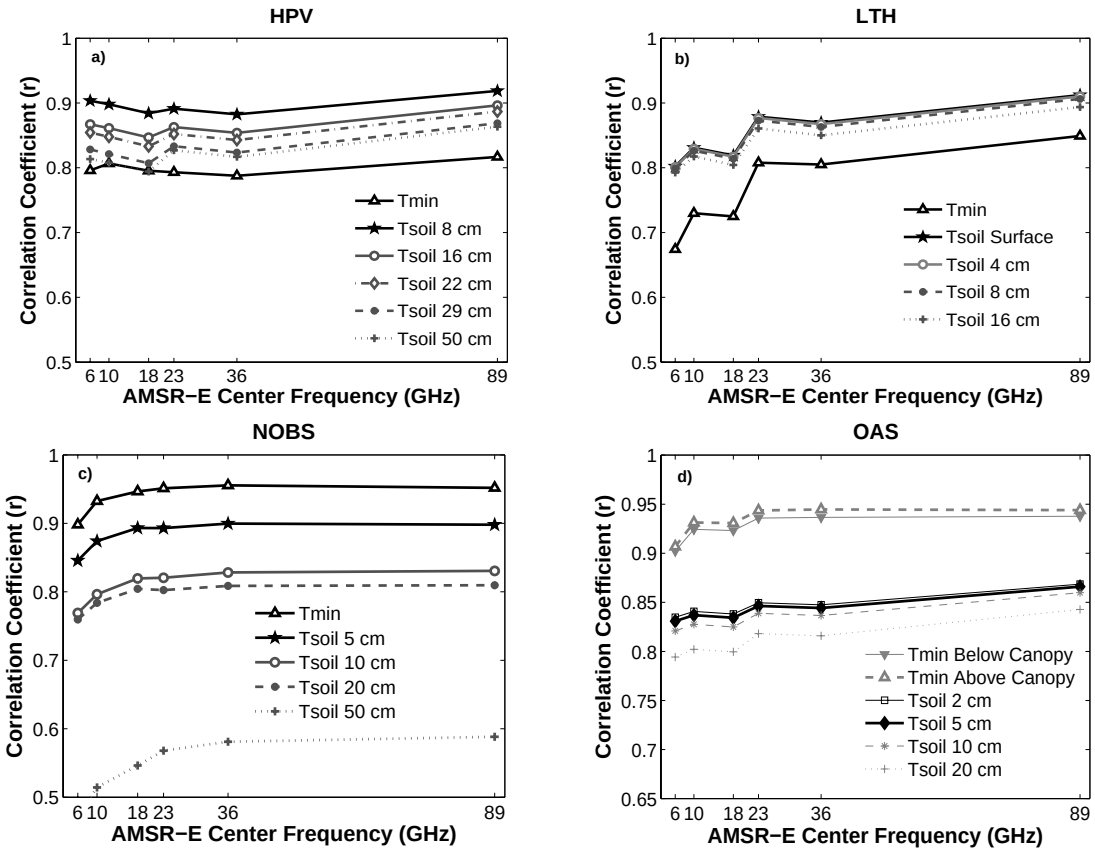

Figure 10: Linear correlation between AMSR-E uncorrected T_{bv} values for various frequencies and *in situ* minimum daily air temperature (T_{min}) and soil temperature (T_{soil}) measurements for selected study sites. Note that the soil and air temperature measurement levels are different for each plot as measurement depth differed between each site.

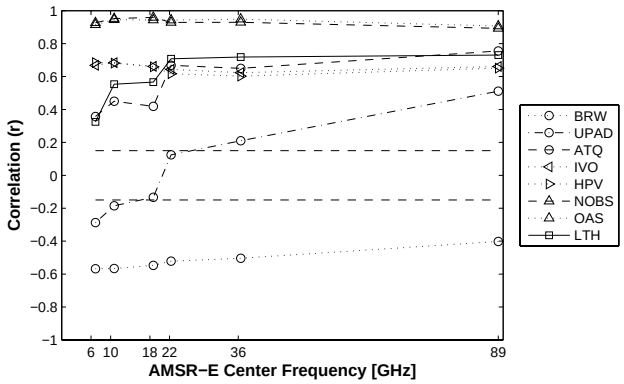

Figure 11: Linear correlation of AMSR-E multi-frequency T_{bv} to *in situ* air temperature (~2 m) by study site corresponding to the time of the descending (am) satellite overpass.

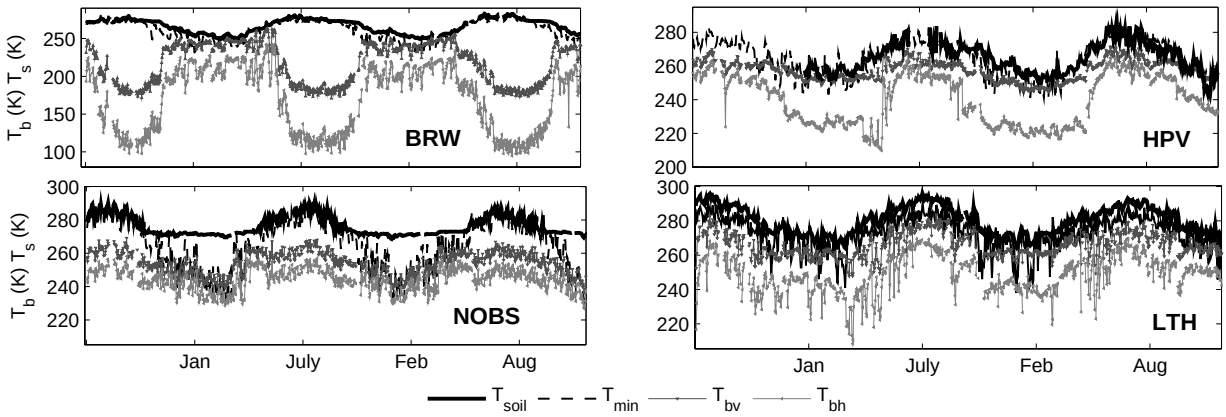

Figure 12: AMSR-E 6.9 GHz V and H polarized brightness temperatures over selected study sites from 2002 to 2004.

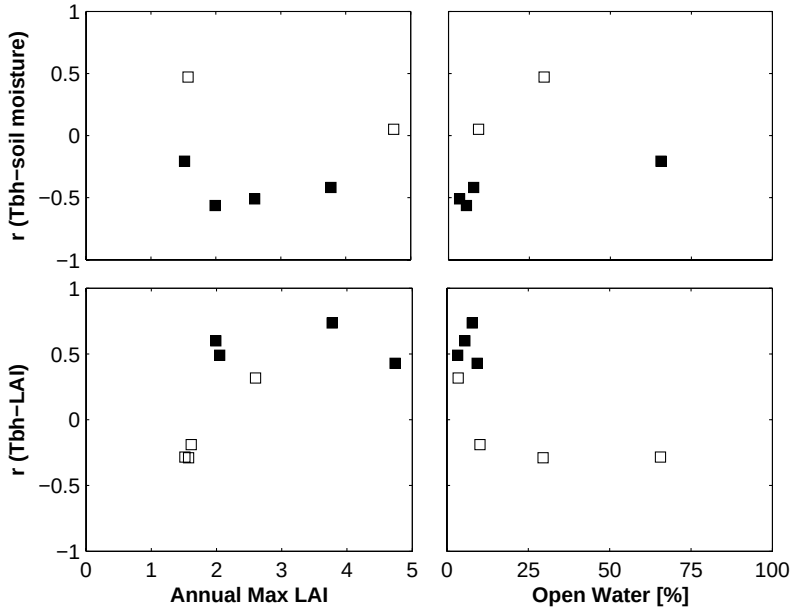

Figure 13: Linear correlation coefficient (*r*) between AMSR-E 6.9 GHz T_{bh} and site observed soil moisture (< 8 cm) and AMSR-E 6.9 GHz T_{bh} and MODIS 8-day LAI plotted against maximum annual MODIS LAI and percent open water derived from MODIS IGBP land cover 60 km x 60 km window extractions. Closed symbols indicate that correlation is significant ($p < 0.05$) of expected sign (see Table 6).

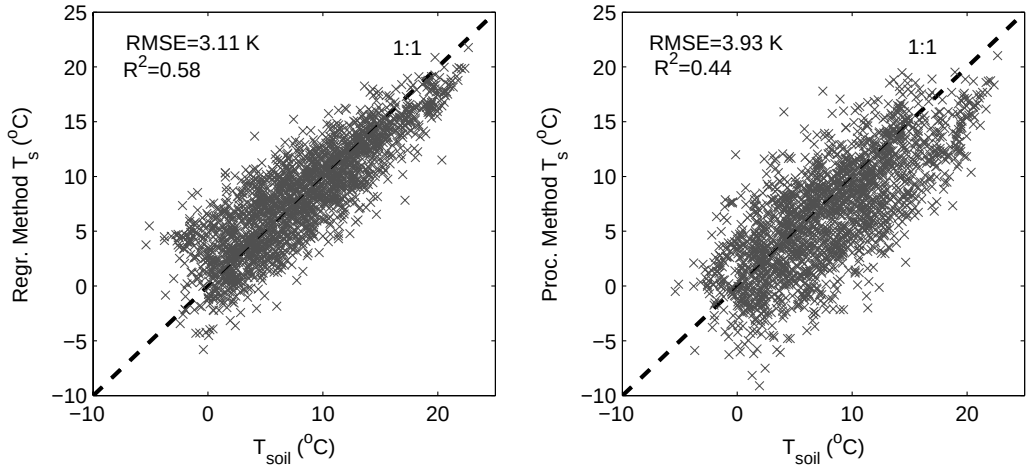

Figure 14: Scatter plot of 2004 thawed-season retrievals for the regression and process-based AMSR-E T_s methods and associated statistics.

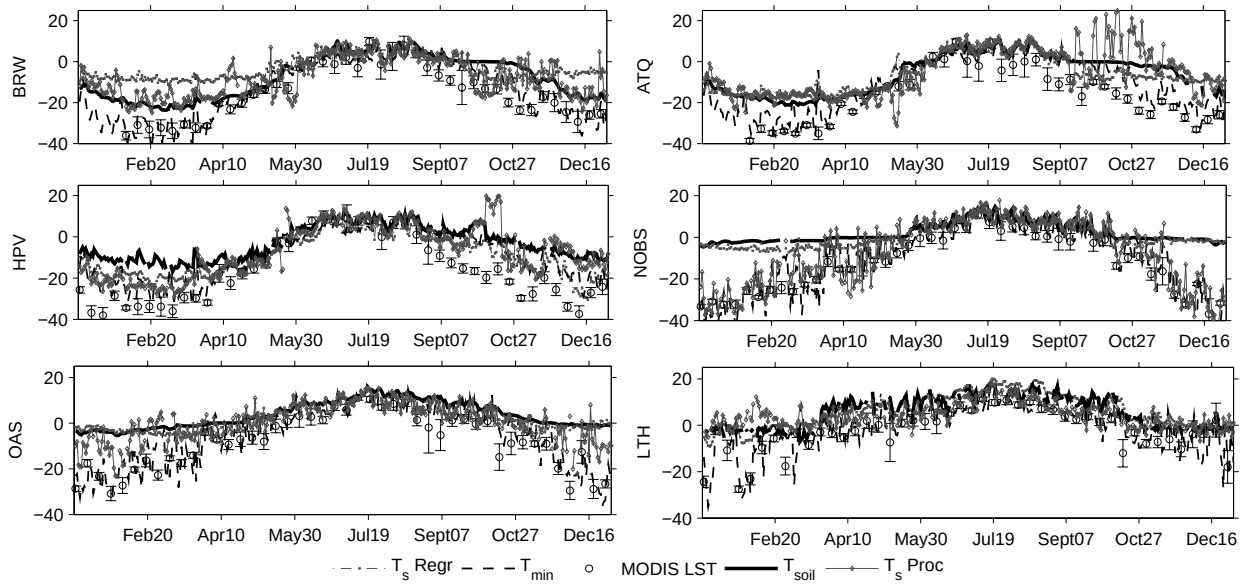

Figure 15: Both methods of AMSR-E T_s retrievals (°C) plotted against T_{soil}, T_{min}, and MODIS LST at the study sites for 2004. MODIS LST error bars represent the standard deviation of the 1 km x 1 km resolution based MODIS LST results within a 60 km x 60 km window centered at each site.

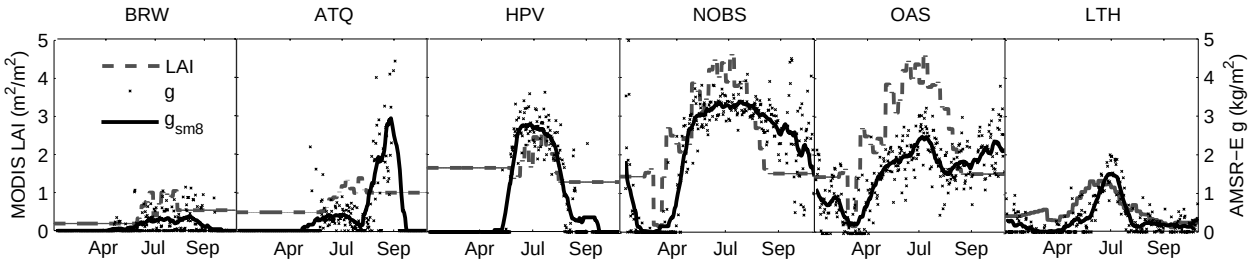

Figure 16: MODIS 8-day LAI (m^2/m^2) time series and AMSR-E g (kg/m^2) vegetation/roughness parameter results for 2003. The points represent daily values of g, while the solid black lines represent an 8-day running average (g_{sm8}).

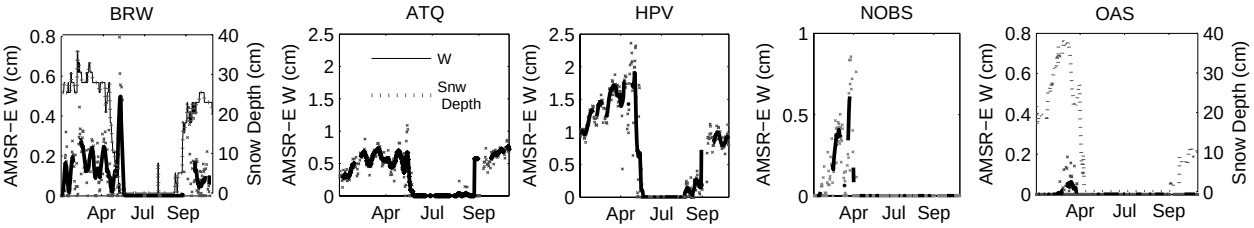

Figure 17: Snow depth at BRW and OAS (dashed gray lines) and AMSR-E W_s (cm)**.** The points represent daily values of W, while the solid black lines represent an 8-day running average.

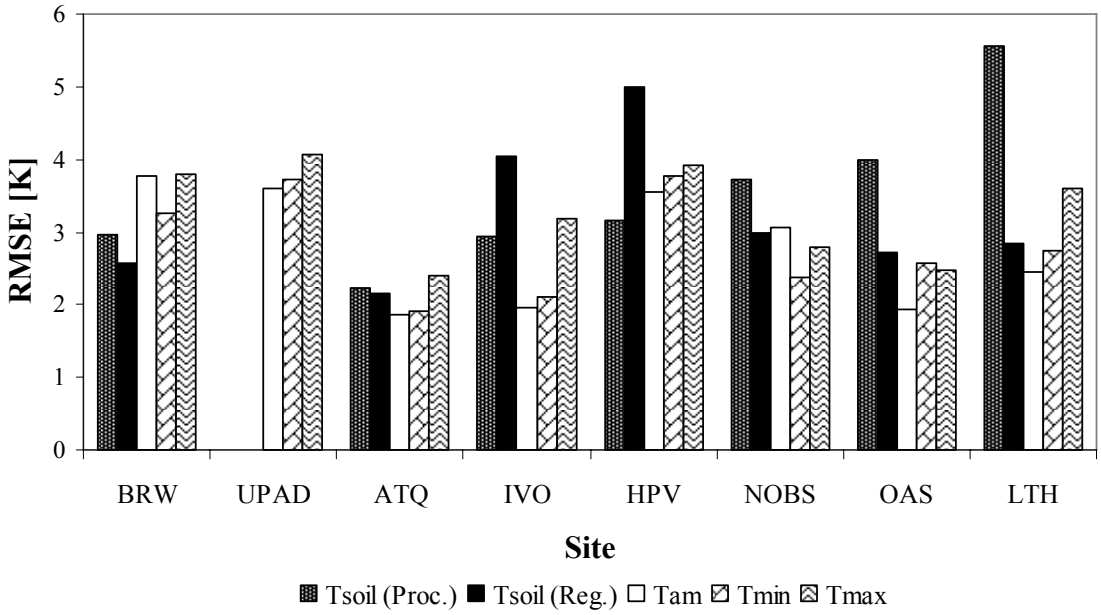

Figure 18: Root mean square error (RMSE) in Kelvin (K) for all AMSR-E temperature algorithms considered in this investigation. Values are tabulated in Table 7 and Table 9.

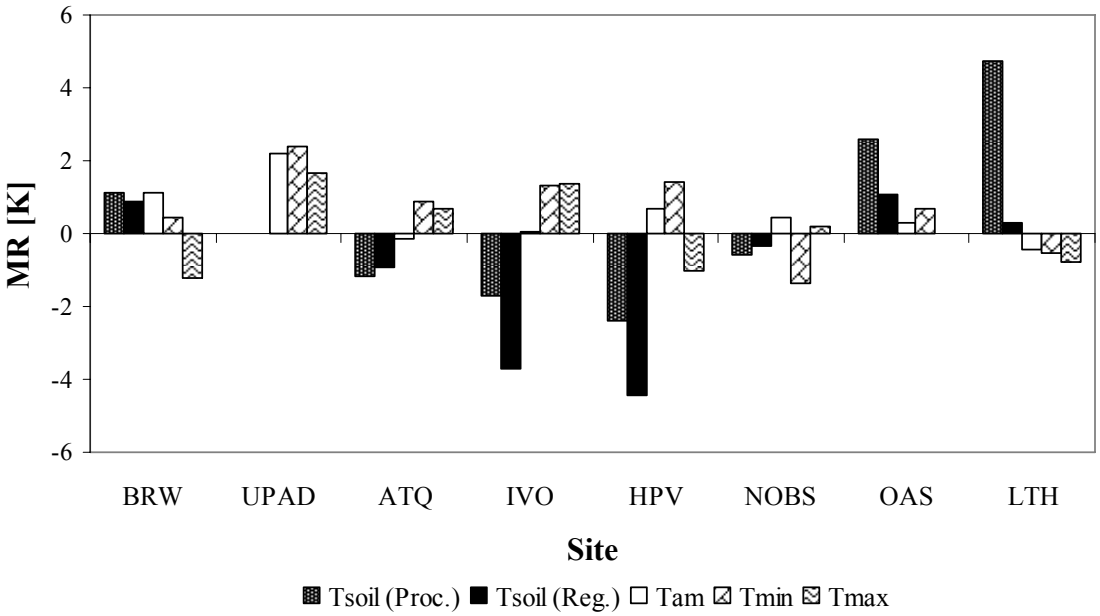

Figure 19: Mean residual (MR) in Kelvin (K) for all AMSR-E temperature algorithms considered in this investigation. Values are tabulated in Table 7 and Table 9.

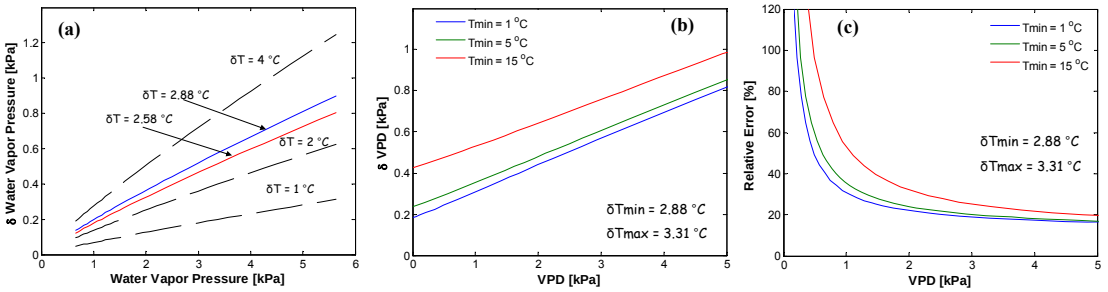

Figure 20: a) Error introduced in saturation water vapor pressure for given levels of error in air temperature. b) Error introduced in VPD estimates from independent errors (δT) in T_{min} and T_{max} inputs for fixed levels of T_{min}. c) Relative error (%; $\delta VPD / VPD * 100$) introduced in VPD estimates from independent errors (δT) in T_{min} and T_{max} inputs for fixed levels of T_{min}.

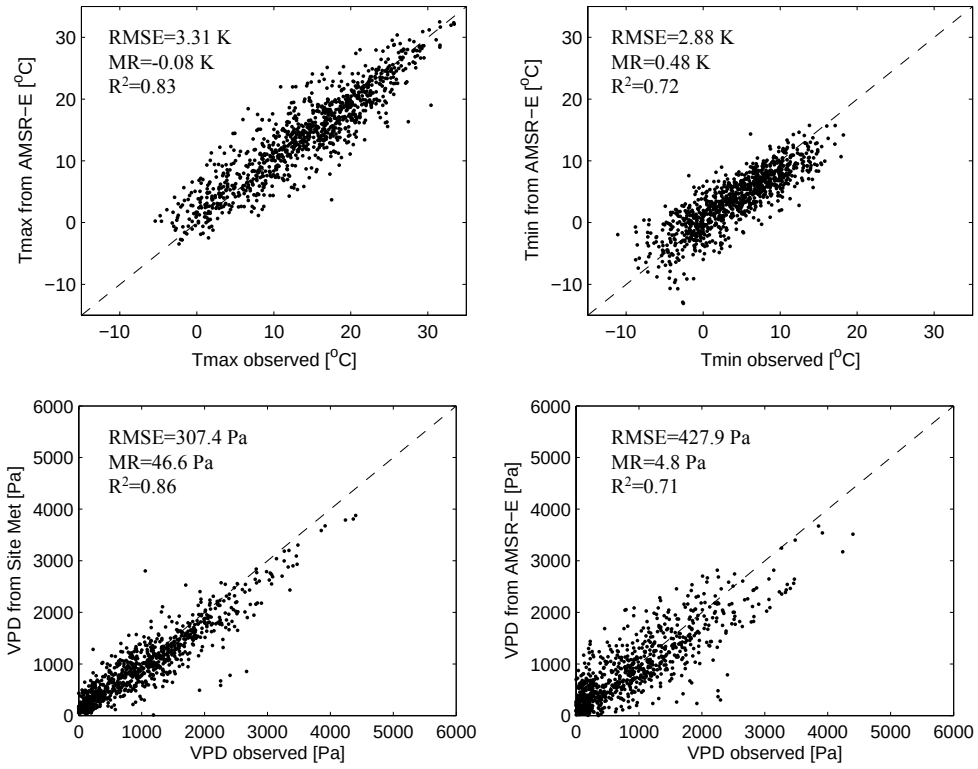

Figure 21: Overall results from validation of AMSR-E T_{max} and T_{min} against site observations and associated statistics (upper plots). Overall results from prediction of VPD from the VPD algorithm run on site observed meteorology and from prediction of VPD using AMSR-E T_{max} and T_{min} vs. site observations of VPD and associated statistics (lower plots). Dashed line represents 1:1.

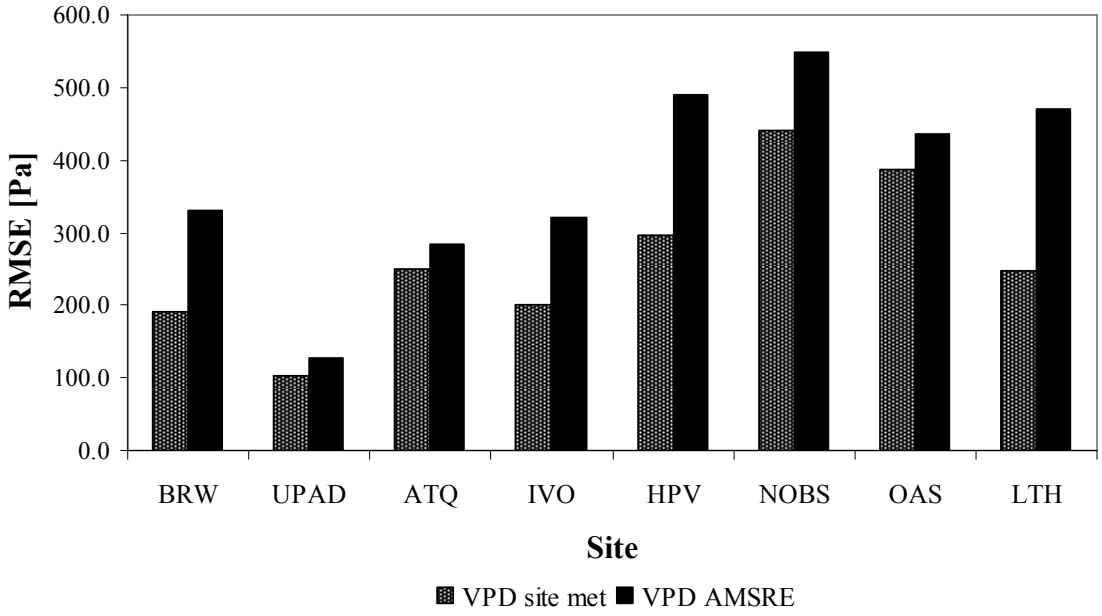

Figure 22: Root mean square error (RMSE) in pascals (Pa) for the VPD algorithm run on site meteorology and the VPD algorithm with AMSR-E meteorology. Values are tabulated in Table 10.

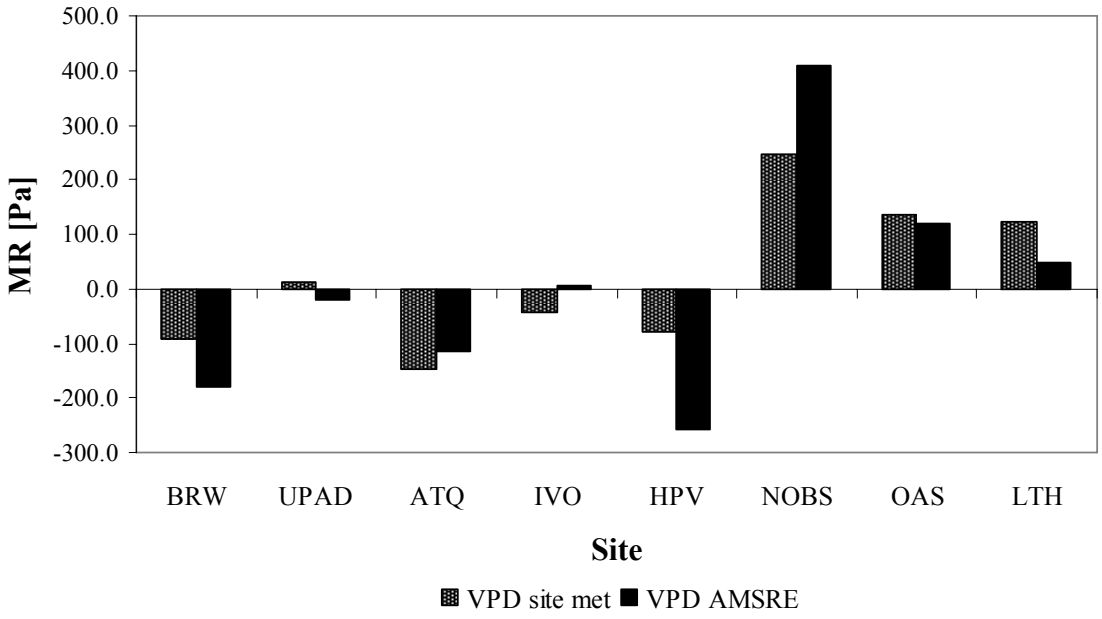

Figure 23: Mean residual (MR) in pascals (Pa) for the VPD algorithm run on site meteorology and the VPD algorithm with AMSR-E meteorology. Values are tabulated in Table 10.

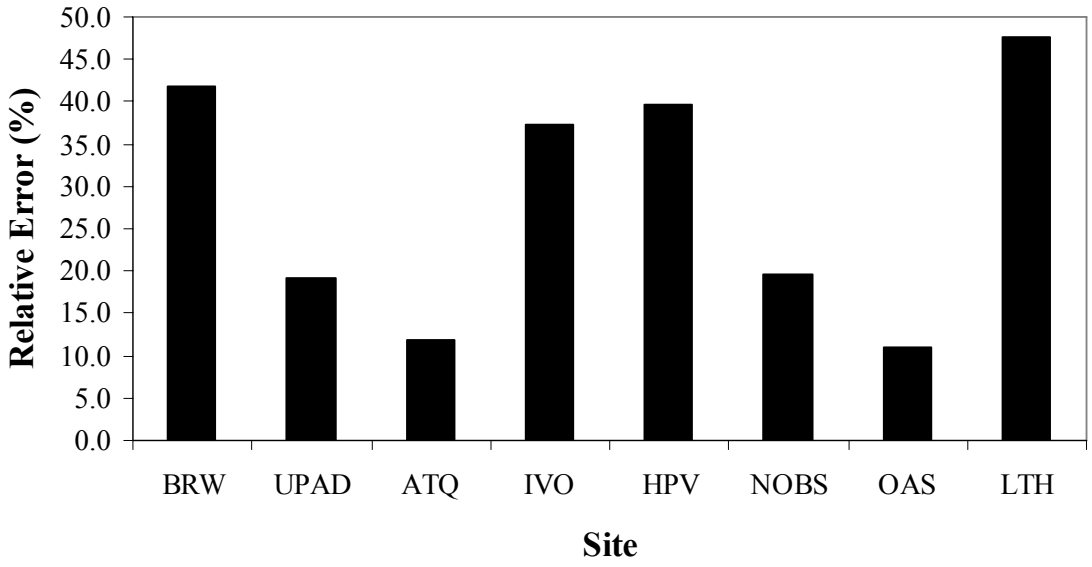

Figure 24: Relative amount of error introduced by employing the AMSR-E meteorology in the VPD algorithm plotted as a percentage of overall AMSR-E VPD retrieval RMSE.

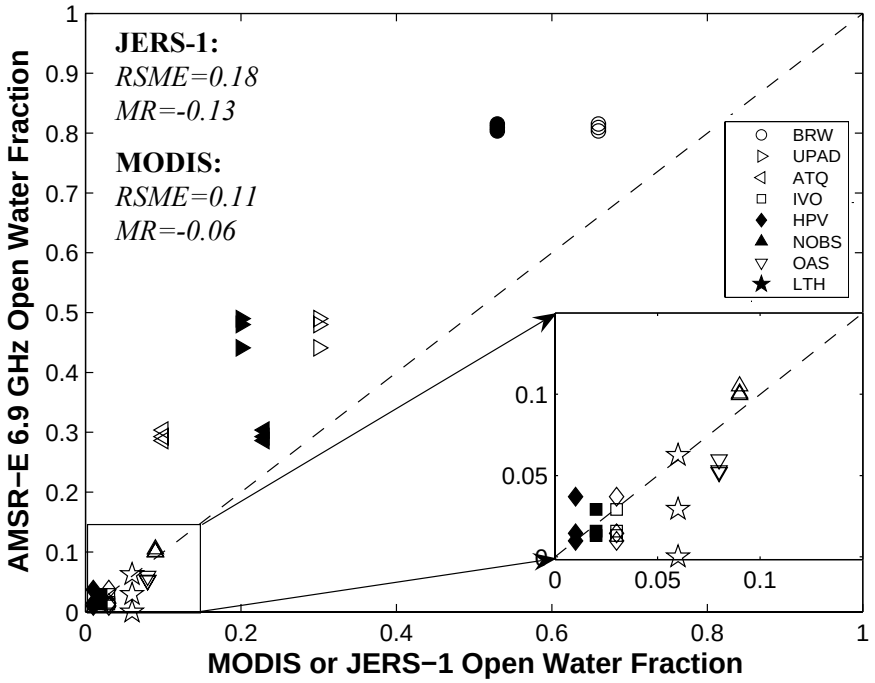

Figure 25: Maximum annual open water fraction estimated from AMSR-E 6.9 GHz (2002-2004) compared to JERS-1 EASE-grid open water map and MODIS land cover with relevant statistics. Symbol shapes same as fig. 13, except that closed symbols stand for JERS-1 and open symbols stand for MODIS. JERS-1 data were only available for Alaska North Slope locations.

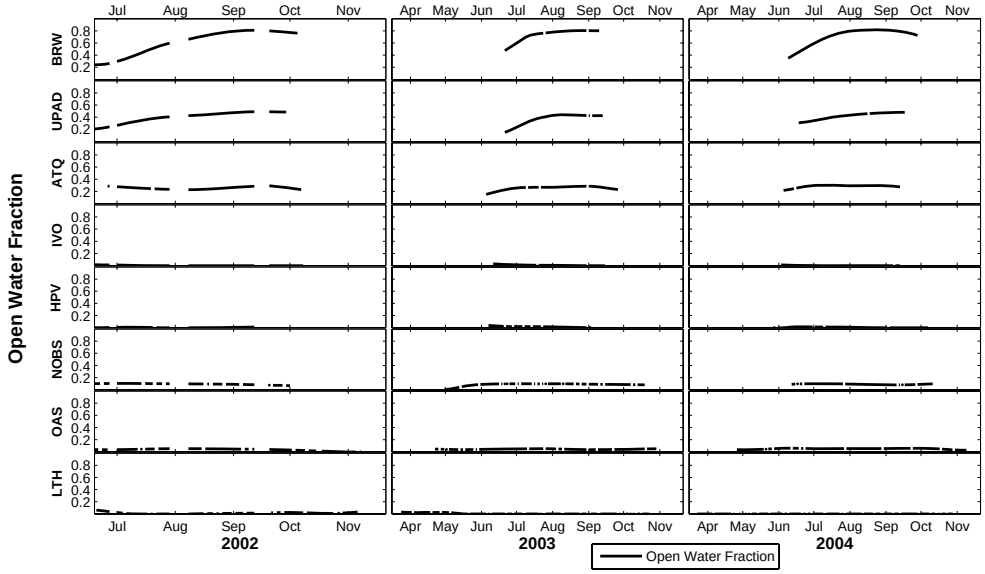

Figure 26: Time series of thawed season open water fraction by study location derived from AMSR-E 6.9 GHz observations. Gaps in the AMSR-E lines represent missing daily values.

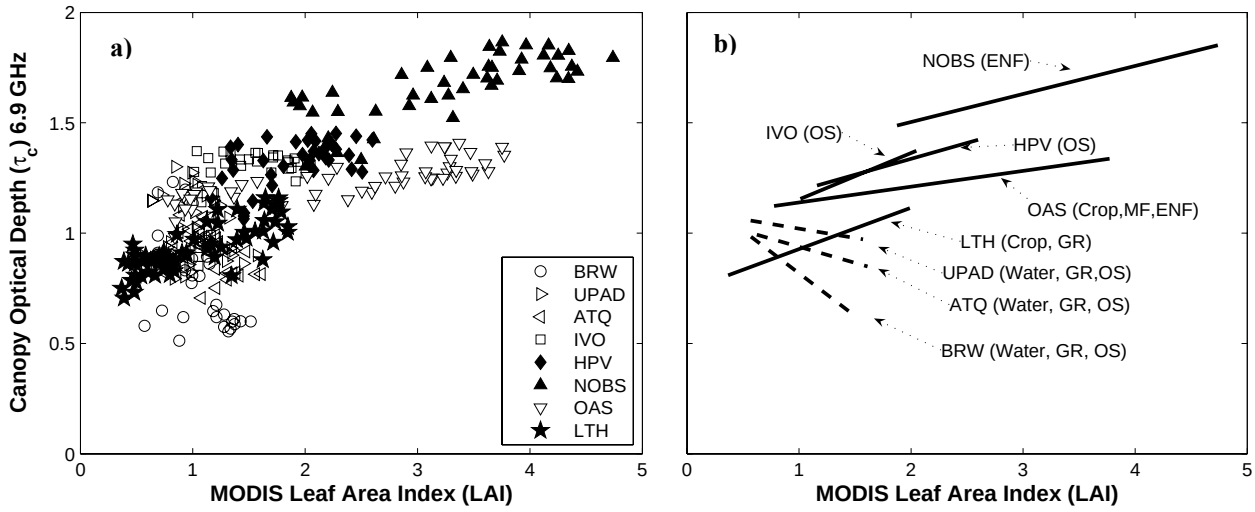

Figure 27: (a) Relation between AMSR-E 6.9 GHz canopy optical depth (τ_c) and MODIS 8-day Leaf Area Index (LAI) means derived from 60 km x 60 km windows. The lines represent linear least-squares fits for each location. Statistics for the lines are in Table 11.

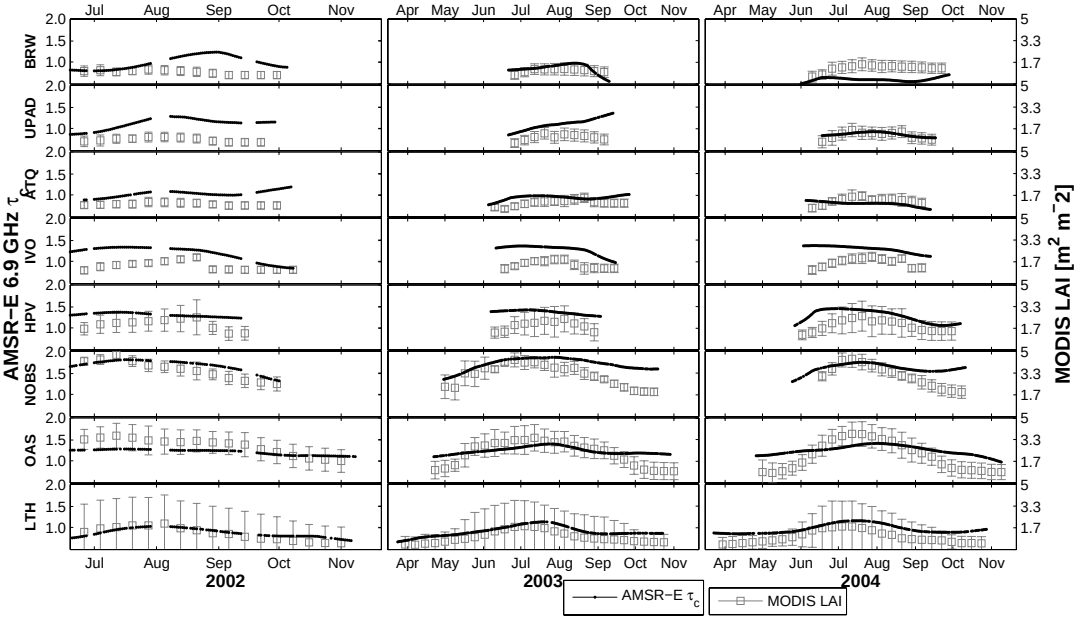

Figure 28: Time series of thawed season AMSR-E 6.9 GHz canopy optical depth (τ_c) and MODIS 8-day LAI by study location. Error bars represent one standard deviation from the mean 8-day LAI within 60 km x 60 km windows. Gaps in the AMSR-E lines represent missing daily values.

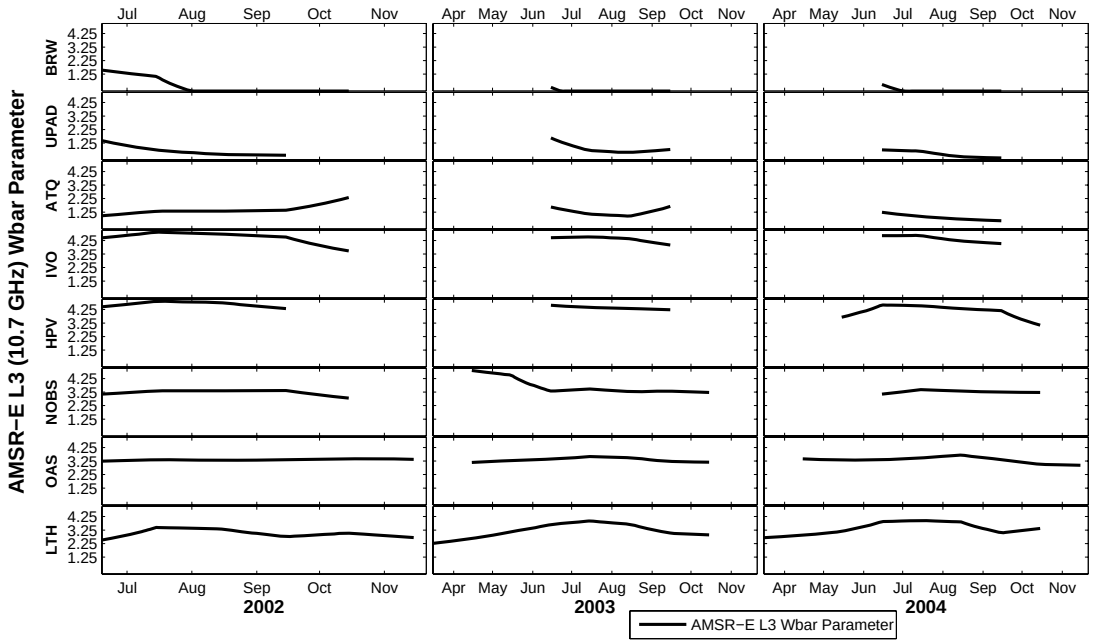

Figure 29: Time series of thawed season NASA L3 soil moisture algorithm $\overline{w}$ parameter by study location. The $\overline{w}$ parameter contains information on both vegetation biomass and open water fraction combined.

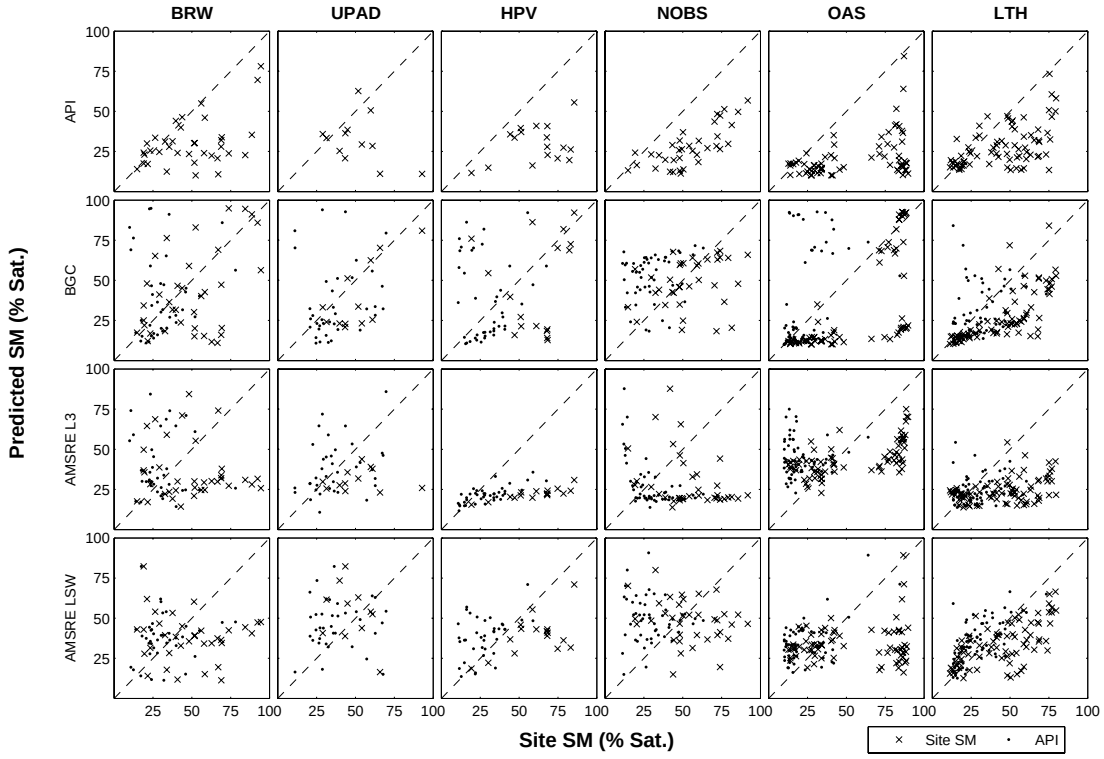

Figure 30: Scatterplots of model (API, BGC) and AMSR-E soil moisture algorithm (L3, LSW) results vs. site observed soil moisture and API (all in % saturation) by study location. Composites of 8-day means are displayed to improve visualization. The associated statistics for the daily values are shown in Tables 12a-d. Dashed lines represent 1:1 for each panel.

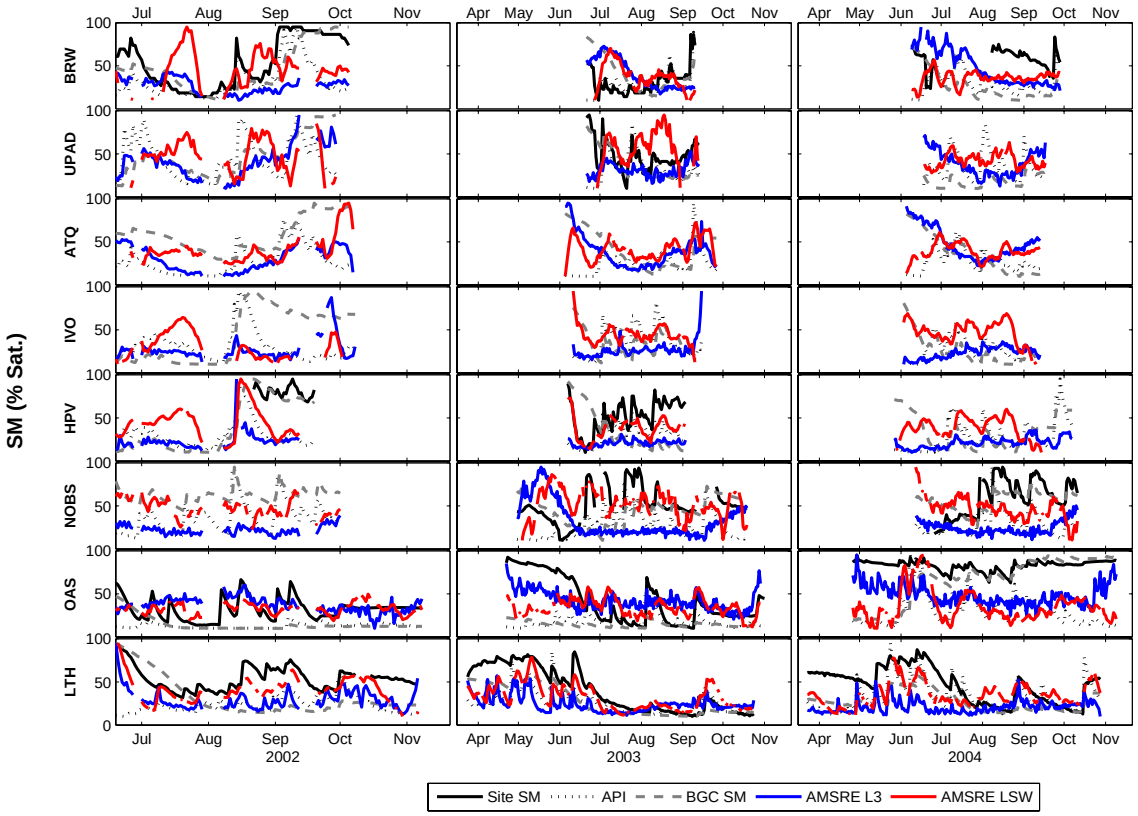

Figure 31: Time series of thawed season model (API, BGC), AMSR-E soil moisture algorithm (L3, LSW) results, and site observed soil moisture by location and year for the observation period (June 19, 2002 to Dec. 31, 2004). Plots depict growing season differences and time series correspondence between locations down each column and across time within a site across each row.

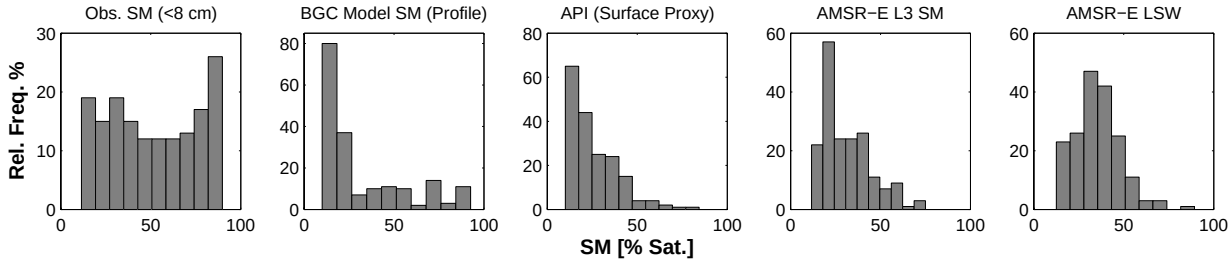

Figure 32: Histograms of soil moisture across locations where the AMSR-E algorithms showed correspondence to both site observed soil moisture (< 8 cm) and API (LTH, OAS, and HPV).

APPENDICIES

Appendix A Symbol List and Description

Site Observation Symbols

Symbol	Units	Description
T_{soil}	[K] or [°C]	Observed soil temperature (0-5 cm depth)
T	[K] or [°C]	Air temperature (2 m height)
T_{min}	[K] or [°C]	Daily minimum air (2 m height)
T_{max}	[K] or [°C]	Daily maximum air temperature (2 m height)
T_{am}	[K] or [°C]	Air temperature at Aqua descending overpass time
T_{dew}	[C]	Dew point temperature
e_a	[Pa]	Partial pressure of water vapor in air
e_s	[Pa]	Partial pressure of water vapor in saturated air
VPD	[Pa]	Vapor pressure deficit
δVPD	[Pa]	Error in vapor pressure deficit estimate
LAI	[m^2 m^{-2}]	One-sided leaf area index
m_v	[m^3 m^{-3}]	Soil volumetric moisture content
P	[cm]	Daily precipitation
γ_l		API model water loss coefficient

Brightness Temperature Symbols

Symbol	Units	Description
T_b	[K]	Brightness temperature (generic)
T_{bland}	[K]	Brightness temperature of land fraction
T_{bwater}	[K]	Brightness temperature of water fraction
T_{bp}	[K]	Brightness temperature (for polarization p)
T_{bv}	[K]	Brightness temperature (V-polarization)
T_{bh}	[K]	Brightness temperature (H-polarization)
T_s	[K] or [°C]	Retrieved soil near-surface temperature
δT	[K]	Error in temperature estimate

Emissivities and Reflectivity Symbols

Symbol	Units	Description
e_p		Emissivity (polarization p)
e_{pland}		Emissivity land fraction
e_{pwater}		Emissivity water fraction
e_{sp}		Soil surface emissivity (polarization p)

e_v	Emissivity (V-polarization)
e_h	Emissivity (H-polarization)
e_v^*	Effective emissivity (V-polarization)
e_h^*	Effective emissivity (H-polarization)
r_p	Reflectivity (polarization p)
r_{op}	Smooth surface reflectivity (polarization p)
r_{oq}	Smooth surface reflectivity (orthogonal polarization q)
r_{sp}	Soil surface reflectivity (polarization p)
$r_{sh,corr}$	Smooth soil land-fraction noise-corrected reflectivity
r_v	Reflectivity (V-polarization)
r_h	Reflectivity (H-polarization)

Empirical Algorithm Index and Parameter Symbols

Symbol	Units	Description
ζ		Normalized difference polarization ratio
$\zeta_{min,interp}$		Monthly minimum normalized difference polarization ratio
β		Regression parameters
α		Regression parameters
$\overline{w}$		L3 algorithm baseline parameter
a		Slope for thawed season e_h and e_v relation
b		Intercept for thawed season e_h and e_v relation
a_{sn}		Slope for frozen season e_h and e_v relation
b_{sn}		Intercept for frozen season e_h and e_v relation
$\hat{a}$		Slope estimate for e_h and e_v relation
$\hat{b}$		Intercept estimate for e_h and e_v relation
δa		Uncertainty in estimated slope

Radiative Transfer and Process-based Algorithm symbols

Symbol	Units	Description
ε_r		Complex dielectric constant (Relative to a vacuum)
ε_r'		Real part of the complex dielectric constant
ε_r''		Imaginary part of the complex dielectric constant
Q		Roughness model parameter
h		Roughness model parameter
ω_p		Vegetation single scattering albedo
τ_c		Canopy optical depth (or opacity)
b_c		Canopy absorption loss factor
θ		Incidence angle relative to nadir
W_c	[kg m-2]	Vegetation water content
$\alpha(f)$		Combined vegetation/roughness loss parameter

g	[kg m-2]	Vegetation water content equivalent
γ		Empirical scattering parameter
Cf		Weighted least-squares cost (or objective) function
σ		Cost function weight
ω_{sn}		Snow single scattering albedo
τ_{sn}		Snow optical depth (or opacity)
b_{sn}		Snow absorption loss factor
W_s	[cm]	Snow-water depth equivalent
λ	[cm]	Free space wavelength
f	[GHz]	Frequency
f_w		Open water fraction
τ_a		Atmospheric optical depth (or opacity)
T_u	[K]	Upwelling atmospheric brightness temperature
T_d	[K]	Downwelling atmospheric brightness temperature
$T_{bp,surf}$	[K]	Brightness temperature at Earth's surface